COMPUTATIONAL DISCOVERY AND CHARACTERIZATION OF LOW-DIMENSIONAL
MATERIALS

By

JOSHUA THOMAS PAUL

A DISSERTATION PRESENTED TO THE GRADUATE SCHOOL
OF THE UNIVERSITY OF FLORIDA IN PARTIAL FULFILLMENT
OF THE REQUIREMENTS FOR THE DEGREE OF
DOCTOR OF PHILOSOPHY

UNIVERSITY OF FLORIDA

2020

To all of my family and friends that helped me get to the end

ACKNOWLEDGMENTS

I would first like to acknowledge my advisor, Dr. Richard Hennig. When I learned that he was interested in me joining his group, I was both flattered and inspired to begin my Ph.D. as soon as possible. His guidance throughout my Ph.D. has been phenomenal, and his patience with my mistakes and learning has been sincerely appreciated. It has been a pleasure to work with him, and I am thankful to have worked under him since I arrived at the University of Florida.

I would next like to acknowledge my parents, whose constant support of this pursuit has been a consistent comfort. It was thanks to the lessons you taught me that I have reached this point. I would also like to thank the rest of my family for all their offers of support on this journey.

I wish to acknowledge and thank Sara, Jim, and Sunni for helping me get through the stress of graduate school. Without your presence and constant support, the journey to the end of my degree would have been much more difficult. The tools I have learned through our discussions have been and will continue to be invaluable in all of my pursuits.

I would finally like to thank all my friends, who have been essential to maintaining a work-life balance. Though there is not space to thank everyone, yet all of their friendships been essential to my growth. In particular, my friends from Arizona have kept me grounded, and my friends from table top have provided not only a creative outlet but much entertainment.

TABLE OF CONTENTS

LIST OF TABLES

LIST OF FIGURES

10

Abstract of Dissertation Presented to the Graduate School
of the University of Florida in Partial Fulfillment of the
Requirements for the Degree of Doctor of Philosophy

COMPUTATIONAL DISCOVERY AND CHARACTERIZATION OF LOW-DIMENSIONAL
MATERIALS

By

Joshua Thomas Paul

August 2020

Chair: Richard G. Hennig
Major: Materials Science and Engineering

With the discovery of graphene, a great deal of effort has been invested in exploring

and analyzing two-dimensional (2D) materials and their properties. Density functional theory

has facilitated these efforts by predicting novel 2D materials and determining which have

properties that warrant the time and resources required for experimental pursuits, performed

at a fraction of the cost. This approach has led to the development of several techniques

and software packages to facilitate the high-throughput identification and analysis of 2D

materials. This work contributes to such efforts in several ways. First, data mining techniques

are extended to cleave bulk crystals, identifying low-energy surfaces with comparable stability

to commercially available substrates. Trends are identified between bond energy of the cleaved

surface and the electronic structure of the parent crystal and discussed. This database of

substrates is epitaxially matched to $BaSnO_3$ to identify several low-strain substrates with

lattice strains an order of magnitude lower than currently used substrates. Second, atomically

thin inorganic nanowires are identified by applying the topological scaling algorithm (TSA)

to the MaterialsProject database. This effort identifies crystal structures composed of van

der Waals bonded nanowires and computationally exfoliate nanowires from them, with

their thermodynamic stability calculated relative to their bulk counterparts. The metric

of "line tension" is used to act as a 1D analog to the surface energy of 2D materials. We

follow by discussing the magnetic behavior and electronic structure of these nanowires to

identify a diverse set of behavior. Third, newly developed software considers symmetry in 2D

materials from the perspective of two-dimensional periodicity in a three-dimensional space. The previously established layer groups are used in place of space groups to describe symmetry in 2D materials more accurately. This software standardizes the unit cells of 2D materials and determines the layer group symmetry of the material. Conventions are developed for high-symmetry pathways used in electronic structure calculations for 2D materials. This work ends with a summary of these efforts and an outlook on where these efforts can be further expanded and used as stepping stones for future research.

CHAPTER 1
INTRODUCTION

1.1   Exotic Properties of Low-Dimensional Systems

The discovery of graphene by Geim and Novoslov led to the identification of Dirac cones,[1] giving rise to singinficant interest in the unique properties of 2D materials. Due to quantum confinement, the properties of a layered system change significantly as one approaches single-layer state. This is famously seen in MoS_2 becoming a direct band gap semiconductor when exfoliated into a single layer[2] and hexagonal BN increasing in band gap considerably when a single layer.[3] The quantum confinement effect is a result of the electrons in the system being, effectively, in an energy well for the non-periodic directions. This results in limitations in the energy states they can reach and, as a consequence, a change in electronic properties. Efforts are being made to use these materials for a wide variety of applications, including photocatalysis,[4] transistors,[5,6] piezoelectrics,[7,8] and thermoelectrics.[9] Quantum dots also utilize this effect, with the size of the nanoparticles being used to modulate the electronic properties of the system. Applications of these materials include light production for lasers and displays as well as medical treatments.[10–12] Nanowires have been far less explored than their planar and molecule counterparts, but several efforts exist to synthesize nanoribbons of 2D materials and extereme nanowires, which have few-angstrom radii.[13–17]

1.2   DFT Calculations on Low-Dimensional Materials

In 1998, Walter Kohn was awarded half of a Nobel Prize in chemistry for his development of Density Functional Theory (DFT)[18] which has since become a critical component of computational materials science. Twelve years later, Konstantin Novoselov and Andre Geim were awarded the nobel prize for the their experiments on graphene,[19] which displayed unique and unexpected mechanical and electronic properties.[1] These two groundbreaking works have allowed for a wide range of computational investigations into 2D materials, evidenced by the wealth of literature on the topic cited in Chapter 2. It has been shown that DFT can give high-quality results for low dimensional systems,[20] but considerations must be made to

prevent inaccuracies in the system. First, van der Waals forces need to be considered in order to accurately describe the thermodynamic stability of a layered material, which is detailed in Section 2.3 . Second, the presence of periodic boundary conditions can cause self-interaction between the material and its periodic image, and thus sufficient vacuum is placed along the non-periodic directions of the system.[21-24] Third, the lack of periodicity can result in the formation of periodic lattice distortions, e.g. Peierls distortions, in the system.[25] This is discussed with respect to 1D materials in Chapter 3. This distortion is can be important to predicting the properties of a low-dimensional material, as metal-insulator transitions can result from such distortions.[25-27]

1.3   Discovery of Novel Low-Dimensional Materials

The synthesis of graphene by Geim and Novoslov was performed by exfoliating a monolayer using scotch tape, which resulted in research pursued in other well known layered systems. Once these relatively low-hanging fruit were picked, new techniques needed to be used to identify novel 2D materials. These can, broadly, be categorized into two groups: techniques which rely on known crystals, and techniques agnostic to any known crystals. With regard to the former category, datamining and chemical subsitution are the most common approaches. Datamining efforts have primarily searched materials databases for layered, graphite-like structures[22,24,28-31] and, while extremely successful, can only produce new 2D materials if new structures are added to the database searched over previously. In Chapter 4 I explain a novel approach which searches for fully periodic crystals and breaks bonds to identify easily cleaved surfaces. Chemical substitution takes known 2D materials and substites the atomic sites in the crystal with different species, commonly limited elements similar to the species being substituted. This approach is less efficient than datamining in identifying novel low-dimensional systems, but has been demonstrated to be a successful approach.[32-34] Techniques which are agnostic to known crystal structures are grand canonical, exploring the energy landscape of a system to identify the global minimum. A careful balance of exploring the energy landscape

15

and exploiting identified minima is needed to properly idenitfy the crystal structure which represents the global minimum, though there is no way to guarantee the lowest energy structure found truly lies at the global minimum. This approach has successfully identified a number of 2D materials, and has been shown to be predictive of monolayers which were later synthesized in a laboratory setting.

1.4 Advances in Computational Materials Science Tools

One of the primary techniques to advancing technology has been improving the materials used to construct said technology. Recognizing this, the Materials Genome Initiative was launched by the USA government in 2011 and integrated into the mission statements of several federal organizations.[35] Experimental databases such as the inorganic crystal structrue database (ICSD)[36] had existed for decades prior to this announcement, a number of computational databases were created, including MaterialsProject,[37] the Open Quantum Materials Database,[38] AFLOWLIB,[39] JARVIS-DFT,[24] and MaterialsWeb.[22] This has resulted in the properties of a vast number of materials being publically available, helping prevent scientists from "reinventing the wheel" and focus their efforts on novel investigations. The most basic of properties avaible are the lattice constants and atomic positions of a crystal,[22,24,36–39] typically obtained using a DFT software to perform structural optimization. Depending on the database, further properties available can include (but are not limited to) electronic strucutre, phonon modes, elastic constants, piezoelectric tensors, thermodynamic stability, solubility in water, and optical spectra.

These databases contain tens to hundreds of thousands of unique crystals within them, which leads to the opposite problem of before. That is, there are now too many materials to select from. The previously mentioned computational databases are open-source, often with a web interface for the user to search the information therein. To facilitate high-throughput efforts which use these datasets, numerous databases have included some method of mass querying the database, such as accessing the information using an API key or downloading the entire database.[22,24,37–39] Using these tools, users can perform an inital screening based on

some criteria relevant for the desired application. This provides a short list for the user, which may be sufficient for the application in mind. However, in order to contain such a large number of materials, the initial calculations tend to be limited in accuracy, else computational costs become excessive and cannot be performed for such a large number of crystals.

To facilitate computational materials science research, a plethora of open-source software packages exist. Atomic Simulation Environment (ASE)[40] was a forerunner in preparing and analyzing the results of computational investigations. Since then, packages such as pymatgen[41] and MPInterfaces[42] have been developed which specifically address the DFT need for the preperation and execution of high-throughput computational investigations. Though the former two packages are focused on fully periodic systems, advances are being made though packages such as MPInterfaces to treat specifically low-dimensional systems. Coinciding with the development of software packages has been a great expansion of computation power. Supercomputing clusters such as STAMPEDE, ARL DSRC, and HiPerGator can supply computational resources and, when combined with the development of open-source software and databases, has resulted in explosive growth in the field of computational materials research.

In order to optimize the use of computational resources, some materials must be screened from the investigation. Knowledge of physics and chemistry can be used to justify the screening to achieve the intelligent decrease of scope. For example, only materials which can be feasibly synthesized are relevant to developing technologies, and thus thermodynamic stability can be used as a criteria. If one is screening for dielectrics then metallic materials need not be considered, and if piezoelectrics are of interest then any crystal with inversion symmetry can be removed. Though defect engineering can be used to custom tailor the properties of a crystal, open-source databases contain hundreds of thousands of unique crystal structures, some of which can inherently possess the properties of interest. After this pre-screening step, DFT codes can be used to perform higher-fidelity calculations of materials properties and provide a list of tens or hundreds of materials relevant to a given application, decreasing the

possibility space by four to five orders of magnitude. From this subset, a feedback loop can begin between experimental and computational efforts to further refine the list and understand the system and properties.

1.5   Outline

Discussed in the remainder of this dissertation are efforts to identify and better understand low-dimensional materials to aid experimental efforts. These efforts are either papers which are published, under review, or under preperation, with all calculations of properties performed using DFT. Chapter 2 is a review article I authored in 2017 with several co-authors. The details of contributions will be described at the start of the chapter. The review article is an overview of computational efforts on 2D materials up to that point. It begins with an overview of 2D crystal structures in Section 2.2, followed by an overview of the methods and software used for computational investigations into 2D materials in Section 2.3. Section 2.4 describes the thermodynamic requirements for 2D materials to be considered stable and is followed by techniques to discover novel 2D materials in Section 2.5. Interactions with various environments, as opposed to vacuum, are discussed in Section 2.6. Electronic, magnetic, and superconducting properties are covered in Sections 2.7, 2.8, and 2.9, respectively. Section 2.10 covers how various properties in 2D materials change with various stimuli and Section 2.11 outlines the different kinds of defects that can be found in 2D materials and the impact they have on their properties. Section 2.12 briefly discusses techniques to synthesize 2D materials and is followed by simulating the integration of 2D materials into electronic devices. The article concludes with an outlook on the future of 2D materials, primarily how the wide variety of new 2D materials discovered will need to be explored for their response to various non-ideal conditions and the growth of open-source 2D materials databases.

Chapters 3 and 4 can be, broadly, categorized as extensions of development and application of the toplogical scaling algorithm (TSA).[22] I conclude with Chapter 5, where I describe the limitations of using the space groups for classifying the symmetry of 2D systems. Chapter 3 applies identifies van der Waals bonded solids composed of nanowires, i.e. crystals that

are composed of van der Waals bonded inorganic polymers. I explore the sensitivity of the TSA to the bonding criteria chosen, as well as unique crystals such as heterostructures and bipartite crystals. Following, I exfoliate nanowires from their bulk precursors and calculate their formation energy. Using 1D tellurium as a standard, I define "line tension", a measure of thermodynamic stability analogous to the "surface energy" of 2D materials and find it to be a much stricter criteria for stability than exfoliation energy. I then discuss the challenges of structurally optimizing 1D materials using DFT and the existence of various local minima of comparable stability in their energy landscapes. Exploration of their electronic and magnetic properties follow, which finds not only a wide variety of electronic behaviour but also the energy barriers for the magnetic ordering of five magnetic 1D materials.

In Chapter 4 I develop a novel algorithm which breaks bonds within a crystal to idenitify low-bond-density surfaces in crystals with primitive cells of five or fewer atoms. The intention of this search is to identify surfaces which are stable enough to be used as substrates which will have smooth surfaces. Through this process, I identify 3,847 unique cleavage surfaces across 1,847 periodic crystals. I identify a strong correlation between the work of adhesion of these surfaces and their relaxed states. This process generate 2,924 possible substrate materials, drastically increasing the possibility to experimentally synthesize crystals with lower strain, and thus fewer defects. I demonstrate this by searching the database for epitaxial matches to $BaSnO_3$, identifying three low-strain substrates which could decrease the defect density in thin films of the crystal.

Chapter 5 investigates improved ways to classify 2D materials based on symmetry. Wallpaper groups have their applications, but do not properly describe the thickness of a 2D material. Space groups are also insufficient, due to their assumption of periodicity in all directions. Instead, the already known layer group operations should be used to describe 2D materials, as they consider systems which exist in three dimensions but are only periodic in two. I summarize the literature which relates space groups to layer groups, and develop software which standardizes 2D crystal unit cells and determines their layer group. I also

provide a complete list of high symmetry pathways for 2D materials based on the possible Bravais lattices.

Chapter 6 summarizes the findings of Chapters 4, 3, and 5 and the lessons learned from these investigations. It concludes with an outlook on the field of computational research into low-dimensional materials and datamining efforts, as well as the next steps to take in the field.

CHAPTER 2
COMPUTATIONAL METHODS FOR 2D MATERIALS: DISCOVERY, PROPERTY CHARACTERIZATION, AND APPLICATION DESIGN

This chapter is a review article authored in 2017 on developments in computational research of 2D materials, with a number of coauthors to maximize the amount of information provided. My contributions include significant to majority portions of Ch. 2.3, Ch. 2.4, Ch. 2.5, Ch. 2.10, Ch. 2.11, Ch. 2.7 and complete authorship of Ch. 2.6.2. My total contributions account for 40% of the publication.

2.1   Background

Since the discovery of graphene,[43] the field of two-dimensional (2D) materials and research on the discovery, characterization, and application of novel 2D materials has grown exponentially. This excitement was initially due to the extraction of a 2D crystal whose existence was ruled out by earlier harmonic approximation theories of Mermin and Wagner[44] but later proven to be stable due to coupling between bending and stretching modes.[45,46] The remarkable properties of graphene, such as the presence of a Dirac cone, and thus high conductivity in the monolayer, further motivated the investigation of other potential 2D materials. The next several 2D materials to be discovered were hexagonal boron nitride (h-BN), with a wide band gap,[3,47] MoS_2, which displays an indirect to direct band gap transition between the bulk and monolayer forms,[48] and other members of the 2D transition metal dichalcogenide (TMDC) class of materials with predominantly semiconducting nature and band gaps larger than their bulk counterparts.[49]

More recently, III-V semiconductors,[33] metal oxides,[50,51] MXenes,[52,53] II-VI semiconductors,[54,55] and many other compositionally diverse 2D materials[22,56–59] have been predicted and in some cases synthesized. While the first 2D materials – graphene and h-BN – are atomically thin, most 2D materials possess a finite thickness. They are still commonly categorized as 2D materials, and they typically possess significantly different properties than their bulk counterparts.[22,28,48,49,53,60]

2D materials can be difficult to synthesize due to their extremely thin nature, and the fact that they are not the thermodynamic ground state of a given materials system. Novel experimental techniques have been developed to synthesize and characterize 2D materials, freestanding and supported on substrates. 2D monolayers can be obtained from certain layered bulk precursors by means of mechanical[61–64] or chemical[65] exfoliation. Deposition on a substrate is another popular method for creating 2D materials.[66–68] Predicting the structure and composition of a 2D material on a given substrate is the subject of intensive ongoing research.[21, 60, 69–71] Computational approaches provide a valuable guide for experimental efforts toward the synthesis of 2D materials with specific structures and properties. Such approaches can discover novel monolayers,[22, 28, 33, 34, 72] identify suitable substrates for their synthesis and growth, characterize their properties, and predict their performance when used in devices.

So far close to one hundred 2D materials have been synthesized, several hundred more are predicted to be stable, and many more are likely awaiting discovery. The rapid growth of the family of 2D materials, with a broad range of properties suitable for many applications, presents an exciting opportunity for researchers to explore an entirely new class of materials. This opportunity has come at a time when mature computational methods provide the predictive capability to enable the computational discovery, characterization, and design of 2D materials as well as provide the needed input and guidance to experimental studies.

Several reviews have been written on the topic of 2D materials,[73–75] on specific 2D materials, including graphene,[76–79] h-BN,[80] transition metal dichalcogenides,[81, 82] MXenes,[83] metal oxides,[84] and phosphorene,[85] and for van der Waals (vdW) heterostructures.[86, 87] These articles focus on experimental works and methods, but provide some discussion on computational methods. Review articles with a focus on computational methods have been written on the discovery and characterization of 2D materials,[21] the design of 2D materials for specific applications, such as photocatalysis,[4] and multiscale methods for graphene-based materials.[88]

a) Crystalline 2D Materials

C (Graphene)   P (Phosphorene)   2H-MoS$_2$

1T-MoS$_2$ Litharge SnO   Ti$_2$CO$_2$ (MXene)

b) Quasicrystalline 2D BaTiO$_3$

c) Amorphous 2D SiO$_2$

1.42 Å
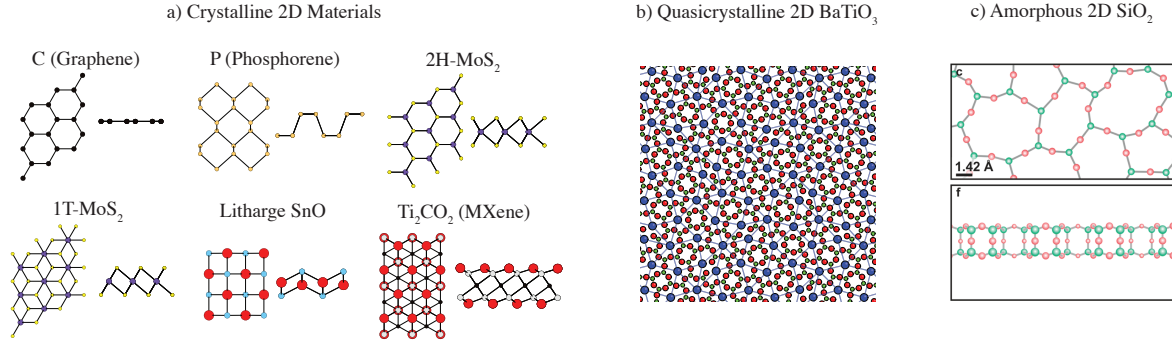
Figure 2-1. The three classes of 2D material structures. Structures of (a) well-known periodic crystalline 2D materials, (b) 2D quasicrystalline structure of BaTiO$_3$ (reprinted from Ref. 89 Copyright 2016 by the American Physical Society), and (c) amorphous 2D structure of SiO$_2$ (reprinted from Ref. 90).

In this work, we review the state of modern computational methods available for studying 2D materials. In Sec. 2.2, we generalize the structure classification of bulk materials to provide definitions that include the classification of two-dimensional materials structures. We then continue to provide a brief overview of density-functional theory approaches and cyber infrastructures for 2D materials in Sec. 2.3, discuss the general criteria for thermodynamic stability and computational methods to assess the stability of 2D materials in Sec. 2.4, and describe approaches for the discovery of novel 2D materials in Sec. 2.5. We then consider computational methods to assess the environmental stability of 2D materials in Sec. 2.6. We next move on to computational methods for the characterization of the various properties of 2D materials in Secs. 2.7 to 2.10. We continue by discussing defects and their role in 2D materials in Sec. 2.11, and following a short foray into synthesis methods for monolayers and heterostructures in Sec. 2.12 we describe modeling approaches for heterostructures devices in Sec. 2.13. We conclude in Sec. 2.14 by looking towards the future of 2D materials and discuss where novel computational tools and research is needed. The breadth of computational methods for 2D materials and the comprehensive coverage of this broad field in our review requires that we will refer the reader to the literature for some more in-depth discussions throughout this work.

2.2 Structure of 2D Materials

2.2.1 2D structure Definition and Classification

We begin by extending the classification of bulk materials' structures to 2D materials. We define a 2D material as a material with a finite thickness in one dimension and an essentially infinite extent in the other two dimensions. In practice, the thickness of 2D materials ranges up to about a nanometer, a scale below which the thickness strongly affects the materials' properties. The extent in the other dimension should be sufficiently large such that the edges should not affect the overall properties. Otherwise, the material should be classified as a one-dimensional material, *e.g.* a wire or ribbon, or as a zero-dimensional material, *e.g.* a nanoparticle, cluster, or molecule.

Similar to 3D materials,[91] we can further classify 2D materials into crystalline and amorphous materials. Crystalline 2D materials are 2D materials with long-range order in only two dimensions that leads to essentially discrete diffraction patterns, and a finite extent in the third dimension. The class of crystalline materials includes periodic crystals that exhibit translational symmetry and aperiodic crystals. Based on their point group symmetry, we further classify aperiodic crystals into incommensurate crystals and quasicrystals. Aperiodic crystals exhibit translational order but not translational symmetry; they display symmetries in their diffraction patterns, *e.g.* five or twelve-fold,[92] which are incompatible with periodic symmetry and, hence, not possible in periodic crystalline solids. Amorphous 2D materials lack long-range order and do not display discrete diffraction patterns.

2.2.2 Examples of 2D Structures

Figure 2-1 shows examples of crystalline, quasicrystalline and amorphous 2D materials. Most 2D materials, such as graphene, h-BN, and TMDCs belong to the family of periodic 2D crystals. The first quasicrystalline 2D material is $BaTiO_3$ grown on Pd, which exhibits a twelve-fold symmetry that is incompatible with translational symmetry.[89, 93] The first amorphous 2D material is SiO_2, the world's thinnest glass, with a bilayer structure of silica tetrahedra that form a continuous network of mostly 5, 6, and 7-membered rings.[90, 94]

Several of the crystal structures shown in Figure 2-1(a) correspond to single layers in naturally occurring vdW layered solids. This is true for many stable 2D materials. The vdW interlayer forces in layered solids are quite weak and responsible for only a small part of the material's overall Gibbs free energy.[22, 95, 96] As a result, the existence of a naturally occurring vdW layered solid often indicates the existence of a viable 2D crystal structure. This is why, as will be discussed in Sec. 2.5.1, systematic searches for layered materials among bulk materials databases have been able to predict such a large number of stable 2D materials.

There are certain stable 2D materials, however, which have no naturally occurring layered bulk parent structure. The bi-tetrahedral crystal structure of 2D SiO_2, shown in Figure 2-1(c), is one such example. The lowest energy crystal structures of these "orphan" 2D materials are harder to predict, but computational methods exist to uncover them as well. We discuss these methods in some detail in Secs. 2.5.2 to 2.5.5.

2.2.3 Polymorphism in 2D Materials

Some 2D materials can occur in different polymorphs that are either sufficiently close in energy to be experimentally observable or stabilized through substrates or by doping. For these 2D materials, the structural difference between the polymorphs can significantly impact the properties of the compound.[97–106] For example, 2D MoS_2 is most stable in the semiconducting $2H$ phase, but also displays a metallic $1T$ and a small band gap topological insulator $1T'$ polymorph.[97, 98] For 2D phosphorene, several polymorphs have been predicted, including blue phosphorene with an indirect band gap of 2 eV, which is energetically nearly degenerate with black phosphorene with a direct band gap of about 1 eV.[99–101] 2D antimonene exhibits two polymorphs, α and β, which are both dynamically stable and have significantly different band structures, though the α phase is lower in energy.[102]

2.3 Computational Methods and Cyber Infrastructure

2.3.1 Brief History of DFT

The properties of 2D materials are usually computed using the framework of density functional theory (DFT).[22, 33, 34, 60, 107, 108] Even though the idea of describing quantum systems

in terms of their density dates back to the Thomas-Fermi model[109, 110] and the Weizsäcker kinetic energy functional,[111] Hohenberg and Kohn were the first to show that the ground-state electronic density indeed determines all properties of an interacting many-body quantum,[112] thereby putting these ideas on a firm footing. While Hohenberg and Kohn established that knowledge of the ground state electron density in principle determines the ground state energy, they provided no direct way of calculating it. Kohn and Sham[113] proposed to construct an auxiliary non-interacting system with a single particle potential whose electron density agrees with that of the interacting system. The exact ground state energy is then formally written as a functional of the density, and since a single particle problem is a numerically tractable problem, given this single-particle Kohn-Sham potential, the energy can be calculated. Aside from the external potential, which determines the system, the Hartree potential contribution is treated exactly. The remainder, originating from exchange and correlation (xc) contributions has to be approximated.

2.3.2 Exchange-Correlation Functionals

Kohn-Sham in their work on the auxiliary system already proposed the local density approximation (LDA) for exchange and correlation, which replaces the xc potential locally at each point in the unit cell with the xc potential of the interacting electron gas with the same density.[113] The exchange part is calculated analytically; however, the correlation cannot, and LDA functionals[114–116] are usually based on parameterizations of quantum Monte Carlo calculations.[117] One of the most widely used LDA functionals is that of Perdew and Wang.[116] The LDA leads to good total energies for metals but is known to underestimate bond lengths.[118]

More accurate functionals rely on similar ideas but also include additional information about the electron density, such as its gradients in the generalized gradient approximation (GGA), and additionally the curvature or kinetic energy density in meta-GGA functionals. Several flavors of GGAs exist, with two of the most widely used ones being the Perdew-Burke-Ernzerhof functional (PBE)[119] and the Becke-88 functional.[120] GGA type functionals usually

further improve total energy predictions for solids and molecules and predict lattice parameters very accurately as compared to experiment. The outstanding accuracy and computational efficiency of these semi-local functionals makes DFT the standard method in computational materials science and chemistry, and condensed-matter theory.

2.3.3 Hybrid Functionals for Accurate Band Gaps

A common shortcoming of semi-local functionals is the underestimation of a possible band gap in the system. This effect is ultimately related to the derivative discontinuity of the exact exchange and correlation potential with respect to the particle number, which the LDA and GGA type approximations are missing.[121] The PBE0[122] and Heyd-Scuseria-Ernzerhof (HSE)[123] functionals include, *e.g.*, 25% of the exact exchange contribution, which improves the agreement of the Kohn-Sham band gap with experiment,[121] as well as the defect formation energies[124,125] and phase transition pressures for metal-insulator transitions.[126] Because they contain both DFT and Hartree-Fock contributions these functionals are referred to as hybrid functionals. Note that the explicit dependence of the functional, now not only on the density but also on the Kohn-Sham wavefunctions, leads to a significant increase in computational cost. Meta-GGAs also improve band gaps to some extent while being in general less expensive.[121] Both in computational cost and accuracy, they range in between GGAs and the hybrid functionals.

2.3.4 DFT+U Method

DFT with semi-local and hybrid exchange-correlation functionals accurately describes the structural and electronic properties of bulk materials. However, in some materials, strong electronic correlation present additional challenges and require special treatment. In a broad sense, correlations are effects that cannot be incorporated into an effective non-interacting system which naturally makes them hard to describe in a Kohn-Sham single-particle system. Especially for strongly localized states with a small overlap between neighboring lattice sites, the correlation energy can dominate and behave very differently from the homogeneous electron gas that provides the starting point for the functional construction. It is possible

to correct for the shortcomings of these functionals by selecting these localized states and describing them with an independent Hubbard model of electrons interacting with an effective screened Coulomb interaction U. In practice, this Hubbard interaction, U, in this DFT+U treatment is an adjustable parameter with common values for various materials classes.[127–129]

2.3.5 Many-Body Methods

The most accurate method to compute band gaps is based on the Dyson equation for the single particle Green's function, G. Hedin reformulated the exact solution of the Schrödinger equation in terms of five coupled integral equations and suggested an approximation that neglects the screening of the electron vertex function.[130] The result is a system of equations where the screening of the Coulomb interaction, W, is treated within the random phase approximation (RPA), which then enters the equation for the Green's function via the self-energy $G \cdot W$, hence the name GW approximation.

In practice, DFT is used to obtain a starting system, and different levels of self-consistency are imposed to arrive at a final solution. The G_0W_0 approximation computes the screening in the Kohn-Sham system, W_0, and the self-energy is constructed with the Kohn-Sham Green's function, G_0, to update the Kohn-Sham energies. The partially self-consistent GW_0 approximation imposes self-consistency at the level of the Green's function but keeps the screening fixed. Finally, the fully self-consistent GW approximation treats both the Green's function and the screening it provides self-consistently.[131] It is observed that the GW_0 matches the experimental data well and that the significantly more computationally expensive fully self-consistent GW method provides similar results.

While GW-type methods yield accurate single electron excitations, computing neutral two particle interactions such as electron-hole pair or exciton interactions requires a more accurate calculation of the polarizability at the level of the Bethe-Salpeter equations (BSE).[132] Interactions of this kind are important in the calculation of optical absorption spectra, but are numerically very expensive. Alternatively, time dependent DFT (TDDFT) can be applied to

compute optical spectra of solids, which is numerically much more efficient while usually less accurate.[133–135]

2.3.6 *Van der Waals* **Interactions**

Another intrinsically non-local effect that semi-local DFT functionals fail to describe are vdW interactions. Especially for layered materials, the neglect of this effect can lead to significant underestimation of the bonding energy and interlayer distance. Common methods to account for this effect range from empirical corrections,[136,137] to non-local exchange correlation functionals,[138,139] to full many-body treatment of vdW interactions.[140,141] Comparison with more accurate and computationally demanding random-phase approximation (RPA) calculations show that these non-local functionals and the many-body treatment of vdW interactions reproduce relative trends in exfoliation energy and predict the interlayer interactions within 30% of the RPA.[22,142,143] The vdW interactions are of particular importance for 2D materials, where energies are to be compared to bulk references. If the bulk material is layered, semi-local functionals will underestimate the binding energy. As discussed in the previous section, layered bulk materials provide an important set of candidate materials for exfoliation of 2D materials.

2.3.7 **Software Packages**

DFT methods have mostly been developed on and for bulk 3D materials. However, functionals show very accurate performance also in reduced dimensions? for many materials systems. Similarly, most Kohn-Sham DFT software packages are designed for 3D systems and employ periodic boundary conditions. The standard method for calculations of 2D materials is to approximate the 2D material by a slab embedded in a 3D simulation cell. Periodic images of the slab must be separated by a sufficiently large region of vacuum. Especially for layers which lack inversion symmetry or exhibits an electric dipole moment, this setup has to be treated with care since periodic replicas will be present in the third dimension which can lead to spurious interactions if the vacuum is not sufficiently large. Widely used software packages

that can perform DFT calculations for 2D materials include VASP,[144–146] Quantum Espresso,[147] ABINIT,[148] and CASTEP.[149]

2.3.8 High-Throughput Frameworks

Bahn and Jacobsen were among the first to realize the potential of a highly automatic framework to systematically setup, run, and analyze DFT calculations when they developed the Atomic Simulation Environment (ASE).[40] The package prepares, runs, manipulates, and analyzes results from a wide array of simulation packages.

A decade later, Python Materials Genomics (Pymatgen) was developed.[41] This tool manipulates input and analyzes output files of various DFT software packages and interfaces with the Materials Project database of materials. Recently, the package MPInterfaces has been developed to aid the study of nanoparticles and interfaces.[42] In addition, it provides a framework for high throughput submission and screening of simulations for DFT software packages. These tools make the acquisition and analysis of material data far more efficient, increasing the speed of computational research.

2.3.9 Materials Databases

It has become increasingly common to make calculated materials data available through online databases. Databases which host data specifically for 2D materials include the Computational Materials Repository,[150] the Midwest Nano Infrastructure Corridor 2D Database,[151] and the MaterialsWeb database.[22] In order to facilitate large scale analysis, some of these databases provide high-throughput application programming interfaces (APIs) to their data. MaterialsWeb, for example, uses the Materials API developed for the Materials Project and Pymatgen. With this API, users can systematically access the DFT data on the Materials Project or MaterialsWeb databases using programs written in python.

2.4 Thermodynamic Stability

Materials are stable when they are in thermodynamic equilibrium. The second law of thermodynamics commands that for a material to be in equilibrium at constant pressure, p, and temperature, T, its Gibbs free energy must be a minimum. The Gibbs free energy,

$G(p, T) = E + pV - TS$, has three contributions: the internal energy, E, the volume, V, and the entropy, S. For condensed phases, the pV contribution is usually negligible. The entropy contribution, TS, becomes increasingly important at higher temperatures. For solid materials, there are three main contributions to entropy: the vibrational entropy due to phonons, the configurational entropy due to site disorder in alloys and point defects, and the electronic entropy due to excitations of the electrons across the Fermi level.

DFT-based methods can calculate the various contributions to the Gibbs free energy of a material. DFT is a ground state method and directly computes the internal energy, E, and the volume, V, given an external pressure, p. The contributions to the entropy are commonly calculated using separate methods.

The vibrational entropy is determined by integrating the phonon spectrum for crystalline materials. The phonons can be accurately computed with DFT using either a finite displacement method[152] or using density functional perturbation theory (see Ref. 153 for a review). As non-interacting bosonic particles, the phonon contribution to the entropy is then easily computed according to the Bose-Einstein statistic. The Python code Phonopy[154] assists in setting up and analyzing these calculations.

The configurational entropy can be obtained from Monte Carlo calculations, which require the energy of site disorder and defect formation. DFT can in principle provide these energies. In practice, the vast number of possible configurations makes it unfeasible to directly determine all the energies using DFT, and surrogate models such as cluster expansions fit to DFT are used instead. Several software tools, such as ATAT[155, 156] and UNCLE,[157] can set up and submit the required DFT calculations, optimize the cluster expansion, and perform the Monte Carlo simulations to obtain the configurational entropy.

For the electronic contribution to the entropy at low to moderate temperatures where crystalline solids exist, it is a reasonable approximation to use the zero temperature band structure and populate it according to the Fermi-Dirac statistic.

The vibrational and configurational entropy contributions of a material are bound from above by the Dulong-Petit law at $3/2kT$ per atom. The electronic entropy is negligible in semiconductors and insulators but can be significant in metals with a high electronic density of states at the Fermi level. Since it is the differences in the Gibbs free energy of materials that determines the thermodynamic stability, part of the entropy of materials cancels. For materials with similar Debye temperatures, site disorder, and band gaps or electronic density of states at the Fermi level, most of the entropy cancels and it is therefore a good approximation to neglect the entropy contribution to the Gibbs free energy.[158,159]

2D materials are not in thermodynamic equilibrium, and hence are inherently metastable since the stacking of monolayers always lowers the energy due to vdW attraction between the layers. Hence, when a 2D material is colloquially referred to as stable, it is understood that the monolayer is in fact thermodynamically metastable. For the synthesis, growth, and application of 2D materials, it is required that the 2D materials be sufficiently stable such that any processes that drive the transformation or decomposition of the 2D material are kinetically slow. For the computational study of the stability of 2D materials, we need to identify suitable criteria sufficiently stability. We will discuss the two complementary criteria of hull distance and surface energy in the following Secs. 2.4.1 and 2.4.2, respectively.

2.4.1 Hull Distance

Early work on 2D materials presented negative enthalpies of formation as an indicator of thermodynamic stability in predicted 2D materials. However, since the enthalpy of formation is the energy difference between a material and its pure elemental constituents, it is a necessary but insufficient piece of evidence for materials stability. For a material to be thermodynamically stable, it must have a negative enthalpy of formation not only with respect to the pure constituents but relative to all possible competing phases.

Mathematically, the ground state phases for a multi-component materials system are those that lie on the convex hull of the Gibbs free energy as a function of composition, sometimes also referred to as the thermodynamic hull. Figure 2-2 illustrates the convex hull for the Fe-Cl
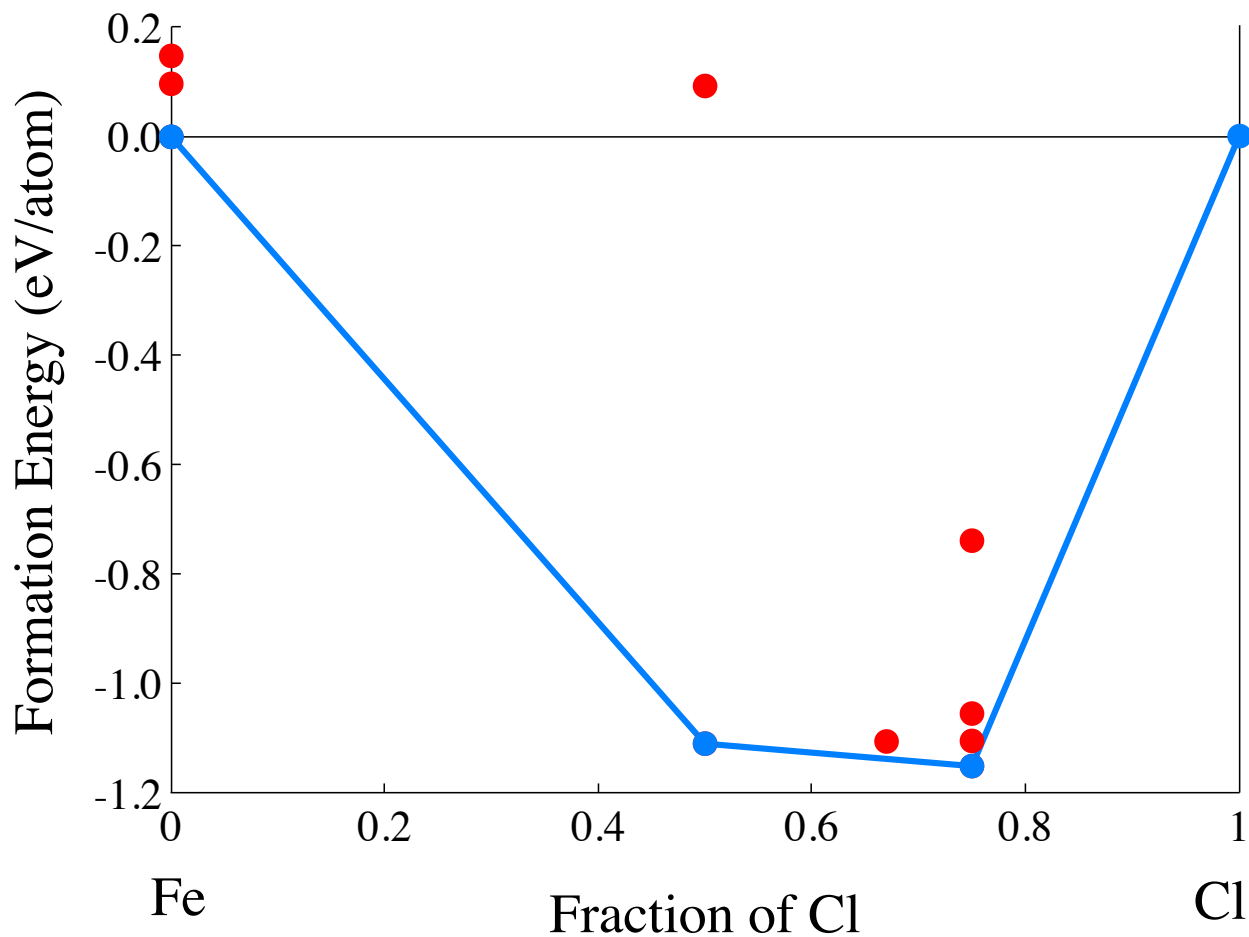
Figure 2-2. The phase diagram for the Fe-Cl system, derived from data at MaterialsProject.org.[37, 160, 161] The most stable phases are represented by blue circles, and the thermodynamic/convex hull is outlined in blue. Compounds above the hull are represented by red circles.

system. Any phase not on the hull is thermodynamically unstable and can lower its energy by decomposing into one or more phases that do lie on the hull. Therefore, when evaluating the stability of a 2D material, the relevant thermodynamic measure is its distance above the convex hull of the ground state (bulk) phases.

A review of already existing 2D materials reveals that only those with hull distances < 200 meV/atom were synthesized as free-standing monolayers.[4, 60] In light of this finding, we recommend using a threshold of 200 meV/atom for the hull distances of potential 2D
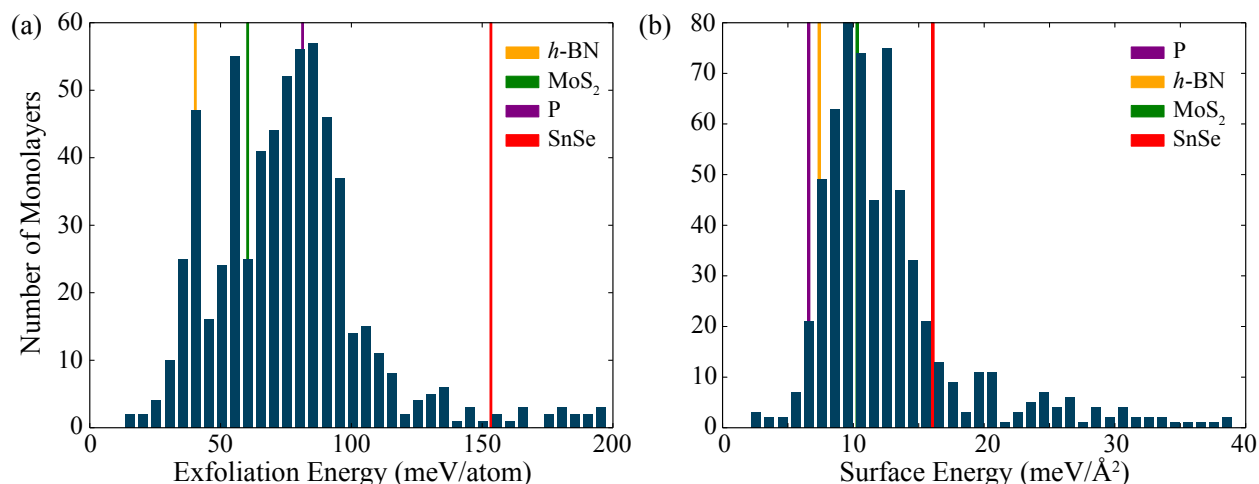
Figure 2-3. Demonstration of thermodynamic stability of 2D materials. Histograms of (a) the hull distance and (b) surface energy criteria for evaluating the thermodynamic stability of 2D materials. The orange, green, purple, and red lines represent the energies of the monolayers h-BN,[142] MoS$_2$,[142] phosphorene,[162] and SnSe,[163] respectively, which have all been synthesized as free-standing layers.

materials as an upper bound on sufficient thermodynamic stability for the synthesis and growth of free-standing monolayers.

We note that the hull distance should not be confused with the exfoliation energy, which is the energy needed to exfoliate a monolayer from a layered bulk material. For 2D materials that correspond to monolayers exfoliated from a ground state layered bulk material, the hull distance and exfoliation energy are indeed the same. However, some layered bulk compounds are not thermodynamic ground states and several 2D materials lack any layered bulk structure from which they can be exfoliated. In the former case, the hull distance is in fact larger than the exfoliation energy and the exfoliation energy may overestimate the stability of the monolayer. In the latter case, no exfoliation energy exists. For thermodynamic reasons and consistency, we recommend the hull distance as the criterion for thermodynamic stability, and not the exfoliation energy nor the enthalpy of formation.

2.4.2 Surface Energy

The surface energy, γ, provides an alternative measure of the thermodynamic stability of a 2D material,[60]

$$\gamma = \frac{N_{2D}}{2A} \Delta E_f, \qquad (2\text{-}1)$$

where ΔE_f is the formation energy relative to the bulk ground state(s), *i.e.* the hull distance, N_{2D} is the number of atoms in the cell of the 2D structure, and A is the in-plane area of the 2D material. The surface energy can be especially useful for evaluating the stability of 2D materials whose structures differ from those of their bulk counterparts. Also, in contrast to the distance from the convex hull, the surface energy is not as strongly affected by the number of layers in multilayer 2D materials, whereas the distance from the convex hull approaches that of the layered bulk compound.[60] Hence, the surface energy criteria for the stability of 2D materials may be advantageous for computational methods predicting novel 2D materials as will be discussed in Sec. 2.5.

2.4.3 Difference Between Standards

We compare the two stability criteria – hull distance and surface energy – using the MaterialsWeb database of over 600 2D materials.[22, 164] Note that most of the over 600 compounds in MaterialsWeb are exfoliated from ground state layered materials and a few from layered bulk materials with hull distances of up to 50 meV/atom. Hence, their exfoliation energy equals or is very similar to their hull distance.

Figure 2-3 shows the histograms for the two criteria and compares the criteria with the values for common 2D materials, h-BN, MoS_2, phosphorene, and SnSe. Although phosphorene and h-BN have significantly different exfoliation energies, their surface energies are very similar. SnSe, the most unstable 2D material that has been synthesized as a freestanding layer,[165] has the highest energy in both standards.[166]

Figure 2-4 compares the two criteria across the over 600 2D materials of the MaterialsWeb database.[22, 164] Applying the exfoliation and surface energy of SnSe as the threshold for defining stability, we find that the surface energy criterion is stricter, resulting in approximately
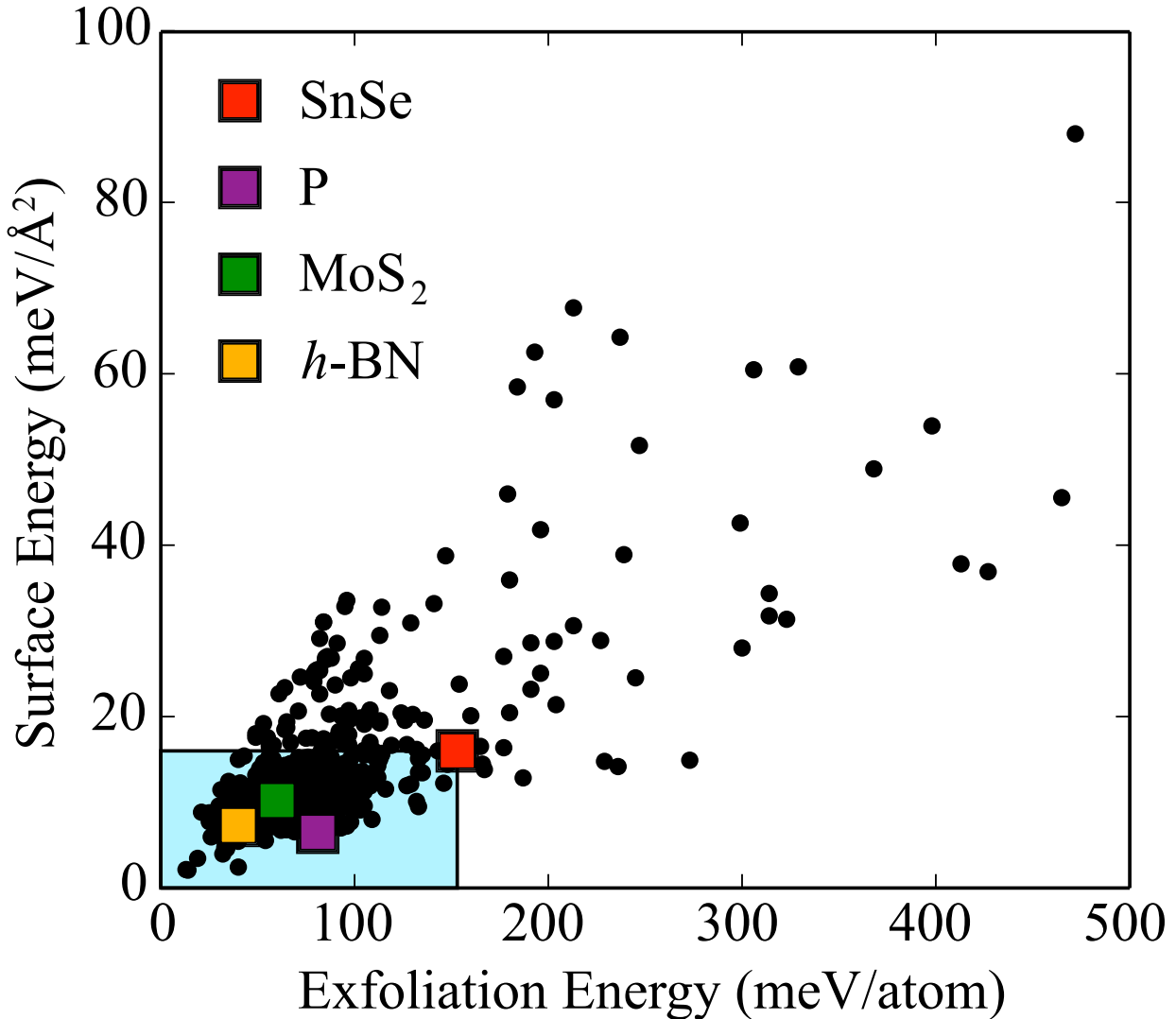
Figure 2-4. Comparison of the stability criteria for 2D materials – exfoliation energy *vs.* surface energy for each of the 2D materials in the MaterialsWeb database discovered by Ashton *et al*. The orange, green, purple, and red squares represent the experimentally synthesized free-standing monolayers h-BN,[142] MoS_2,[142] phosphorene,[162] and SnSe[163] respectively. The shaded region shows the energy ranges containing monolayers that are considered the most feasible to synthesize as free-standing monolayers.

10% fewer structures than the exfoliation energy threshold. However, the surface energy threshold also captures several monolayers, about 1%, that do not pass the exfoliation energy cutoff. In conclusion, both criteria are empirical and provide insight for evaluating monolayer stability.
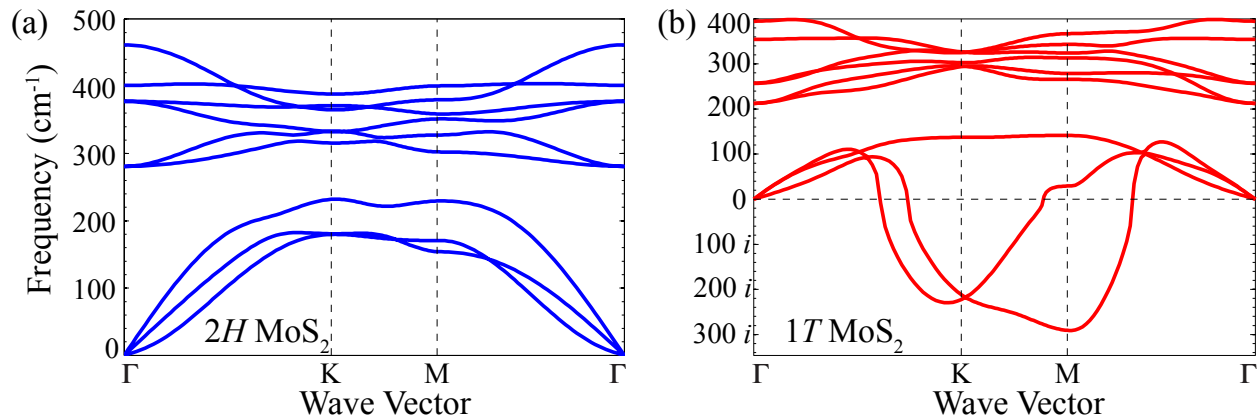
Figure 2-5. Phonon spectra of two polymorphs of 2D MoS$_2$. These are the $2H$ structure (a) and the $1T$ structure (b). The presence of imaginary modes indicates that the $1T$ structure is not dynamically stable.[98]

2.4.4   Dynamic Stability

Metastable materials, such as 2D materials, can exhibit another type of instability that originates from a lack of restoring forces when the structure is perturbed. Such instabilities are reflected in the phonon spectra of materials, where imaginary modes indicate unstable perturbations, which can lead to reconstructive or martensitic phase transformations. A classical example is the low-temperature instability of the bcc phase of Ti, which leads to martensitic phase transformations to either an hcp or ω phase.[167–169]

When considering the stability of 2D materials, it is important to include the dynamic instability to identify possible reconstructions to lower-energy 2D structures. Empirically, 2D materials with larger exfoliation energy or convex hull distances are more likely to exhibit unstable modes since the energy of the structure is bound from below by the energy of the bulk phase. Figure 2-5 illustrates a dynamic instability in one of the polymorphs of 2D MoS$_2$. The imaginary modes in the higher energy $1T$ phase indicate a reconstruction of the structure and the formation of a charge-density wave at low temperatures.

DFT methods can compute the phonon spectrum of a material using either a finite displacement method[152] or density functional perturbation theory.[153] The unstable modes indicate the structural distortions that lead to the reconstructed structure. Creating appropriate

supercells of unstable structures and perturbing the atom positions using the eigenvectors of the imaginary modes, followed by structural relaxations, can provide candidate structures for low-temperature reconstruction.

It is important to note that structures that display unstable phonon modes at zero temperature, as determined by DFT simulations, may still be thermodynamically stable at elevated temperatures. The calculation of the Gibbs free energy of such phases is, however, exacerbated by the unstable phonon modes and requires sampling methods such as thermodynamic integration[170] or self-consistent phonons.[169,171]

2.5 2D Materials Discovery

The first step in successfully synthesizing novel 2D materials is identifying 2D structures that are thermodynamically metastable, as discussed in Sec. 2.4. Several approaches to predicting 2D structures have been reported in the literature, and they may be broadly categorized into two classes. The first class includes methods that rely on the structures of already known materials, whether 2D or bulk, to identify candidate 2D structures. Detailed descriptions of these approaches can be found in Secs. 2.5.1 and 2.5.4.

The second class of methods are algorithms that treat structure prediction as a global optimization problem. These optimization algorithms do not necessarily require knowledge of existing 2D or bulk crystal structures, and are therefore capable of performing unbiased searches for low-energy structures. However, global optimization algorithms generally require hundreds or thousands of objective function evaluations to achieve convergence. If DFT is used to relax candidate structures and compute their total energies, the computational cost of these structure searches can be considerable. Two such algorithms for structure prediction are described in Secs. 2.5.2 and 2.5.3.

2.5.1 Data Mining

Graphene was originally obtained by mechanical exfoliation of graphite. This exfoliation is possible because graphite is composed of several stacked graphene layers, held together by weak vdW forces. There are many other vdW layered solids like graphite. As a result, efforts

a) Co_2NiO_6 (mp-765906)
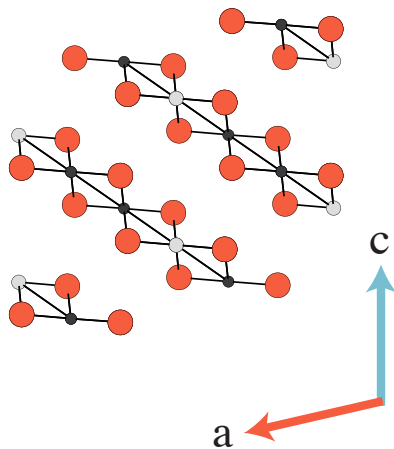
b) V_2O_5 (mp-25643)
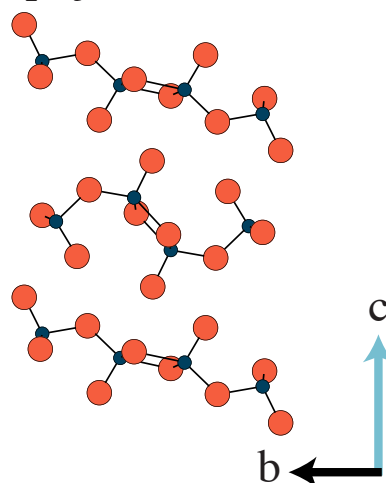
c) $Ge_2Te_5As_2$ (mp-14791)
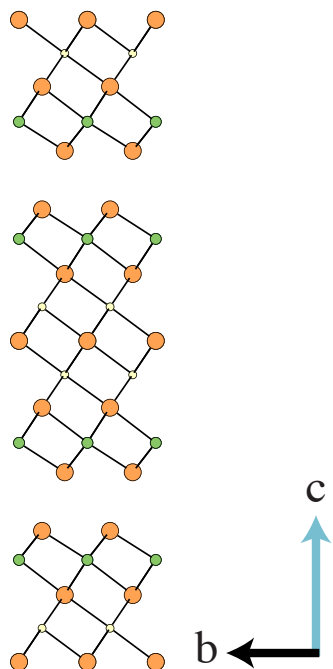
d) $Li\text{-}WCl_6$ (mp-570512)
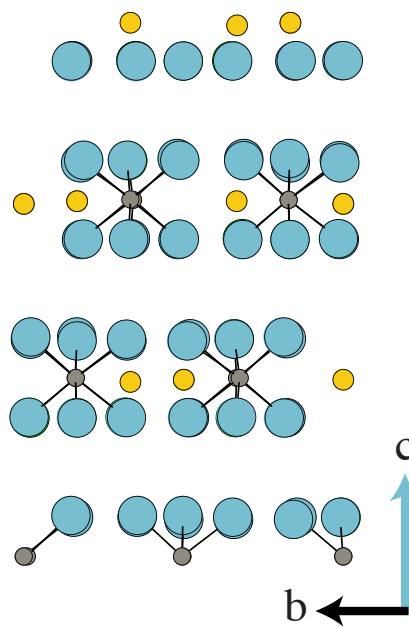
Figure 2-6. Example of structures that the topological scaling algorithm can find. This algorithm improves database searching by finding structures regardless of the gap direction (a), if the layers are intercalated (b), if the layers are very thick (c), and molecular structures that appear layered (d). Reproduced with permission from [22]. Copyright 2017 by American Physical Society. https://doi.org/10.1103/PhysRevLett.118.106101

have been made to identify other layered bulk materials from which single layers could be isolated to form feasible 2D materials.

During these searches, databases of bulk crystal structures are screened to identify materials with layered features. To find new transition metal dichalcognide 2D materials, Ding *et al.* considered materials that are chemically similar to MoS_2, which is known to form a layered vdW structure.[108] The bulk structures of these chemically similar compounds were identified in a database and found to display layered features, leading to several promising candidate 2D materials.

A more thorough search of crystal structure databases was performed later by Lebègue *et al.*[28] They screened the Inorganic Crystal Structure Database (ICSD)[172] for materials with vdW bonded layers. They used the following criteria to determine whether a material was layered: packing fraction between 0.15 and 0.5, gaps along the c lattice vector between crystallographic planes greater than 2.4 Å, and absence of covalent bonds spanning these gaps. In addition, only structures yielding high symmetry square or hexagonal monolayers were considered. This filter was applied to all the structures in the ICSD to identify 92 single layer compounds.

Ashton et al. recently developed another algorithm to identify layered structures.[22] This algorithm identifies networks of bonded atoms within the unit cell based on overlapping atomic radii. A 2×2×2 supercell is then created, and the atoms are again grouped into bonded networks.

By comparing the number of atoms in the bonded network before and after forming the supercell, the dimensionality of the network can be determined. 2D layers display periodicity in only two dimensions, so if the the cell is doubled in each dimension, the network size in a layered structure will increase by a factor of 4, while in a conventional bulk structure it will increase by a factor of 8.

This algorithm correctly identifies several unusual layered materials, shown in Figure 2-6, such as layered crystals in which the gap between adjacent layers is undulated instead of planar. In addition, this algorithm does not rely on a particular crystallographic representation
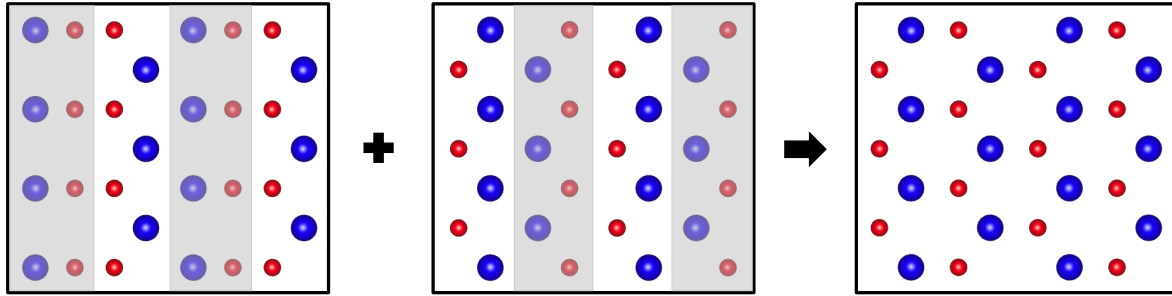
Figure 2-7. Illustration of the mating operator.[60] Sections are sliced from each parent structure, shown on the left, and combined to form an offspring structure. Supercells are shown for clarity. Reprinted figure with permission from [60]. Copyright 2016 by the American Physical Society. https://doi.org/10.1103/PhysRevB.93.054117

of layered structures (*e.g.*, layers oriented normal to the c lattice vector) to be successful, can identify very thick layers, and discerns between 2D layered materials and those composed of 1D chains or 0D molecules. Over 800 layered materials with reasonable thermodynamic stability were identified by applying this algorithm to the structures in the Materials Project database. Monolayers from these materials can be found in the 2D materials database at materialsweb.org.

2.5.2 Genetic Algorithms

In recent years, genetic algorithms have proven to be a useful approach to solving the global optimization problem. Genetic algorithms are inspired by the idea of biological evolution, as they evolve a population of candidate solutions over time. In the course of the algorithm, each structure is assigned a fitness. This is a measure of how low a structure's formation energy is relative to the other structures in the population. Structures with higher fitnesses are preferentially selected to create offspring, who are then evaluated and added to the population.

Offspring structures are primarily generated with a mating operator, which essentially slices a chunk from each of two parent structures and combines them together to form an offspring structure, as illustrated in Figure 2-7. The mating operator is successful because it passes local structural traits from parents to offspring, and formation energy is largely

a function of local structure. Over time, this causes structural traits correlated with low formation energy to propagate in the population, and traits causing high energy to die out.

At least two modifications are usually required in order to apply genetic algorithms to search for 2D structures. The first involves constraining the search to the 2D regime, which is usually accomplished by enforcing a constraint on the thickness of the 2D structures considered by the algorithm. The second modification is needed because most codes for computing a structure's total energy assume periodicity in all three dimensions. Therefore, vertical vacuum padding must be added to 2D structures before their energies are computed to prevent them from interacting with their periodic images. It should be noted that the first modification can prevent the discovery of some monolayers if the thickness of that monolayer is greater than the imposed restriction.

Unlike some other methods for crystal structure prediction, genetic algorithms are not necessarily limited to searching spaces of fixed dimensionality. This is important because the number of atoms in the lowest energy structure is not usually known *a priori*, and even the compositions of the thermodynamic ground states cannot necessarily be assumed.

The key to a successful genetic algorithm optimization is maintaining diversity in the population. Deep local minima in the energy landscape have the chance to trap the algorithm and imply the global minimum has been reached. Thus, most algorithms have ways to perturb a population so that local minima can be escaped. These methods include swapping positions of atoms in unit cells, increasing/decreasing the lattice vector magnitudes, translating atoms in the unit cell, and adding randomly generated structures to the population.

Several authors have applied genetic algorithms to search for 2D structures of boron,[173–176] carbon,[177] C_nO compounds,[178] InP and the C-Si and Sn-S 2D phase diagrams,[60] and group IV dioxides.[107] Publicly available codes that implement genetic algorithms for 2D crystal structure prediction include USPEX,[179] EVO,[173] and GASP.[180] A more in depth review of the genetic algorithm method has been conducted by Revard *et al.*[181]

2.5.3 Particle Swarm Optimization

Particle swarm optimization (PSO) is another heuristic approach that has been successfully applied to predict 2D crystal structures. The algorithm starts with a group (swarm) of randomly generated structures (particles) and then moves the particles in the swarm through the solution space. Specifically, a particle is shifted by a vector that is the weighted sum of three components: the particle's previous shift, the difference between the particle's current position and the best position previously seen by the particle, and the difference between the particle's current position and best position seen by the entire swarm of particles, where the weights on the latter two terms are drawn from a uniform distribution. Once a structure has been shifted, its energy is recomputed. In this way, the swarm of particles gradually converges toward the global minimum of the potential energy surface.

A PSO algorithm for 3D crystal structure prediction[182] was initially modified to search for completely planar structures.[183] The algorithm was later modified further to search for 2D structures with non-zero thicknesses.[184,185] Note that the modifications needed to enable 2D structure searches are essentially the same as those made to genetic algorithms: a constraint on the thickness of the 2D structures and the addition of vertical vacuum padding.

The modified PSO algorithm has been applied to several 2D systems containing boron and carbon.[178,183,186–189] However, most the these searches were restricted to completely planar structures, and the formation energies of the predicted 2D materials relative to the competing bulk phase(s) were not reported. As a result, one should determine their hull distance or surface energy before pursuing further research on these materials.

2.5.4 Chemical Substitution

Chemical substitution is perhaps the most straightforward way to find novel 2D materials. The method entails taking known 2D structures, discovered from the previously described methods, and substituting different species at the atomic sites. This approach is simple and computationally inexpensive, making it a good first step to identify promising structures in a 2D system. It should be noted that chemical substitution does not usually lead to new

structures (unless significant changes occur during structural relaxation), but rather to new site decorations of known lattices. As the collection of known 2D structures grows, this method becomes increasingly useful.

There are several methods to increase the accuracy of chemical substitution searches. First, one can use chemical intuition in order to decide what structures and elements to use in the substitution. If the elements substituted into a structure are likely to exist in uncommon oxidation states, they can often be screened out. Second, one can increase the number of structures used in the substitution for a given set of elements. Using 2D material databases, one can obtain a list of of structural templates based on known structures for a given ratio of elements. This allows for more certainty that the lowest energy structure has been discovered. Third, one can simulate supercells of a given structure rather than a single unit cell. While this increases the computational cost, using supercells enables the study of structural distortions and different magnetic configurations, which are not accessible with a single unit cell and may lower the system's energy.

Ciraci *et al.* and Şahin *et al.* used this method to discover group IV and group III-V binary monolayers.[32,33] 2D transition metal dichalcogenides and dioxides with the $1T$ and $2H$ structures have also been identified with chemical substitution,[190] as well as group III-V single layer materials with a tetragonal structure.[34]

2.5.5 Etching

Bulk materials databases can also be screened for materials that can be chemically etched to form 2D materials. This can be done by looking for bulk structures with repeating layers composed of galvanically active elements (*e.g.* Al) that can be dissolved by an acid. The details of a typical etching reaction are discussed in greater detail in Sec. 2.12, but one can approach discovering these precursors from a computational perspective. By taking a known precursor phase and replacing some of its elements, one can sometimes discover novel bulk phases with the potential to yield novel 2D materials after selected layers of the crystal are dissolved.
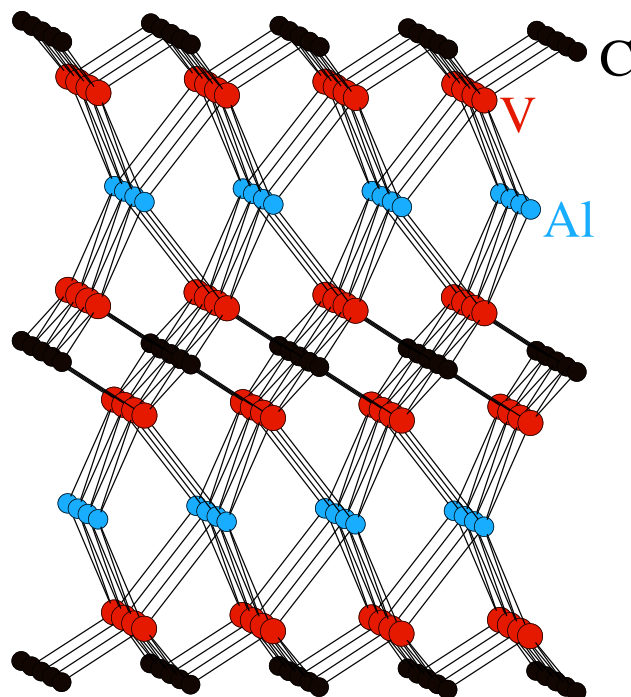
Figure 2-8. The V_2AlC MAX phase. The Al atoms can be etched away with an appropriate acid, leaving behind V_2C monolayers. The surfaces of these monolayers can then be passivated to obtain stable 2D materials. Reprinted figure with permission from [191]. Copyright 2016 by the American Physical Society. https://doi.org/10.1103/PhysRevB.94.054116

One example of such a precursor phase is the MAX phase structure, shown in Figure 2-8. HF can be used to selectively etch layers from these materials, leaving behind transition metal carbide/nitride monolayers known as MXenes. The majority of successful etchings have had Al as the dissolved layer.[83,191–197] The newly exposed transition metal surfaces can then be passivated with anions such as oxygen.[53]

Obtaining insight into an etching process from a computational framework is challenging, and requires an accurate understanding of the relevant competing phases for the original bulk material, as well as for the desired 2D material, as a function of pH and choice of acid. A possible route to obtain this information is briefly described in the next section.

2.6 Environmental Interactions

2.6.1 Stability in Water

A 2D material's stability in an aqueous environment is quite different from its dry stability. The most straightforward reaction pathway for a 2D material to decompose in water generally involves the formation of ions and molecules in solution that would not form in air. Consequently, understanding a 2D material's stability in water requires considering these ions and molecules as competing phases when constructing its aqueous phase diagram.

To construct these phase diagrams computationally, it is expedient to use experimentally obtained formation energies of solvated ions and molecules that are difficult to calculate accurately in DFT. These experimental formation energies can be used in the same framework as the DFT-calculated formation energy of a 2D material after they are shifted based on the difference in experimental and DFT formation energies of a known reference material.[198]

The free energy of each species in an aqueous environment is a function of concentration, pH, and applied potential in the solution, according to

$$G_i(c_i, pH, \phi) = G_i^0 + 0.0591 \log c_i - n_O \mu_{\mathrm{H_2O}} + + pH(n_H - 2n_O) + + \phi(-n_H + 2n_O + q_i) \quad \text{(2-2)}$$

where c_i is the concentration, n_O and n_H are the respective numbers of oxygen and hydrogen atoms in the species, $\mu_{\mathrm{H_2O}}$ is set to the formation energy of water of -2.46 eV, ϕ is the electric potential, and q_i is the species' charge. The variable nature of G_i enables the construction of Pourbaix diagrams, which plot a material system's stable phases as a function of pH and voltage. Therefore, these diagrams show what values of pH and voltage (if any) one can expect a given 2D material to remain stable and not dissolve.

As an example, the Pourbaix diagram generated for 2D SnO_2, where all ionic concentrations are set to 10^{-3} M, is provided in Figure 2-9. SnO_2 has a large region of stability, indicating this material is likely to remain undissolved in water under normal conditions.
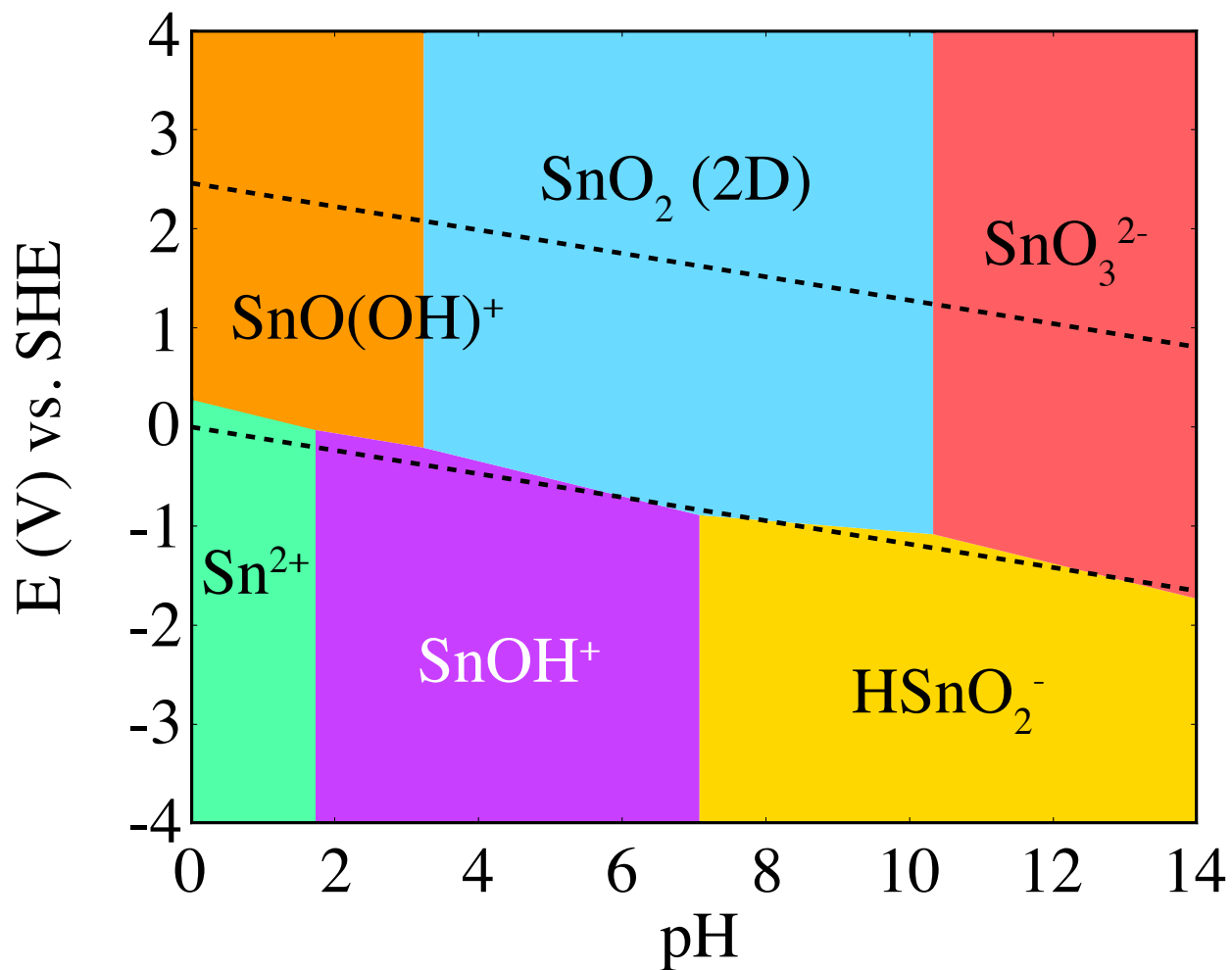
Figure 2-9. Pourbaix diagram for 2D SnO$_2$. The region between the dashed red lines represent the range of stability for H$_2$O. The light blue region is the range of pH and applied voltage in which SnO$_2$ is most stable. Derived from materialsweb.org.[22]

2.6.2   Sensitivity of Properties to Gaseous Molecules

2D materials, when used in applications, are not isolated in vacuum. Thus, finding the impact of gaseous molecules on 2D materials is an ongoing area of research. The majority of research has been on graphene and TMDCs, especially MoS$_2$, and so the following section focuses on these classes of monolayers.

Determining adsorption energies of molecules on 2D materials is not unlike the process for bulk material surfaces, and requires the careful selection of adsorption sites and orientations of the gaseous molecules.
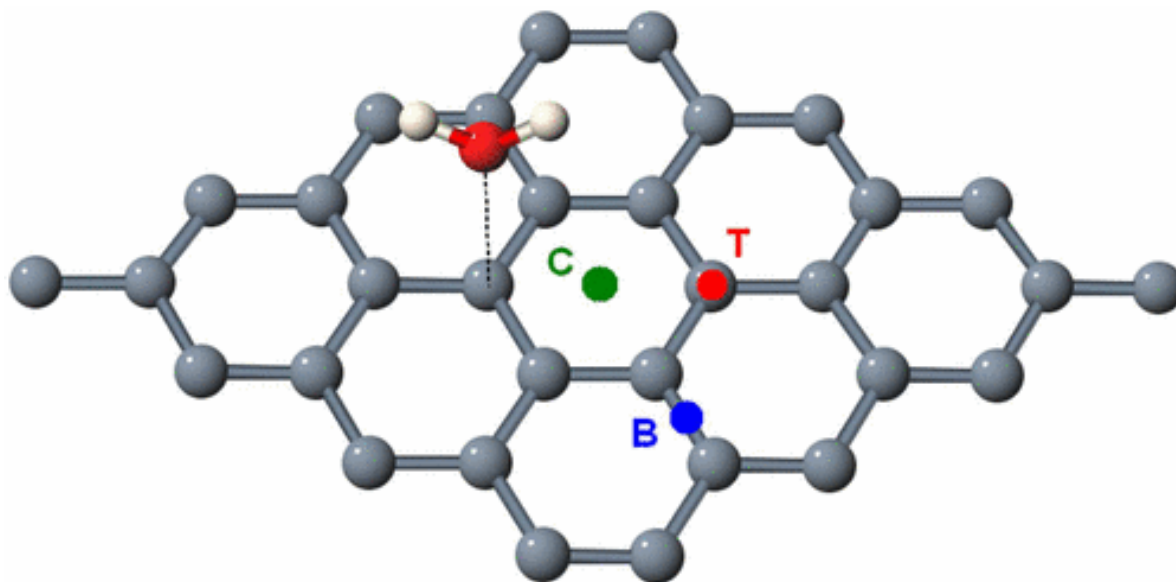
Figure 2-10. The adsorption sites of gases on graphene. The three potential sites of adsorption on graphene are above a carbon (T), between two carbons (B), and in the center of a carbon ring (C). Reproduced from [200]. Copyright 2008 by the American Physical Society. https://doi.org/10.1103/PhysRevB.77.125416

One also needs to decide what environment to calculate the adsorption energy in. Adsorption in vacuum is often a sensible choice and is the default in most DFT codes. To investigate adsorption in an aqueous environment, it is necessary to include a solvent either implicitly[199] or explicitly by adding the solvent molecules in the DFT calculation. If the adsorbate is charged, such as OH^- or H^+, then explicit solvation is required.

2.6.2.1 Graphene

The primary motive for investigating interaction between graphene and gaseous molecules has been for sensor detection. This detection usually relies on measuring any changes to graphene's conductivity upon the introduction of adsorbates.[200–203]

There are three primary sites of adsorption, as shown in Figure 2-10: on top of a carbon atom (T), between two carbon atoms (B), or in the center of the hexagon ring (C). For atoms and simple molecules, there are only a few possible orientations relative to the surface.[204] Additional orientations must be considered for more complex molecules.

Leenaerts *et al.* used DFT to investigate the interaction between pristine graphene and 5 gaseous molecules: H_2O, NH_3, CO, NO_2, and NO.[200] The adsorption energy, distance from the graphene surface, orientation, and charge transfer was calculated for each molecule. They found that H_2O and NO_2 act as p-type dopants, with NO_2 showing the greatest charge transfer from the surface. NH_3, CO, and NO act as n-type dopants.

Zhang *et al.* investigated graphene for sensing many of the above molecules.[205] They computed the adsorption energy and charge transfer of each molecule on graphene doped with P, B and N, and on graphene containing vacancies. They found that graphene with vacancies had the greatest adsorption energy for all molecules except NH_3, which bound tightest to B-doped graphene.

NH_3 and NO_2 have been found to remain as n-type and p-type dopants, respectively, regardless of the condition of the graphene sheet. CO is shown to have very little interaction with doped graphene, but acts as an n-type dopant on graphene with vacancies. NO acts as a slight to moderate n-type dopant for doped graphene, matching its behavior in pristine graphene, but behaves as a significant p-type dopant on graphene with vacancies.[205]

2.6.2.2 Transition metal dichalcogenides

The majority of research into how gaseous molecules affect the properties of transition metal dichalcogenides has been in the context of photo-luminescent devices. In a recent paper by Liu *et al.*, the impact of oxygen on MoX_2 and WX_2 monolayers was simulated using DFT.[206] They found that pristine monolayers were unaffected by the presence of oxygen. However, oxygen molecules have significant interaction with single chacolgenide vacancy defects, which is a very common defect in MoS_2 monolayers.[207–209]

Their results show that for MoX_2 and WX_2 (X=S, Se), O_2 molecules adsorb onto vacancy sites, flattening the highest valence band and increasing the effective mass of the holes compared to the pristine monolayers.[206] In $MoTe_2$ and WTe_2, O_2 was found to dissociate across the monolayer with one oxygen filling the vacancy and another bonding with a chalcogen atom. The resulting band structure shows that the electronic properties of these two monolayers is

largely unaffected by oxidation, making them ideal for device fabrication. The band structures of MoS_2 under all these scenarios are illustrated in Figure 2-11.

Oxygen can also dissociate across the other TMDCs, resulting in only slightly influenced electronic properties. However, thermal annealing is required to overcome the energetic barrier in most cases.[206] In both adsorbed and dissociated cases, the defect state introduced by the chacolgen vacancy disappears.

Tongay *et al.* found that nitrogen gas impacted the band structure of MoS_2 during photoluminescence experiments and investigated further using DFT simulations.[210] They found that, similar to Liu *et al.*, N_2 physisorbs only onto defect sites in MoS_2 at sulfur vacancies and di-vacancies, and that the defect states introduced by the vacancies disappeared when the N_2 interacts with the defects. In addition, the defect sites screened excitons when in vacuum, but after introducing N_2 to the system the free and bound neutral excitons were stabilized and contributed to the photoluminescence spectrum.

Interaction between monolayers and H_2O has been considered in Sec. 2.6.1. However, the context of that interaction is in regard to electrochemistry. Molecules of H_2O are present in air, and thus should be considered when determining monolayer behavior. As has been the trend so far, the molecule is found to interact strongly with sulfur defects in MoS_2.[209] The charge transfer from the monolayer to the molecule increases by a factor of 5 when comparing the adsorption to a pristine monolayer and a sulfur vacancy. The exact impact on the band structure was not explored, but it was found to improve the photo-luminescent intensity of MoS_2 by a factor of 10.

2.7   Electronic Properties

2.7.1   Band Structure

In a semi-infinite system where atoms are isolated from each other, all electrons have the same atomic energies. As the interaction among atoms increases and the atomic orbitals overlap, the energy levels hybridize and form continuous bands. However, the dimension of the material has an impact on the energy levels. When confining the system in any given direction,
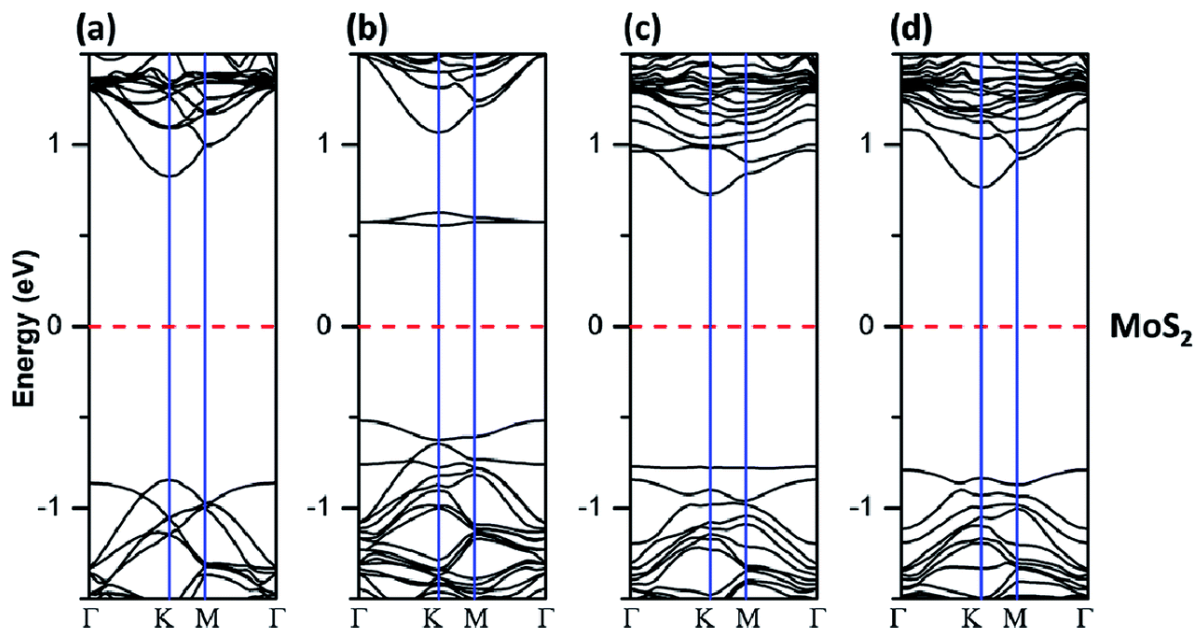
Figure 2-11. The band structure of MoS_2 under varying conditions. (a) represents the band structure of pristine MoS_2. (b) is the band structure when a S vacancy is present. (c) is the band structure when an O_2 molecule is adsorb to the defect. (d) is when the O_2 is separated into 2 oxygen atoms that adsorb to the monolayer surface. The defect states that decrease the band gap in (b) are disappear when O_2 adsorbs. Adapted from [206] with permission from The Royal Society of Chemistry. https://doi.org/10.1039/C4RA17320A

band energies are generally separated by quantized energy separations in a phenomenon known as quantum confinement. As a result, band gaps can appear in 2D materials derived from bulk metals, and band gaps can increase in 2D materials derived from bulk semiconductors or insulators.

These bands can be calculated using *ab initio* methods. The three most common methods are DFT with PBE functionals,[119] HSE hybrid functionals[123] as introduced in Sec. 2.3, and the GW approximation. A comparison of the band gaps and edges calculated with these methods can be seen in Figure 2-12 for SnS_2.

As discussed in Sec. 2.3, semi-local DFT functionals typically underestimate the band gap. Consequently, of the above methods, PBE yields the least accurate band gaps with an, on average, 50% underestimation as compare to experiment.[211, 212]

The HSE06 hybrid functional offers significant improvement compared to PBE. HSE06 includes a percentage of the short-range Hartree-Fock nonlocal exchange energy of Kohn-Sham orbitals and potential energy of exchange-correlation, while long range Hartree-Fock exchange energy is derived from the exchange-hole formalism of PBE. HSE06 functional still, on average, underestimates bandgap energy, but is significantly closer than the PBE functional.

The GW methods predicts a band gap very close to experiment. In this method, starting from a converged Kohn-Sham DFT band structure, the RPA screened Coulomb interaction W is used to construct the exchange self-energy diagram G·W, giving rise to a dynamical potential for the single electron Green's function G. The method approximates the Hedin equations by replacing the interacting electron vertex with the bare one and, in some flavors, omitting self-consistence.

There are three flavors to computer implementation of GW method: G0W0, GW0 and pure GW.[131] The G0W0 approach holds the Green's function G and screened Coulomb's potential fixed across iterations, leading to a non-self-consistent solution. On the other hand, GW0 iterates over G while it keeps W constant, which gives the partially self-consistent solution that matches the experimental data the best. Pure GW method iterates over both G and W, which yields completely self-consistent solutions. This method gives similar results to GW0, but is significantly more computationally expensive.

The effective mass of electrons can be approximated in the same way as in a bulk geometry. In the general case, the electron accelerate according to the mass tensor

$$M_{i,j0}^* = \hbar^2 (\mathrm{d}^2\mathrm{E}/\mathrm{dk_i}\mathrm{dk_j})^{-1}, \tag{2-3}$$

while in some cases where the band structure is isotropic, the above simplifies to the relation $m_0^* = \hbar^2/(\mathrm{d}^2\mathrm{E}/\mathrm{dk}^2)$. Knowing the effective mass of an electron and hole in a 2D material is useful for numerous applications, especially when building electronic devices. Having a lower effective mass allows for faster electron transport, and thus improved functionality from the device. The accuracy of the effective mass is dependent on the accuracy of the methods used
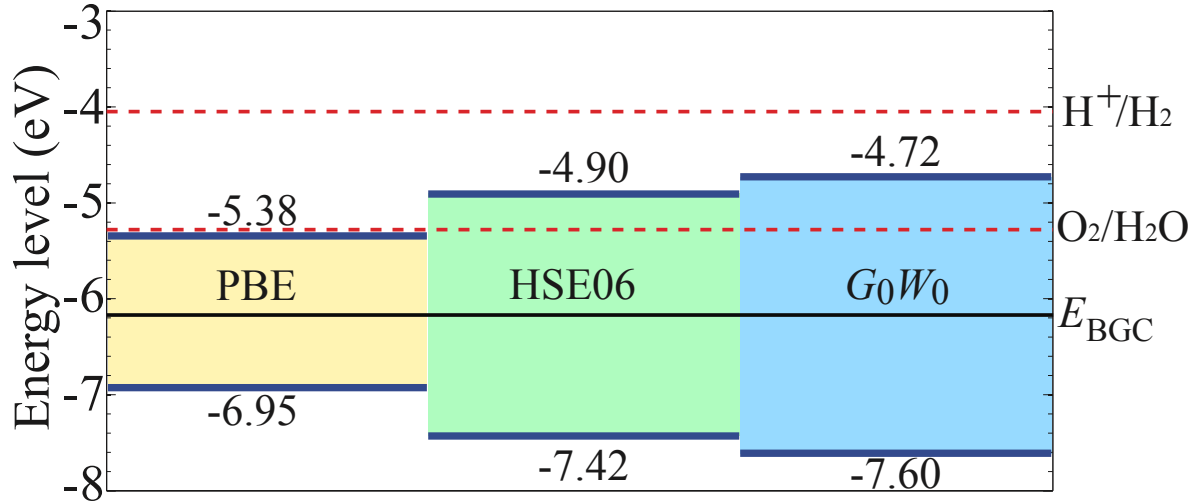
Figure 2-12. The calculated band edges of SnS_2 using PBE, HSE, and GW methods. The more accurate the method the larger the predicted band gap. The HSE band gap is 60% larger than the PBE, while the G_0W_0 band gap is 14% larger than the HSE. Reproduced from [213]. Copyright 2013 by the American Physical Society. https://doi.org/10.1103/PhysRevB.88.115314

to calculate the bands. For example, GW is able to include dynamic Coulomb interaction effects not captured in PBE or HSE functionals, potentially changing the curvature of the bands.

2.7.2 Optical Absorption and Excitations

2.7.2.1 Fundamentals of light absorption

Light absorption and emission by a material requires conservation of energy, momentum, angular momentum, and spin. In the optical range of the spectrum, transitions must conserve energy in the eV range, *i.e.* typical optical transitions involve electronic excitations between filled and empty states. Since the photons carry very little momentum, the change in momentum of the electron is negligible unless phonons are involved in the transition. This means optical transitions occur vertically between occupied and empty states in the band structure, else they require the emission or absorption of a phonon. During an optical transition, the electron spin must be preserved when spin-orbit interactions are negligible. The magnetic quantum number must either remain the same or change by one, and the angular momentum

quantum number must change by one. With these rules, which optical transitions are allowed can be calculated and be used to characterize the optical properties in materials.[214]

Following the excitation of an electron from a filled valence band state into an empty conduction band state by absorption of a photon, the electron will eventually relax to lower energy states. This relaxation can occur in two ways: radiatively or non-radiatively. The former results in light emittance and is often independent of phonons. The latter requires phonon emission to dissipate the energy and change the momentum. Radiative processes can also involve phonons, though the rate of these processes is typically smaller than for direct transitions.

When an electron is optically excited across the band gap of a material, the resulting hole state in the conduction band interacts with the electron in the valence band state. The bound state between the electron and hole is called an exciton. These excitons can either be localized at crystallographic sites, so-called Frenkel excitons,[215] or freely move through the material as so-called Wannier-Mott excitons.[216] Furthermore, excitons can exhibit a net positive or negative charge, which occurs when an additional hole or electron, respectively, binds with the original electron-hole pair to form a trion.[217,218]

Since the Kohn-Sham equations of DFT map the electronic system onto a system of non-interacting electrons, other computational methods and corrections are necessary to accurately calculate the properties of excitons, which are inherently interacting two-particle excitations. Thus, GW methods and Bethe-Salpeter equation (BSE) calculations are often used to determine optical absorption and emission properties and exciton binding energies. As an example, Fig. 2-13 shows that the binding energy for the exciton in 2D SnS_2 calculated with the BSE is 0.4 eV.[213]

The computational expense of the BSE makes routine calculations of the exciton binding energy difficult. To estimate the exciton binding energy, the Mott-Wannier model[219] can be applied to 2D materials.[213,220] This model approximates the exciton binding energy as the binding energy between an electron and a hole embedded in a dielectric continuum. In two
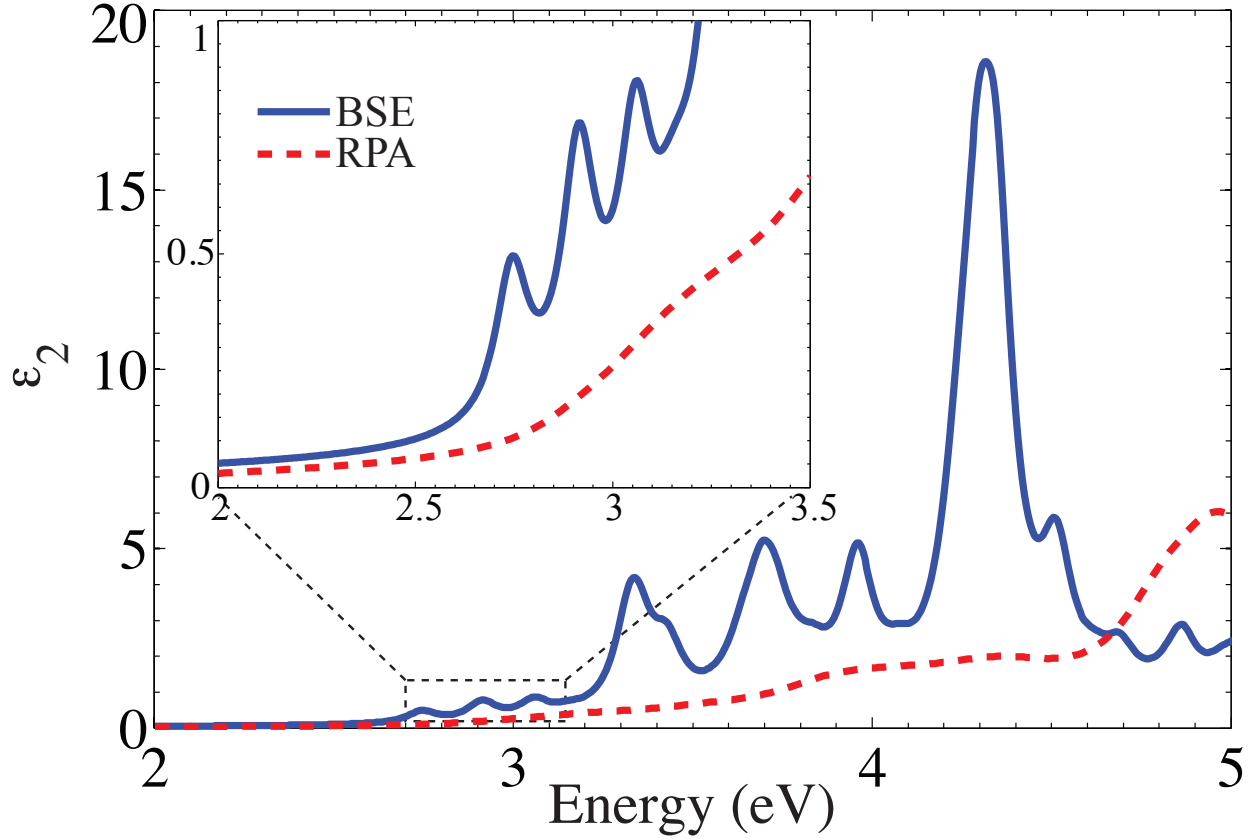
Figure 2-13. Calculation of the exciton binding energy in 2D SnS_2 using the Bethe-Salpeter equation (BSE). The inset shows a close-up of the imaginary part of the permittivity, ϵ_2 with three exciton peaks. To compensate for the bandgap underestimation using the PBE functional in the RPA calculation, the spectra are shifted by 1.0 eV, which is the difference between the HSE06 and PBE bandgaps. Reprinted with permission from Ref. [213]. Copyright (2013) by the American Physical Society.

dimensions, the first excitonic binding energy is

$$E_0 = 4\frac{m_\mathrm{r}}{m_0}\frac{R_\infty}{\epsilon_{2\mathrm{D}}^2}, \tag{2-4}$$

where m_r is the reduced effective electron mass, m_0, the rest mass of the electron, $\epsilon_{2\mathrm{D}}$ the effective permittivity, and R_∞ the Rydberg constant.[219] For 2D systems, care must be taken in the calculation of the permittivity tensor to account for the size of the simulation cell, *i.e.* the thickness of the vacuum layer.[213] The contribution of the vacuum to the computed permittivity tensor elements can be corrected using the linear law, $\epsilon_\mathrm{calc} = f\epsilon_{2\mathrm{D}} + (1-f)\epsilon_\mathrm{vac}$, where f is
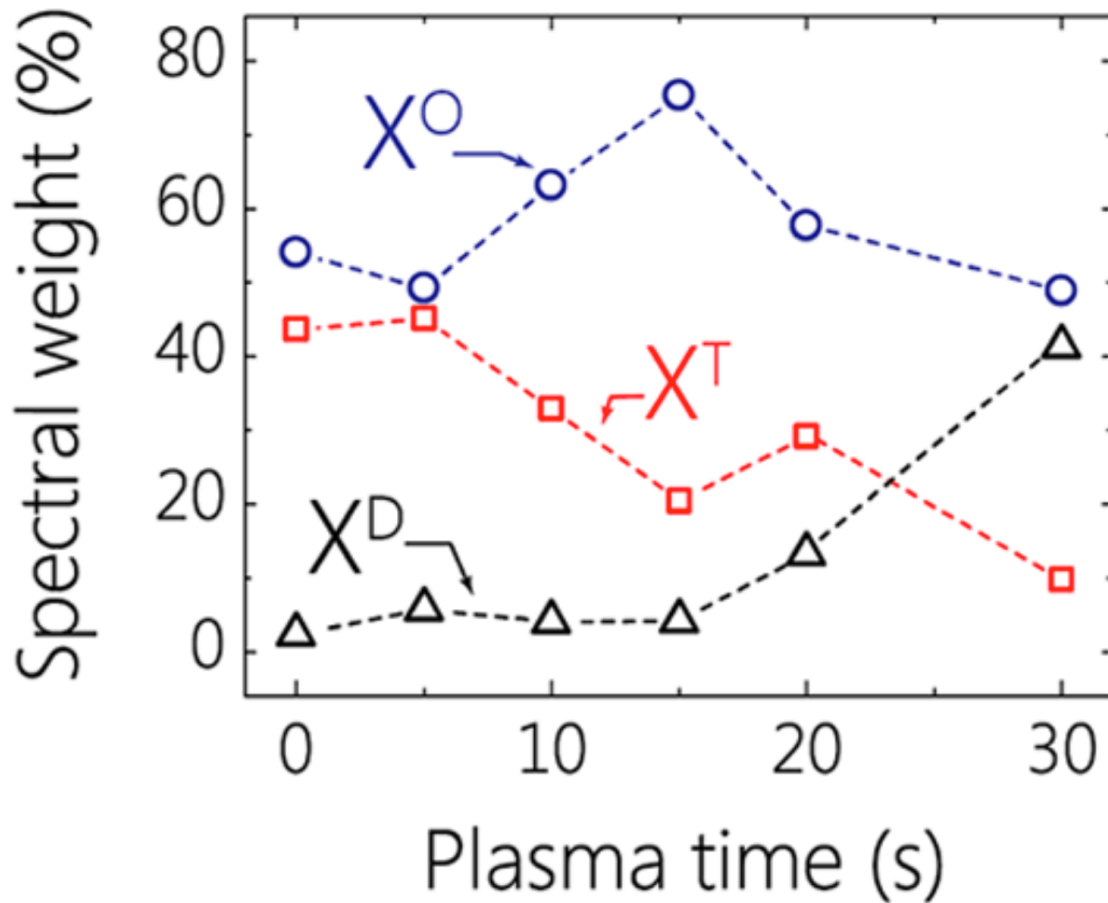
Figure 2-14. The spectral contribution of excitons to the emission spectra of monolayer WS_2 as plasma time, the source of defect generation in the monolayer, increases. As plasma time increases and more defects are present, the contributions by the negative trion contribution (X^T) decreases, by the neutral exciton (X^0) fluctuates somewhat, and by the defect bound excitons (X^D) increases significantly. Adapted with permission from [221]. Copyright 2015 American Chemical Society. https://doi.org/10.1021/nn5073495

the volume fraction of the 2D structures in the simulation cell, $\epsilon_{vac} = 1$ is the permittivity of vacuum, and ϵ_{2D} is the permittivity of the 2D material.[213]

For SnS_2, the exciton binding energy predicted from the Mott-Wannier model is identical to the binding energy calculated by solving the BSE. While such perfect agreement is probably fortuitous, it nevertheless indicates that the simple approximation can provide insight into the excitonic properties of 2D materials.[107]

2.7.2.2 Photonic devices

Graphene absorbs 2.3% of visible light,[222] which is surprisingly high considering its only one atom thick. TMDCs have shown even higher amounts of absorption, ranging from 5-10% depending on the wavelength.[223] Combined with the flexibility of 2D materials, this has led to investigations into their potential in photovoltaic[224,225] and luminescent devices.[210,221,226] These behaviors are intrinsically linked due to the above transition rules dictating both processes. At present, these materials do not outperform those in commercially available devices.

It has been found that excitons dictate the optical emission spectra of 2D materials. For photoluminescence (PL) based electronics using 2D materials, both WS_2[221] and MoS_2[210] have had their photo-luminescent spectra measured before and after the introduction of point defects. Prior to defect introduction, the spectra are largely dominated by a peak corresponding to a negative trion in MoS_2 and a mixture of trion and neutral exciton contributions in WS_2. As point defects are introduced to the monolayers, a lower energy peak associated with defect bound excitons arises. A higher energy peak associated with neutral excitons appears to envelop the trion peak, and the overall PL increased as more defects were introduced. In WS_2, the trion contribution is found to disappear almost entirely. The spectral contribution of each exciton after different plasma times, *i.e.* with increasing defect density, can be seen in Figure 2-14.

Electroluminescence (EL) is also feasible through heterostructure design. Withers *et al.* developed graphene|*h*-BN|MS_2|*h*-BN|graphene (M=Mo,W) heterostructures which displayed EL spectra nearly matching the PL spectra of the isolated monolayers.[226] These devices operate by electrons and holes tunneling from the metallic leads (graphene) through a thin tunneling junction (*h*-BN) into a semiconductor with a band gap in the visible range (MS_2). Like in the PL device, it is found that the trion and bound neutral defects dominated the emission spectra of the device.

In summary, excitons are crucial to the optical behavior of 2D materials. However, accurately predicting how monolayers will respond to optical excitation is difficult at this time due to the computational costs. Simulating excitons and point defects both have increased computational expenses, which is compounded when both are simulated at once. These calculations are within the realm of possibility on an individual basis, but high throughput simulations of this nature are difficult at this time.

2.7.3 Work Function/Ionization Potential

The work function of a solid is the energy it takes to move a single electron from the surface to a point far outside the solid. "Far" means here that the distance is large enough to suppress the local interaction with the surface but small enough to feel the macroscopic electro-magnetic fields of the solid. This definition is to make the work function a property of the surface only.[227] For 2D materials, the work function can be easily calculated. After converging the size of the vacuum, the local potential will reach a maximum in-between periodic replica which represents the vacuum according to the above definition. One can then find the difference between the Fermi level and the vacuum level to resolve the work function of the material.

2.7.4 Photocatalysis

One of the applications where two-dimensional materials have demonstrated the potential to outperform bulk materials is that of photocatalytic water splitting to derive hydrogen as a fuel.[4] Solar energy fuel generation provides a route to clean, environment friendly, and renewable energy production, but its practical application has been largely limited by poor efficiency of solar energy conversion.[228, 229] 2D materials present two intrinsic advantages in comparison to other nanostructures and bulk materials which enhance their photocatalytic efficiency. First, they exhibit high specific surface area for the redox reactions. Second, the photogenerated electrons and holes migrate to the surface more quickly due to the reduced dimensionality in the third direction, potentially reducing electron-hole recombination, thus
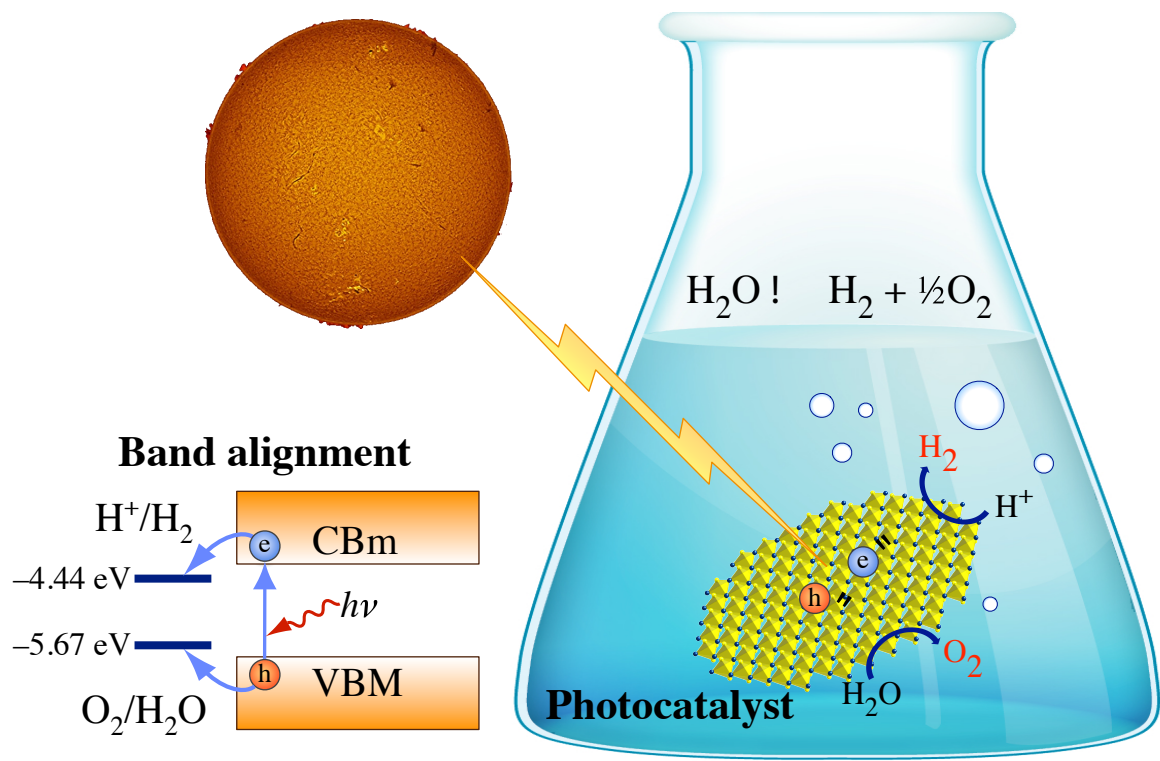
Figure 2-15. Schematic mechanism of photocatalytic water splitting. The minimum criteria for potential photocatalysts to show activity towards water splitting are (a) presence of a band gap larger than free energy of water splitting, 1.23 eV, (b) stability in water, and (c) the band edges of the photocatalyst should straddle the redox potentials of hydrogen and oxygen evolution. Adapted with permission from [4]. Copyright 2015 American Chemical Society.

increasing efficiency. In addition, 2D materials represent a large exploratory space of materials with tunable electronic, mechanical, and optical properties.[22,73]

There have been several experimental validations of enhancement in photocatalytic water splitting efficiency with the reduction in dimensionality in the vertical direction. For instance, freestanding single-layer SnS_2 is observed to provide high photocurrent density of 2.75 mA/cm^2, over 70 times higher than that of bulk SnS_2. In addition, it has an incident photon to converted electron ratio (IPCE) of 38.7% at an irradiation wavelength of 420 nm, in contrast to only 2.33% for bulk SnS_2.[230]

In another example, ZnSe with four atomic layers exhibits a photocurrent density of 2.14 mA/cm^2, about 200 times higher than the value for bulk ZnSe and an IPCE of 42.5%

Table 2-1. First-principles simulations have been used to predict several 2D photocatalysts

2D Material	Ref.
CrS_2	72
HfS_2	236
$(N_2H_4)_2Mn_3Sb_4S_8(\mu_3\text{-OH})_2$	237
MS_2 (M = Mo, W, Pt) and $PtSe_2$	238
MX (M = Ga, In; X = S, Se, Te)	239
MX (M = Ge, Sn, Pb; X = O, S, Se, Te)	166, 240
CdX (X = S, Se, Te)	241
TcX_2 (X = S, Se)	242
MPX_3 (M = Zn, Mg, $Ag_{0.5}Sc_{0.5}$, $Ag_{0.5}In_{0.5}$; X = S, Se)	243
$MPSe_3$ (M = Fe, Mn)	244
$AlSiTe_3$, $InSiTe_3$, Al_2Te_3, B_2S_3, As_2X_3 (X = S, Se, Te)	58
β-MNX (M = Zr, Hf; X = Cl, Br)	245
α-MNX (M = Zr, Hf; X = Cl, Br, I)	245
TiNM (M = Cl, Br)	246
BiOX (X = Cl, Br, I)	247, 248
Zr_2Co_2, Hf_2Co_2	249

compared to 0.25% of the bulk counterpart.[231] Similar photocatalytic enhancements through the reduction of the dimensionality have been observed for other single and few-layer 2D materials such as SnO, SnS, SnSe, CdS, and WS_2.[230–235]

Theoretical investigations have been successful in identifying several potential photocatalysts by searching for 2D materials which have properties suitable for photocataytic water splitting. More than 50 2D materials have been predicted to show photocatalytic activity for water splitting, Table 2-1. The intrinsic properties which are desirable in a potential photocatalyst include, but are not limited to, a) high thermodynamic stability, b) a band gap larger than the free energy of water splitting, c) large visible light absorbance efficiency, d) suitable band edge alignment with respect to redox potentials of hydrogen and oxygen evolution reactions, and e) stability in water;[4, 250] see Figure 2-15. In addition, application of strain, chemical bias, and doping have been shown to enable the engineering of key photocatalyst properties such as band edge locations, band gap sizes, and optical spectra.

While several studies have explored the use of 2D materials as catalysts for hydrogen production, similar investigations focused on reduction of CO_2 for fuel generation have been

limited. Recently, Liang *et al.* have shown that single unit-cell Bi_2WO_6 layers can reduce CO_2 to produce 75 μmolg^{-1} h^{-1} of methanol, which is 125 times higher than that of bulk Bi_2WO_6. Apart from identifying potential photocatalysts, challenges in the generation of carbon-based fuels include the mitigation of low efficiencies due to loss of excitons to hydrogen generation and low product selectivity due to comparable redox potentials of the closely competing final reduction products.

2.7.5 Magnetic Insulators

As outlined in Sec. 2.8, some 2D materials display a net magnetic moment. When such monolayers also have a band gap, the band structure differs from non-magnetic insulators. The magnetism results in two sets of bands in the monolayer's electronic structure: one for up spin electrons, and one for down spin electrons. As stated in Sec. 2.7.2, electron spin must be preserved as an electron transitions from one band to another. This results in one band gap for up spin electrons, and different gap for down spin electrons.

One can use such materials in spintronic applications. Since there are two different band gaps, electrons in one spin channel often have a higher chance of exciting across the gap than electrons of the opposite spin. As a result, it is theoretically possible to build a transistor that improves its on/off current ratio by using a magnetic insulator. Combined with the small size of monolayers, this technology has the potential to significantly increase the performance of electronic devices and such materials are of great interest to spintronic research.

2.7.6 Half-Metals

Naturally, magnetism can also affect the bands in 2D metals. A standard ferromagnetic 2D material is one in which the two spin channels are metallic but not energetically degenerate. In some cases, however, one spin develops a band gap while the other remains metallic. Such materials are called half-metals, and an example of such a band structure is shown in Figure 2-16. The band structure shown in Figure 2-16 was calculated with the PBE functional, however, it has been demonstrated that HSE or other more accurate functionals are required to adequately assert the presence of a half-metallic band structure.[251]
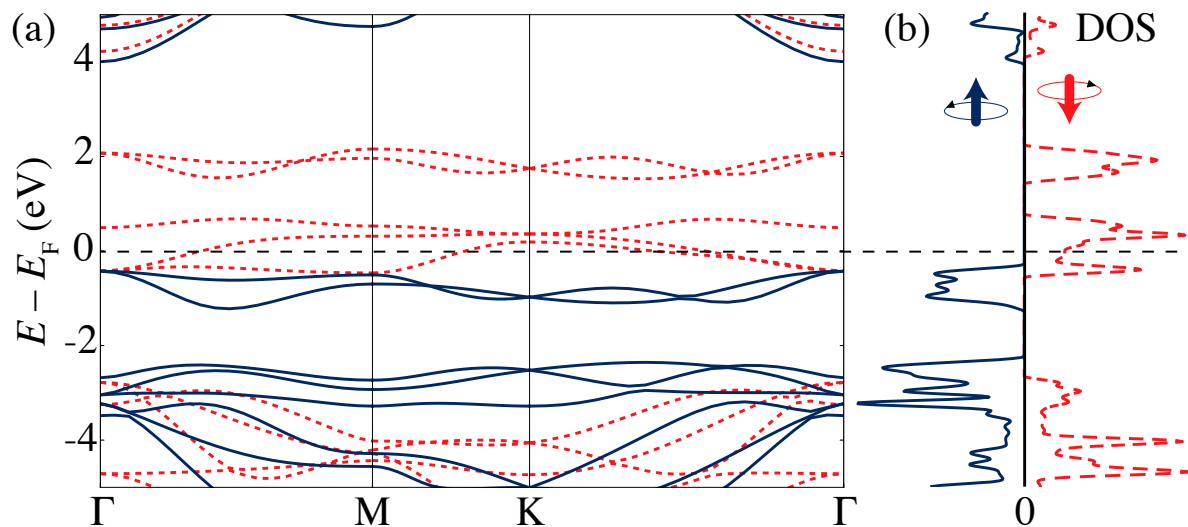
Figure 2-16. The PBE band structure and density of states of the FeCl$_2$ half metal. The solid blue lines represent the majority spin component and the dashed red lines the minory one. The minority spin electron bands cross the Fermi level and thus behave metallically, whereas the majority spin electrons exhibit a band gap. Reproduced with permission from [22]. Copyright (2017) by the American Physical Society.

Half-metallic behavior has recently been discovered in pristine 2D FeCl$_2$, FeBr$_2$, and FeI$_2$, all in the $1T$ structure.[251,252] It is understood that the half-metallic behavior in these materials strictly depends on their reduced dimensionality, since their multilayer forms have an interlayer antiferromagnetic (AFM) order.[253] Their half-metallic nature makes these materials very promising for spintronic applications. Designing a magnetic tunnel junction with half-metallic leads, in principle, enables the use of 100% spin-polarized currents, and in turn creates a very high ratio between the junction's on and off states.

2.8   Intrinsic Magnetism

2.8.1   Computational Treatment of Magnetism

Spin-polarized DFT can be employed to compute various magnetic properties of a 2D magnetic material. An initial guess at each atom's magnetic moment is required, and can typically be estimated using Hund's rule. During a self-consistent DFT calculation, the magnetic moment on each atom is optimized as the wavefunctions are determined.

For a ferromagnetic (FM) 2D material, a single unit cell is sufficient to describe the magnetic configuration. In contrast, calculations of antiferromagnetic (AFM) materials often require supercells. This is to allow for various distributions of up and down spins across the material. For example, Sivadas *et al.* considered three types of AFM structures in 2D $CrSiTe_3$: Néel, zigzag, and striped.[254] This is an example of how a complete assessment of antiferromagnetism in a material is more complicated and computationally expensive than that of ferromagnetism.

Having obtained the ground state magnetic structure, it is worthwhile understanding the underlying mechanism that causes the magnetic ordering. Depending on whether the system is metallic or semiconducting, the Stoner and Heisenberg exchange models are respectively useful for understanding the exchange interactions.

The magnetocrystalline anisotropy energy (MAE) is an important parameter that should be calculated. This is because a significant MAE is required for a 2D system to exhibit a long-range order, which is deemed impossible according to Mermin and Wagner.[44] That said, there exist two notable exceptions to the applicability of the Mermin-Wagner theorem: the Ising and the Berezinsky-Kosterlitz-Thouless systems,[255] both of which exhibit sizable MAEs. The MAE can be calculated by the torque method[256] via non-collinear calculations including spin-orbit coupling. In these calculations, the spin directions are fixed while the magnetic moments are optimized. This allows one to plot the energetic stability of the material as the magnetic moment points in various directions, and thus find which direction is the ground state. If the magnetic moment is equally stable in every direction in the plane of the monolayer, it is considered an "easy plane". If the most stable position is perpendicular to the plane, it is considered an "easy axis" monolayer.

2.8.2 Ferromagnetism, Anti-ferromagnetism, Ferrimagnetism

Existence of magnetic order offers an additional degree of freedom for controlling electrical properties of 2D materials. As such, magnetic 2D materials hold great promise for applications in novel electronic devices. Recently, a number of 2D materials have been predicted via DFT

calculations to exhibit ferromagnetic and antiferromagnetic order. These 2D materials are often binary compounds consisting of transition-metal and chalcogen elements such as VS_2, MnS_2, $MnSe_2$, and FeS_2.[257–259] Ternary compounds form a separate group of magnetic 2D materials with a general chemical formula of ABX_3 (A=V, Cr, Mn, Fe, Co, Ni, Cu, Zn, B=P, Si, Ge, Sn, and X=S, Se, Te).[260–263] It is worth emphasizing that most of the above mentioned 2D materials possess an interesting combination of magnetic order and semiconducting properties. The critical temperature (Curie or Néel) of the predicted magnetic 2D materials can range from a low temperature (*e.g.* 90 K for 2D $CrSiTe_3$[262]) to several hundred Kelvin (*e.g.* 675 K for 2D CrN[264]), computed based on Monte Carlo simulations.

The interest in magnetic 2D materials is not only reflected by emerging theoretical studies. Experimental groups have also provided evidence of magnetic order in 2D materials. For example, Gong *et al.* confirmed the intrinsic long-range ferromagnetic order in 2D $CrGeTe_3$ via scanning magneto-optic Kerr microscopy.[265] Another recent experiment performed on monolayer chromium triiodide CrI_3 reported intriguing magnetic properties that are strongly dependent on the number of monolayers.[266]

2.8.3 Anisotropic Magnetism

In addition to magnetic order, magnetocrystalline anisotropy (mainly due to spin-orbit coupling) is another critical property that could widen the applications of magnetic 2D materials. Here, DFT simulations play similarly important roles in computationally identifying potential magnetic 2D materials with strong magnetocrystalline anisotropy. For instance, Zhuang *et al.* have shown that single-layer $FeGeTe_3$ exhibits a significant magnetocrystalline anisotropy energy (MAE, see Fig. 2-17), which make this single-layer material potentially useful for magnetic recording applications.[267] It is natural to expect that more theoretical efforts will be spent searching for new 2D materials with strong magnetocrystalline anisotropy capable of withstanding thermal fluctuations at high temperatures.
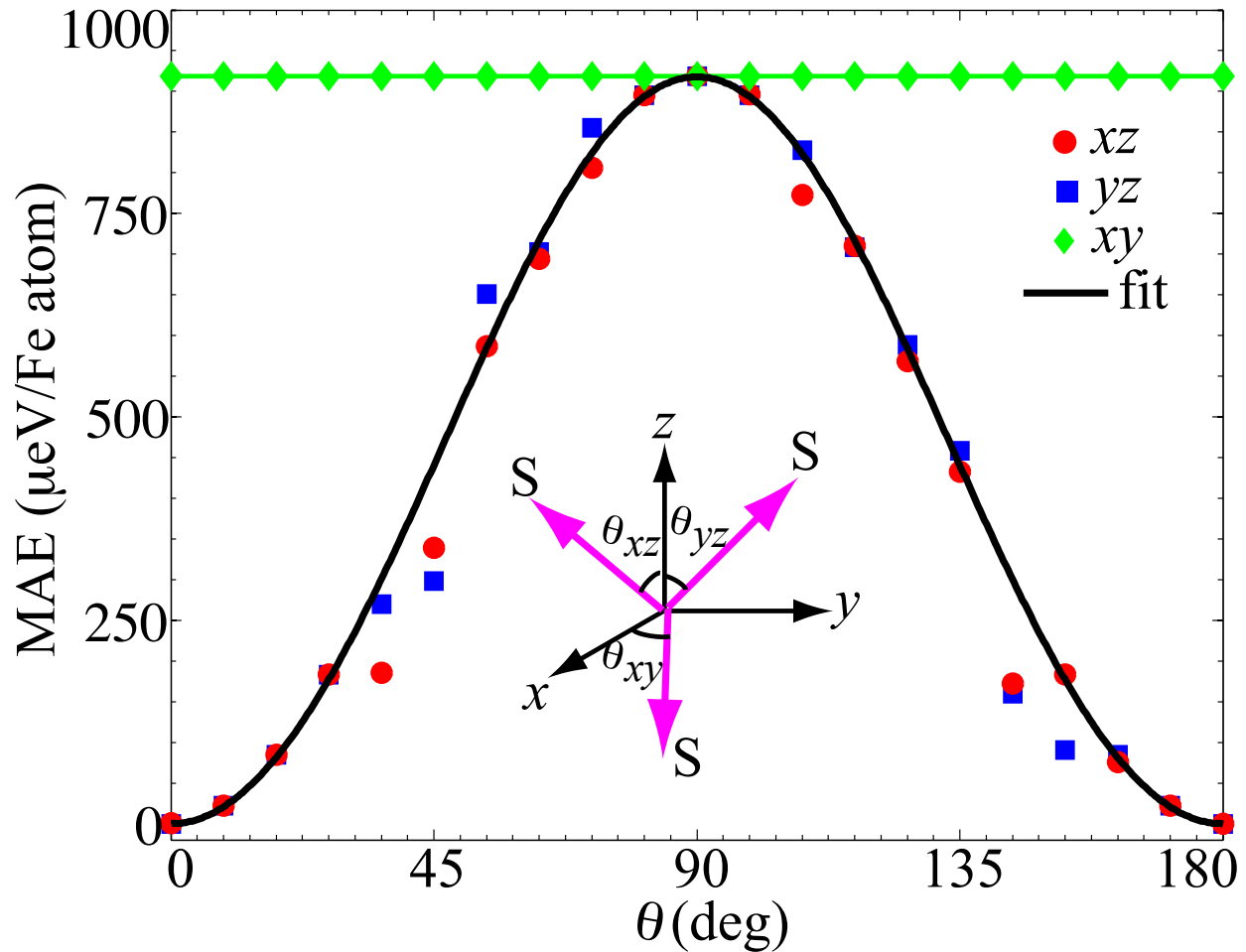
Figure 2-17. Magnetic anisotropy energy in FeGeTe$_3$. As can be seen, the z direction is most stable for the direction of the magnetic moment in the monolayer, while in-plane rotation has no barrier. Reprinted figure with permission from [267]. Copyright 2016 by the American Physical Society.
https://doi.org/10.1103/PhysRevB.93.134407

2.9   Superconductivity

According to the Mermin-Wagner theorem[44] a 2D system cannot become superconducting because the long range fluctuations of the spontaneously broken symmetry prevent the system from ordering. The symmetry in question for a superconductor is the electromagnetic gauge field which is reflected in the phase of the superconducting order parameter such that the response to such perturbations is expected to be come strong in reduced dimensions and eventually suppress T_c completely.

Real 2D systems have a finite, albeit small, thickness and can undergo a quasi long range ordering, the Berezinsky-Kosterlitz-Thouless transition, and still superconduct. The question arises to what extent the increased susceptibility to fluctuations of the order parameter translates into an effective T_c reduction. To the best of our knowledge, first-principles calculations of phase and amplitude fluctuations have not been attempted so far. The calculation of T_c using the standard mean field Eliashberg equations while accurately treating the underlying electronic and phononic structure in a 2D geometry, however, indirectly also sheds light on the importance of fluctuation effects. The changes in the electronic and phononic structure can be important and in some cases are known to even increase T_c beyond the bulk value.

Here, we focus on a computational approach to the problem and, since the methods are by far more accurate, on electron-phonon driven superconductivity.

Phonon calculations are $\mathcal{O}(N_{\mathrm{atoms}})$ more expensive than electronic structure calculations and thus free standing slabs and interfaces are not easy to compute accurately. Otherwise the approach is similar to other 2D material calculations. Most electronic structure codes work in 3D, so for a surface geometry the amount of vacuum between two slabs must be sufficient to reduce spurious interactions. This is of particular importance when unsymmetrical slabs are used where one has to make sure no artificial dipole interaction between periodic replica obscures the result. The slab size has to be large enough that the local chemical environment of the interface is converged, which can easily lead to unit cells with several dozens of atoms. Possible dangling bonds can be saturated with specifically designed H-like atoms to speed up the convergence with slab size. In spite of these challenges, there have been a number of first-principles calculations of electron-phonon driven superconductivity of systems in a surface and free standing layer geometry.

2.9.1 Pb Monolayer on Si(111)

In an effort to study the approaching 2D limit of superconductivity by controlling the number of Pb layers on Si(111), Guo *et al.*[268] found an oscillating behavior of T_c as a function of number of layers. This is attributed to the effect of quantum confinement of the electronic

wavefunction, which creates oscillations in the density of states and the electron-phonon coupling with the vertical dimension. Yu *et al.*[269] have studied a system of 4 to 10 free standing layers of lead, also finding an oscillating behavior of the coupling constant and density of states. Note that while in bulk systems the effective screened Coulomb interaction μ^* is well approximated within the range $0.1 - 0.15$, the screening in a 2D geometry is more difficult to compute.[269] Özer *et al.* found a further reduction of T_c from 6.5 K at a thickness of 18 layers to 5 K upon decreasing the number of layers to 5 which excludes a final wetting layer.[270] This is also supported by DFT calculations,[269,271] even though the details of the interface with Si(111) are neglected in these studies. A single layer of Pb on a Si(111) substrate has been fabricated by Zhang *et al.*[272] and is superconducting with a $T_c = 1.86$ K for Pb in the striped incommensurate phase (SIC). Modeling the SIC phase by a $\sqrt{3} \times \sqrt{3}$ assembly, this T_c is well reproduced by a first-principles calculation by Noffsinger and Cohen.[273]

2.9.2 Graphene Related Compounds

There have been a number of first-principles investigations of electron-phonon super-conductivity in doped graphene.[274–277] The doping was achieved by including a Li coating in the calculations.[274,275] Using parameters for the Coulomb screening from well studied bulk graphene intercalated materials, Ref. 275 predicted a transition temperature of 8.1 K; the experimental $T_c = 5.9$ K[278] was later discovered to be in fairly good agreement with this result.

2.9.3 FeSe on $SrTiO_3$

FeSe is a very interesting material with a bulk T_c of 8 K.[279] The discovery of superconductivity in a FeSe monolayer on $SrTiO_3$[280] has caused enormous excitement in the community owed to the large T_c of 65 K in ARPES.[281] The hope is that understanding the origin of the greatly increased transition temperature could enable the construction of similar superconductors of even higher T_c and improved properties for technological applications. While bulk FeSe is generally considered a sign-changing $s_\pm$ superconductor driven by repulsive electronic interactions (see Ref. 282 for a review), measurements of the ARPES gap of FeSe on $SrTiO_3$ reveals a very isotropic s-wave gap.[281] Consequently, attractive interactions originating from

electron-phonon coupling were investigated in the material.[283] So-called replica bands in ARPES suggest a strong coupling of the modes at $q = 0$,[281] which has the particular feature that the electron-phonon coupling is supporting superconductivity in all pairing channels, including unconventional d and $s_{\pm}$ channels.

While FeSe appears to be only weakly bound to the substrate, an explanation for the strong electron-phonon coupling at small momentum involves the motion of the polar oxygen mode in $SrTiO_3$. The energy of this mode and the observed energy offset of the replica band are similar. First principles calculations have found this large coupling at $q = 0$[284] in agreement with the original model. That said, DFT calculations are not without problems. In many different types of DFT functionals, it is difficult to promote the charge transfer from $SrTiO_3$ to FeSe in a similar way as observed in experiment.[285–287] Moreover, and most importantly, the DFT bands at the Fermi level are in disagreement with experiment. This very interesting material is still not fully understood.

2.10   Responses to Stimuli

Certain properties in 2D materials are only accessible in the presence of external stimuli. This section focuses on the responses of 2D materials to mechanical and electrical stimuli, and how to understand these responses computationally. Methods to calculate relevant properties are discussed in their individual sections.

2.10.1   Mechanical Stimuli

Strain engineering and response in 2D materials has been heavily studied.[102, 288–296] Properly understanding 2D materials' behavior under mechanical stresses requires a slightly different treatment than bulk materials. Stress and strain along the z direction in monolayers is rarely considered, which reduces the dimensionality of the resulting property tensors. Thus, there are only three kinds of stress in 2D materials: normal stress in the x direction, normal stress in the y direction, and shear stress in the x-y plane.
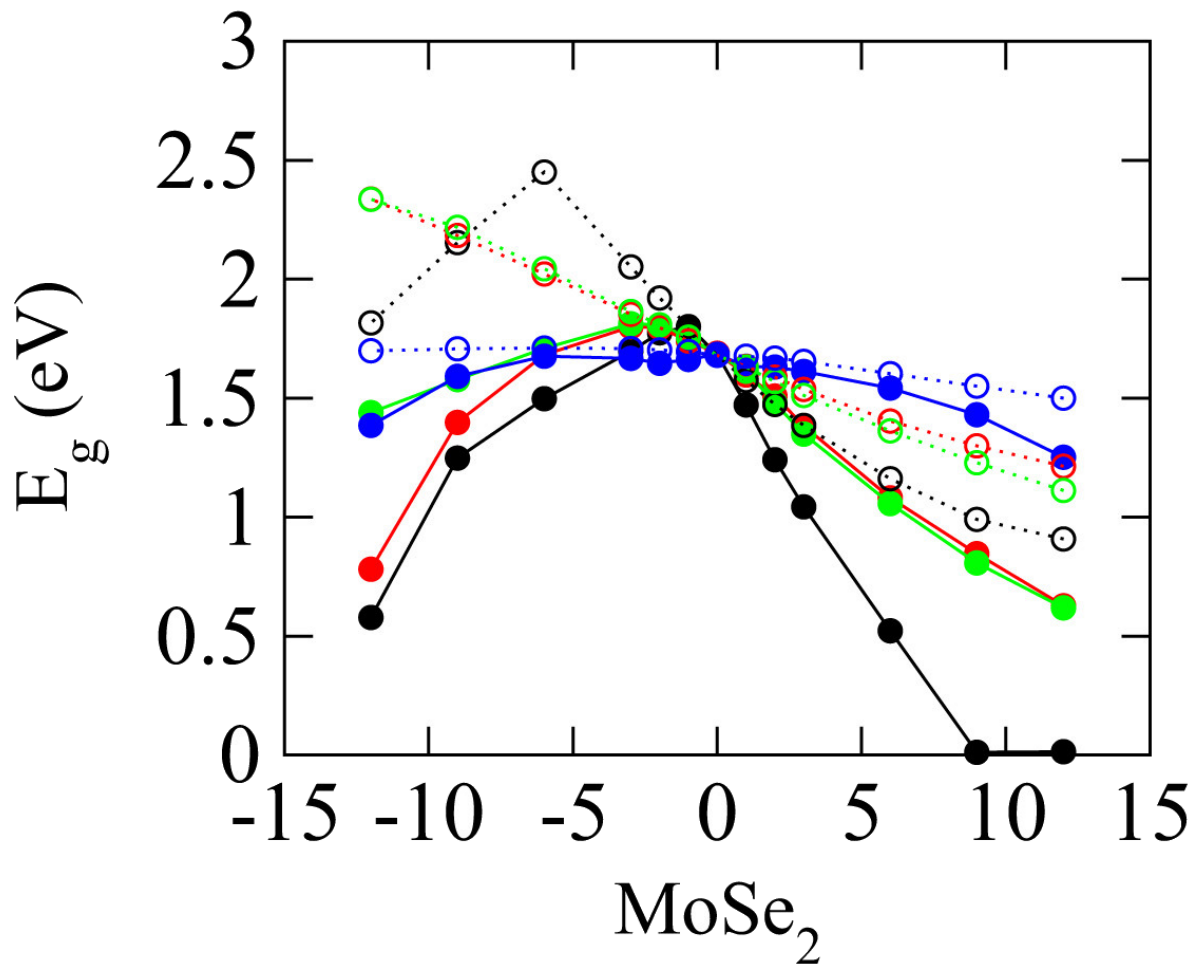
Figure 2-18. The change in band gap with applied strain of $MoSe_2$. Black represents isotropic strain, red and green represent uniaxial strain in perpendicular directions, and blue represents shear strain. Reprinted from [288]. Copyright 2016, with permission from Elsevier. https://doi.org/10.1016/j.ssc.2015.11.017

2.10.1.1 Band structure

Strain typically shifts the electronic bands in materials, most notably growing or shrinking band gaps. Graphene is well known for developing a band gap upon large enough applied strain,[289–291] and suffering a resulting decrease in conductivity.[292] Similarly, MX_2 (M=Mo, W, X =S, Se, Te) monolayers have been observed to undergo changes in conduction band minimum (CBm) and valence band maximum (VBM) locations under strain.[288, 293–295] This behavior is a result of the orbitals contributing to the band structure responding to the strain. Electronic bands do not always uniformly change with applied strain, nor is their response
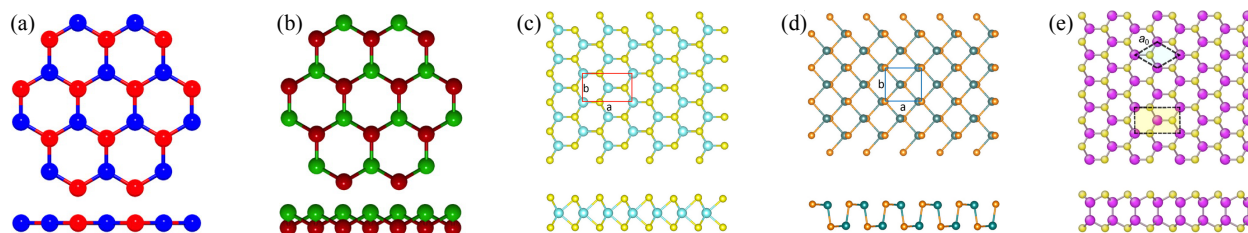
Figure 2-19. Known piezoelectric structures: (a) planar honeycomb structure of $h-$BN, (b) buckled honeycomb structure of III-V compounds, (c) $2H$ structure of transition metal dichalcogenides, (d) distorted rocksalt structure of group-IV chalcogenides, and (e) hexagonal structure of group-III monochalcogenides.[297] Image sources: (a) and (b) are reprinted from [8]. Copyright 2015 American Chemical Society. (c) and (d) are reprinted from [298], with permission of Springer. (e) is reprinted from [299], with permission of AIP Publishing.

necessarily isotropic with regard to the direction of applied strain. The response of the MoSe$_2$ band gap to strain is shown in Figure 2-18.

2.10.1.2 Elasticity

Elasticity is a material property that relates a mechanical stress to a strain response, and vice versa. Elastic constants can be estimated for 2D materials using a variety of computational methods. A common approach is to use the finite differences method,[300] which measures changes in stress due to small changes in applied strain on a unit cell. The relaxed ion elastic constants, which include ionic and electronic contributions, are then reported in a tensor.

All elastic constants for 2D materials have different units than those for 3D materials. Due to the reduced dimensionality, a force or displacement is applied along a unit of length rather than a unit of area. Elasticity or stiffness coefficients have units of N/m as a result. In VASP, 2D constants can be derived by normalizing the calculated 3D constants with the c lattice parameter. Elastic constants typically converge within at least 1% at a z spacing of 15 Å.[8]

Graphene is known for its high elastic coefficient of 350 N/m,[301] though 2D materials have a wide range of elastic constants. The elastic constants typically range between 30 and 300 N/m, and shear constants are between 10 and 70 N/m.[8] The elastic coefficient of h-BN

is also large at 297 N/m. 2D materials with low elastic coefficients include tetragonal PbO (34 N/m) and buckled hexagonal InSb (28 N/m).

2.10.1.3 Piezoelectricity

Piezoelectricity is a property that quantifies the interaction between mechanical stress or strain and electric fields generated by the material. The phenomenon only arises in materials without inversion symmetry, as applied strain causes species of differing electronegativity to distribute unevenly, resulting in the formation of a dipole and thus a net electric field across the material. There are five known classes of 2D materials that break inversion symmetry: planar and buckled hexagonal group III-V semiconductors,[7,8] $2H$ transition metal dichalcogenides,[48,49] group III monochalcogenides,[302] and group IV monochalcogenides.[303] These monolayers are shown in Figure 2-19.

Similar to elastic tensor coefficients, piezoelectric coefficients in 2D materials have different units due to reduced dimensionality. Polarization density P is reduced to C/m, and therefore the piezoelectricity tensor, $e = dP/d\epsilon$, has units of C/m. The piezoelectric tensor, $d = dP/d\sigma$, is normalized by the 2D elastic tensor and maintains its units of m/V. It can be calculated using density functional perturbation theory.[8,304–307]

An important distinction between piezoelectricity and elasticity is that electrical responses are not limited to the x-y plane for 2D materials.[8] This allows piezoelectric 2D materials to exhibit out-of-plane electrical responses due to in-plane stresses. Buckled hexagonal structures have been identified to exhibit an out-of-plane piezoelectric coefficient, which range from 0.05 - 0.5 pm/V.[8] It should be noted that all of the known buckled hexagonal structures are either unstable or metastable relative to other 2D phases.[34]

Piezoelectric coefficients, particularly those in buckled crystal structures, have been shown to converge more slowly than elastic constants. It is computationally expensive to calculate accurate coefficients using a large z spacing, but coefficients can be estimated by extrapolating to infinite z spacing. A recent study extrapolates in-plane coefficient e_{11} by fitting values to

the inverse of the layer spacing and out-of-plane coefficient e_{31} by fitting values to the square inverse of the layer spacing.[8]

In-plane 2D piezoelectric coefficients are usually in the range of 1-10 pm/V. The largest coefficients are typically in metal oxides such as CdO (21.7 pm/V) and ZnO (8.65 pm/V) and in metal dichalcogenides such as $CrTe_2$ (13.45 pm/V) and $CrSe_2$ (8.25 pm/V).[8] For more information on piezoelectric monolayers, we direct readers to a recent review of piezoelectric monolayers published by Zhang *et al.*[297]

2.10.1.4 Magnetostriction

Magnetostriction is a magnetic analog to piezoelectricity. Magnetostriction was first observed in single layer Fe_3GeTe_2, which exhibits a decreasing magnetic moment under compressive strain and an increased magnetic moment under tensile strain.[267] This was calculated using static calculations for applied biaxial strain ranging from -4% to 4%.

The degree of coupling is described by the magnetostrictive coefficient λ. This value depends on two components: the mangetoelastic energy density MAE, and the 2D elastic stiffness coefficient. For Fe_3GeTe_2, $\lambda =$ -559 ppm (parts per million), which is found to be larger than known bulk $Fe_{1-x}Ga_x$ alloys.[308] The details of this calculation for hexagonal crystals is outlined by Cullen.[309]

2.10.2 Electrical Stimuli

The properties of 2D materials also frequently respond to external electrical stimuli. Some of the most interesting and technologically important responses are discussed below.

2.10.2.1 Thermoelectrics

A recent topic of research in 2D materials is thermoelectricity. Thermoelectric devices directly generate a voltage from a temperature gradient and vice versa, which makes them useful in several applications. These include cooling, sensors, and thermal energy harvesting.

The origin of the thermoelectric effect lies in differences of the conductivity of high energy versus low energy electric carriers such that in the hotter side of the material, where carriers are excited to higher energies, the diffusion to the colder side overcompensates the back-flow

at lower energies. The most promising monolayer in the field at this time is black phosphorous due to its electronic and thermal anisotropy. One of the limiting factors in thermoelectric materials is that thermal and electrical conductivity often have positive correlation. In an ideal thermoelectric material, electrons will flow freely while a strong thermal gradient is preserved.

Black phosphorous not only has anisotropic electrical and thermal conductivities, but also preferred flow in orthogonal directions.[9] The electrical conductance has preferred transport along the armchair direction due to lower effective mass while the heat is transported along phonons which prefer the zigzag direction in black phosphorous. Through doping, black phosphorous becomes an extremely competitive material for use in thermoelectric devices. Its properties are illustrated in Figure 2-20.

In order to determine the directions of flow for electrical and thermal conductivity, the band structure and phonon spectra for black phosphorous was calculated and analyzed for, respectively, effective masses and speeds of sound. For more information on thermoelectricity in 2D materials, we direct readers to the review by Zhang *et al.* on thermoelectricity and its applications in 2D materials.[310]

2.10.2.2 Ferroelectrics

Ferroelectric 2D materials have been elusive, in part because they require a lack of inversion symmetry to generate a net dipole in the material. This net dipole must also be able to have its direction changed, and maintain the change in direction after the applied field is removed. Further, materials that behave as ferroelectrics in their bulk forms don't necessarily retain their ferroelectric properties when their thickness decreases to the nanoscale. Nevertheless, layered ferroelectrics are a natural starting point when looking for ferroelectric monolayers.

$CuInP_2S_6$ (CIPS) is a layered ferroelectric material that is found to retain its ferroelectric behavior when decreased to a thickness of two monolayers.[311] When the polarization of the CIPS structure was calculated using DFT, it was found that the material remained ferrielectric
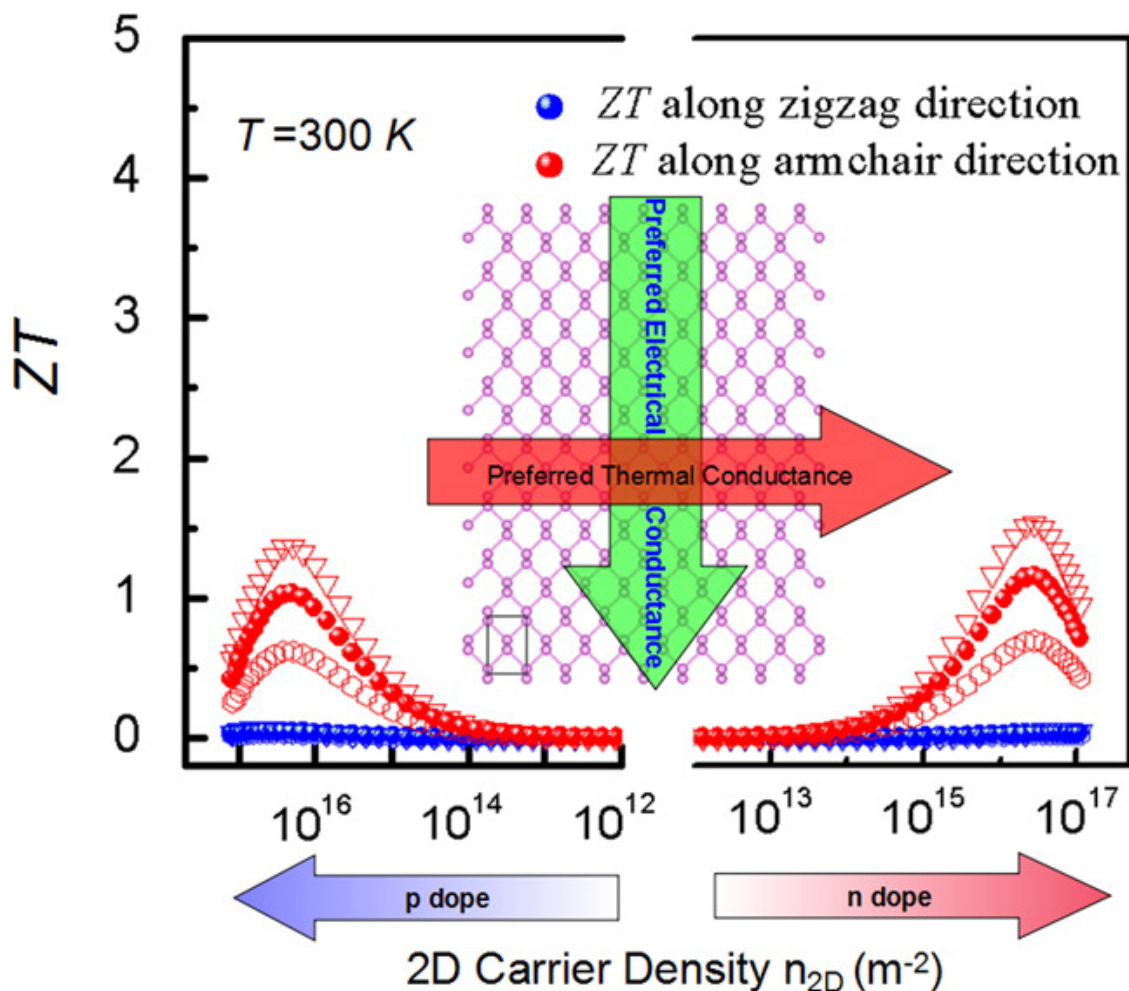
Figure 2-20. The thermoelectric behavior of black phosphorous, doped with carrier doping of approximately $2 \times 10^{1}6$ m^{-2}. The ZT, or measure of effectiveness as a thermoelectric, is found to increase with doping along the armchair direction while remaining low along the zigzag direction. This is a result of the anisotropic electrical and thermal conductivities in monolayer phosphorous. The open circles, closed circles, and inverted triangles represent phonon relaxation times of 150, 60, and 45 ps respectively. Reprinted with permission from [9] Copyright 2014 American Chemical Society.

as a bilayer. Although the mechanism that gives rise to its ferrielectricity is slightly different than that of conventional ferroelectricity, the response behavior for both is the same.

A monolayer that displays ferroelectric behavior in its most stable configuration was recently discovered computationally in the MXene Sc_2CO_2. This material displays both an in-plane and out-of-plane polarization, and was found to have an intermediate antiferroelectric phase, allowing for the transition from one out-of-plane polarization to the other. Group IV chalcogenides have also recently been found to be multiferroic, displaying both ferroelectric and ferroelastic behavior.[312]

Determining ferroelectric behavior computationally requires three steps: identifying a net polarization in the monolayer, identifying stable ferroelectric and antiferroelectric phases of the monolayer, and calculating the energetic barriers between the the phases. The first and second step can be found using standard DFT and Berry phase calculations. Determining the energetic barriers is best done with density functional perturbation theory. In addition, one must ensure that there is not a point during the transition when the material becomes metallic, or else the polarization is not guaranteed to reverse.

2.11 Defects

Like in bulk materials, defects in 2D materials can have a significant impact on their properties. In the next sections, we discuss the structure of defects and their effects on the properties of 2D materials. We classify the defects by their dimensionality into zero-dimensional point defects, one-dimensional line defects such as dislocations, grain boundaries, and edges, and two-dimensional area defects. For a discussion of experimental aspects of defects in 2D materials, we refer the reader to reviews on defects in 2D MoS_2,[313] graphene,[314–316] and defect engineering in 2D materials.[317]

2.11.1 Point Defects

The same kind of point defects are possible in 2D and 3D systems: vacancies, interstitials, and substitutions or impurities. Naturally, these defects can also interact to form pairs or complexes. Because of the reduced dimensionality in 2D systems, point defects can

dramatically affect the electronic conductivity, optical spectra, magnetic response, and other properties even at modest concentrations.[313–317]

The most important quantity for point defects is their formation energy.[318,319] The formation energy, $E_{\mathrm{def}}^{\mathrm{f}}$ for a defect, X, with charge q is given by

$$
\begin{aligned}
E_{\mathrm{def}}^{\mathrm{f}}[X^q] \;=\; & E_{\mathrm{tot}}[X^q] - E_{\mathrm{tot}}[\mathrm{bulk}] \\
& - \sum n_i \mu_i + q[\epsilon_{\mathrm{F}} + \epsilon_{\mathrm{v}}],
\end{aligned}
\tag{2-5}
$$

where $E_{\mathrm{tot}}[X^q]$ and $E_{\mathrm{tot}}[\mathrm{bulk}]$ are the total energies of the supercell containing the defect and perfect bulk structure, respectively, n_i and μ_i are the number and chemical potential, respectively, of the atomic species, i, comprising the defect. ϵ_{F} is the Fermi level with respect to the valence band maximum (VBM) and ϵ_{v} is the energy of the VBM of the pristine host. The formation energy of point defects determines their equilibrium concentration. Furthermore, equilibration of defects can be slow at ambient conditions. Hence, the defect concentration in 2D materials is a often controlled by synthesis conditions such as the local chemical potential of components and the Fermi level, *e.g.*, set by the substrates.

Calculations of point defects require large simulation cells to approach the low concentration relevant for experiments and to reduce the spurious interactions between the defect and its periodic images.[320] Convergence of the defect formation energy with simulation cell size works well for neutral defects, but special care has to be taken for charged defects.

Most DFT calculations employ plane-wave basis sets and periodic boundary conditions. To minimize the interactions between periodic images of the 2D materials in the direction perpendicular to the material, increasing amounts of vacuum spacing are added until the energy or other properties converge. For charged defects, the Poisson solver of plane-wave DFT codes implicitly assumes a compensating background charge and an average electrostatic potential of zero. However, unlike for bulk materials, 2D materials containing a net charge due to a charged defect display a linear divergence of the energy with vacuum spacing that is not corrected by a compensating uniform charge background. Furthermore, the electrostatic

potential becomes quadratic in the vacuum region instead of linear, as would be the case for an isolated charged 2D material. As a consequence, the energy and forces are incorrect.

To correct this erroneous behavior requires either the addition of an energy correction, the modification of the compensating charge, or the truncation of the Coulomb interaction in the direction perpendicular to the 2D materials. Several energy correction schemes have been proposed, including corrections of the Madelung energy[321, 322] and the electrostatic potential.[323] Richter *et al.* suggest a compensating charge that modifying the nuclear charge of one of the species in the charged material.[324] Alternative techniques that remove the spurious Coulomb interaction between periodic images of the 2D materials include Hockney's Fourier approximation to the Coulomb interaction[325] and improved reciprocal space method by Martyna and Tuckerman,[326] which, however, require large simulation cells. More recently, Genovese *et al.* developed an interpolating functions method that truncates the Coulomb interaction between periodic images of lower dimensional materials.[327]

These computational methods provide potential solutions to the divergence issue for charged defects in 2D materials. However, the lack of implementation in widely available DFT codes still limits the number of calculations for charged defects in 2D materials. Furthermore, comparisons between the computational approaches and experimental validation are needed to determine the accuracy and efficiency of the various approaches for charged defects.

2.11.2 Line Defects

Line defects in 2D materials are slightly different than in bulk materials. In 3D structures, a line defect and grain boundary are distinctly different, with the former being considered one-dimensional and the latter being two-dimensional. In 2D materials, line defects are equivalent to grain boundaries. There is no second direction for the structural defect to expand periodically, but these defects still define distinct grains within 2D materials. Thus, line defects and grain boundaries are treated as equivalent in the remainder of this review. We break the discussion into two sections: we first consider the structure of line defects, then discuss the properties that arise due to line defects.
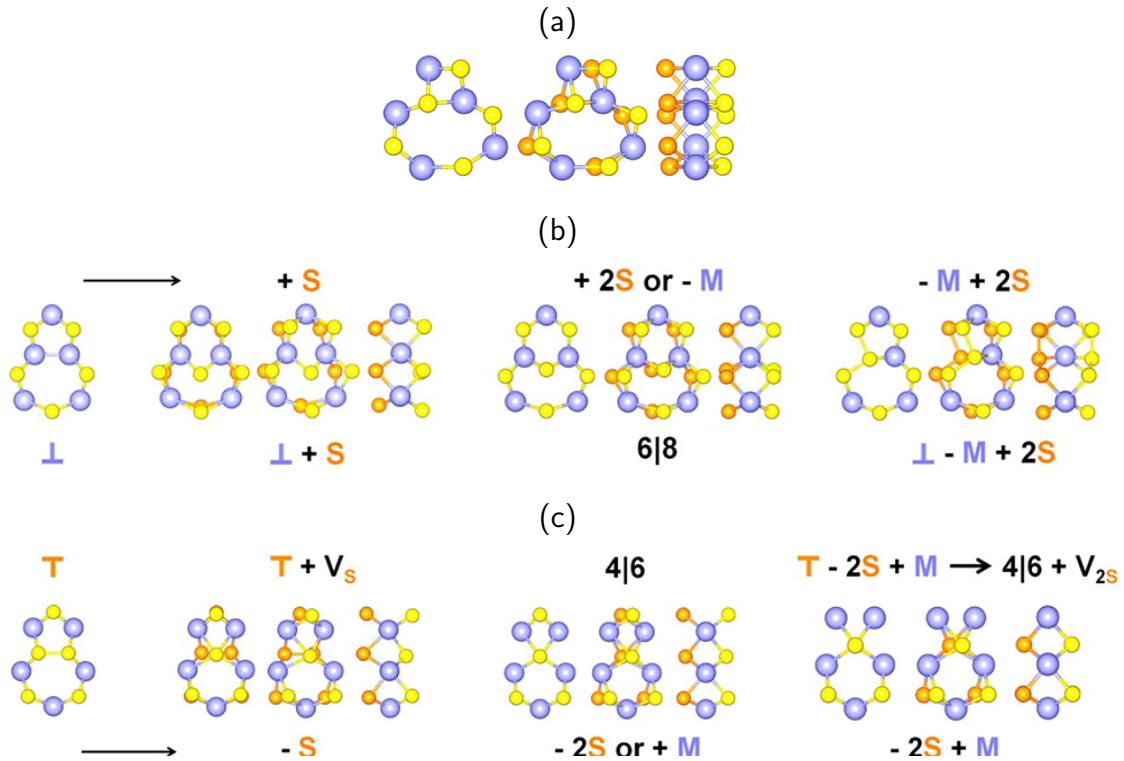
Figure 2-21. Dislocations in monolayer MoS_2. Each dislocation is shown from three perspectives: the top, slightly tilted, and side view of the monolayer (ordered from left to right). Dislocation (a) is referred to as 4|8. Dislocations (b) and (c) begin as 5|7 dislocations, then transition into different dislocations as atoms are added or removed. Adapted with permission from [328]. Copyright 2013 American Chemical Society.

2.11.2.1 Structure of line defects

In the following, we discuss the structure of line defects in hexagonal planar and $2H$ structure monolayers. They are both hexagonal structures, and the dislocations are typically identified by the number of atoms that form a ring in the structure. For example, 4|8 is the notation used to denote a dislocation comprised of one 4–atom ring and one 8–atom ring when viewed top down (see Fig. 2-21 (a)). A single dislocation does not constitute a line defect, but can be placed in series to construct a line defect. Thus, although dislocations are not themselves line defects in 2D materials, they are intrinsically linked to the discussion. To further clarify, line defects can either be continuous, *ie* able to continue indefinitely, or discontinuous with an eventual termination.

The hexagonal planar structure allows for several dislocations. These are primarily in the form of 5|7 and 5|5|8 defects in graphene,[329] though 5|9 dislocations have also been seen.[330] Grain boundaries composed of 4|8 dislocations have also been found to be stable in other planar hexagonal structures.[331] The dislocations that compose a grain boundary do not necessarily have to be periodic, as the boundary can be composed of a variety of dislocation types.[332]

The $2H$ structure exists in AB_2 monolayers, the most common example being MoS_2 and other transition metal dichalcogenides. Zou et $al.$ predicted which dislocations can occur in MoS_2 and WS_2, and which can result in continuous line defects.[328] Of the dislocations predicted, a total of 3 retain stoichiometry in isolation: 4|8, and two forms of 5|7 (one with bridging metal atoms, one with bridging S atoms). S-rich defects include 6|8 and 5|7. Metal-rich include 4|6 and a 4|6 dislocation combined with two sulfur vacancies. These structures can be found in Figure 2-21. In addition, bridging sulfur (8|8) and bridging molybdenum (5|5|8) dislocations have been computationally predicted to be stable and present in experimental MoS_2.[333] 4|8, metal bridging 5|7 and S-rich 6|8 dislocations have also been verified experimentally.[208,334] Finally, Zhou et $al.$ verified the existence of two 4|4 dislocations: one where two rings share a single sulfur atom at a point (4|4P) and the other where two rings share an edge of sulfur atoms (4|4E).[208]

2.11.2.2   Properties of line defects

Self-doping is a prevalent phenomenon in graphene. The break in symmetry caused by line defects creates electronic states that act as n-type dopants.[76] This has been seen in extended 5|8|5 line defects, which also display ferromagnetic behavior.[336,337] Other line defects composed of multiple dislocations have also been found to be magnetic.[338]

In AB_2 (A=Mo, W; B= S, Se) monolayers, it is seen that 5|7 and 4|8 defects display magnetic behavior.[335] Both Mo- and S-rich 5|7 defects display ferromagnetic behavior (as seen in Fig. 2-22) while 4|8 defects are most stable when displaying antiferromagnetic order along the defect length. With regard to electronic structure, 4|4P defects have been predicted to act
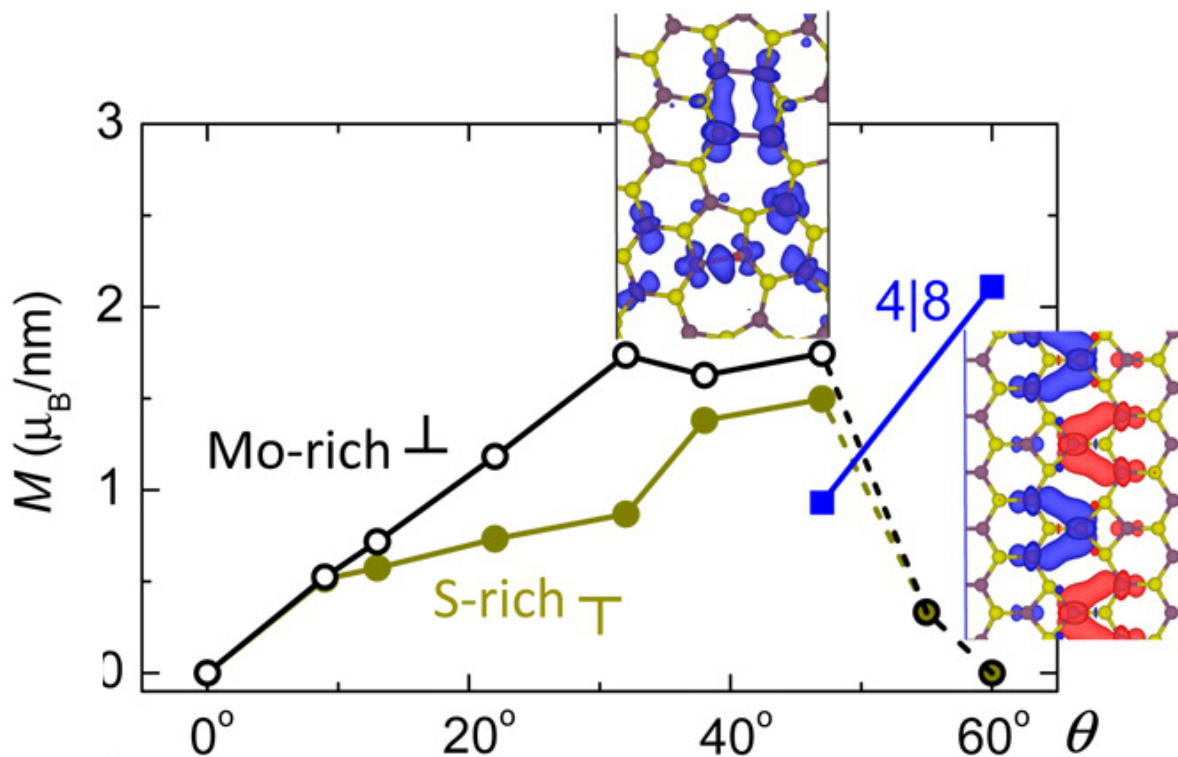
Figure 2-22. The amount of magnetization for the 5|7 and 4|8 defect loops in MoS_2, with regard to misorientation angle. All defects are assumed ferromagnetic in these calculations. One can see that Mo-rich defects are more magnetic than S-rich. Note that the 4|8 defect is found to display antiferromagnetic behavior in its most stable state. Reprinted with permission from [335]. Copyright 2013 American Chemical Society.

as a metallic strip in MoS_2[208] while states within the band gap have been shown to arise in 4|8 defect loops.[334]

2.11.3   Monolayer Edges

Though monolayers are often modeled as if they continued indefinitely in two directions, experimental monolayers have edges. These edges have properties which are quite different from the "bulk" of the monolayer, and have been investigated heavily as a route to tailor properties. In hexagonal and $2H$ structure monolayers, there are two basic edge terminations: zig-zag (ZZ) and armchair (AC), as seen in Figure 2-23. For each of these edges, there can be varying atomic occupations for 2D materials with several layers of atoms (*e.g.* Mo-rich, S-rich). Edges are normally modeled in DFT calculations by creating a sufficiently wide nanoribbon.
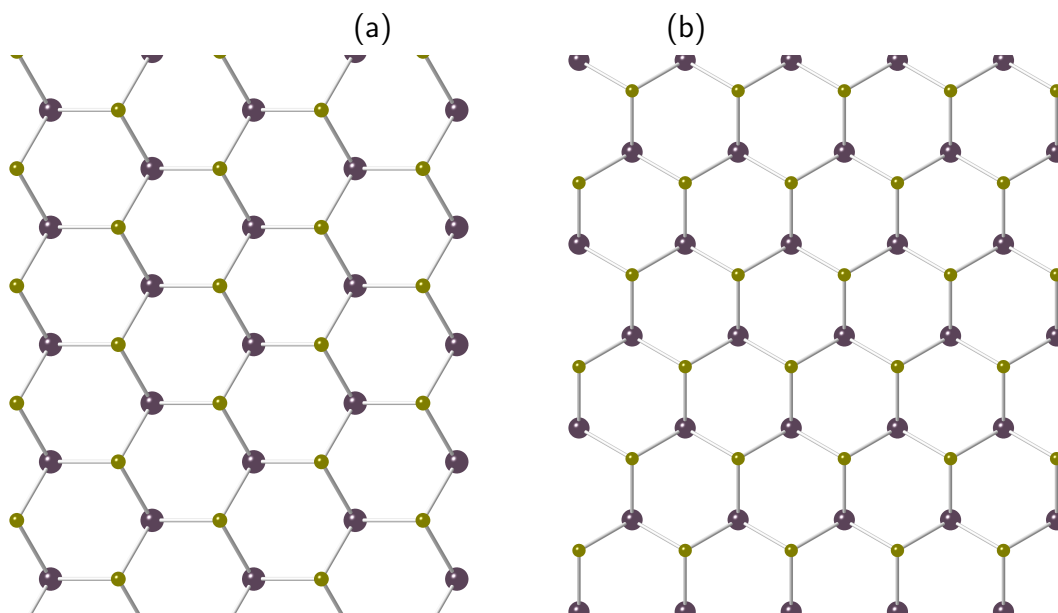
Figure 2-23. The two most common edge shapes of hexagonal and $2H$ monolayers. The (a) and (b) nanoribbons represent zigzag and armchair terminations, respectively.

Graphene displays magnetic moments in ZZ edges[339–341] but not AC edges.[342–344] The emergence of magnetism is due to the appearance of non-bonding π and π^* bands at the Fermi level, which significantly increases the density of states at the Fermi level.[340, 342, 345] The impact of these edge states on the bulk properties is found to decrease dramatically with ribbon thickness, indicating that this behavior is truly restricted to the ZZ edges.[342, 343] A break of symmetry that results in self doping is also present in the edges of graphene.[76]

MoS$_2$ has been investigated to determine the shape of the unit cell under varying synthesis conditions. Using Wulff construction rules, Cao *et al.* found that a Mo-rich environment results in a dodecagonal shape, S-rich in a triangular shape, and in between it takes varying hexagonal shapes.[346] The edges present are AC and three ZZ (S$_2$-rich, S-rich, Mo-rich), the latter two display magnetic behavior. The dodecagon shape displays a significant amount of magnetism, but as the number of sides decreases (the synthesis environment becomes more S-rich) the magnetism disappears. In regard to electronic properties, the AC edge remains semiconducting while the ZZ edges exhibit metallic behavior. Reconstructions have also been

observed in MoS_2. Though the reconstructions are found to be thermodynamically unstable, the lack of thermodynamic equilibrium during synthesis is thought to allow their existence.[208]

2.11.4 Area Defects

Area defects in 2D materials are primarily identified as Haeckelites. Haeckelites are extended regions of the dislocations discussed in Sec. 2.11.2.1. These have been predicted computationally in 5|7 rings of graphene[347,348] and in 4|8 rings of several TMDCs.[349] However, the authors of this review are not aware of these extended area defects appearing in the experimental literature.

2.12 Synthesis

2.12.1 Monolayer Synthesis

Although the primary focus of this article is computation, it is important to know how 2D materials are synthesized. This section describes the available synthesis methods for 2D materials.

Broadly, there are three ways to obtain 2D materials: exfoliation, chemical vapor deposition (CVD), and etching. Exfoliation was the method used to synthesize graphene by Novoselov and Geim.[43] This method is suitable for synthesizing samples in a laboratory setting but difficult to extend to larger scales. CVD vaporizes species using heat and/or pressure, and releases them into a chamber with a cooled substrate. The vaporized species then deposit on the substrate, resulting in the self-assembly of a film. The crystallography of the film depends on the species in the air and on the substrate used. Finally, etching is used on materials such as the MAX phases, where sacrificial layers are removed by a solvent and monolayers are left suspended in solution.

2.12.2 Heterostructures

When building devices composed of monolayers, one can combine monolayers in a vertical or lateral heterostructure. The former is where the majority of research has been focused (and is discussed further in the next section), while lateral heterostructures are more difficult to synthesize. However, it is an area of significant ongoing research interest.[350–352]

Reviews specifically discussing monolayer heterostructures are available.[353] Both kinds of heterostructures are typically created by growing one monolayer at a time on a host substrate.

Lattice mismatch presents a challenge to the formation of both kinds of heterostructures. The importance of mismatch is somewhat lower for vertical heterostructures, as vdW bonding allows for a certain degree of incommensurability. Still, the alignment of the monolayers relative to each other can impact properties like conductivity if there are defects creating interfacial trap states. Lateral heterostructures are strained as a result of the strong covalent bonding at the junction boundary. In either case, mismatch can perturb or destroy the desired properties of the heterostructure. Charge transfer can also take place between the monolayers in a heterostructure and this can also cause otherwise unexpected behavior.[354,355]

2.13   Device Simulation

Monolayer MoS_2 has attracted extensive research interest recently for its potential applications in nano-electronics,[356] flexible electronics,[357] and optoelectronics.[358] TMDC field-effect transistors (FETs) represent the ultimate thickness limit and exhibit superior immunity to short channel effects.[5,6] The absence of thickness variation, surface roughness, and dangling bonds in these thin monolayer materials results in excellent intrinsic carrier transport properties and transistor scalability.

Furthermore, the mono- and few-layer TMDC materials are mechanically flexible and bendable. Thus, the materials and their heterojunctions have led to the development of numerous flexible electronic device designs.[86] Specific examples include low-power electronics for the switching circuitry of flexible displays and vertical steep sub-threshold device based electronics.[359–362]

2.13.1   Approaches to Device Simulation

Carrier transport in semiconductor devices is traditionally modeled using semi-classical methods, such as the drift-diffusion theory for long channel silicon metal-oxide-semconductor field-effect transistors (MOSFETs). For nanoelectronic devices, quantum effects and atomistic-scale features inevitably become important. In response to this need, recent research

has led to the evolution of a unified and powerful quantum transport simulation framework based on the non-equilibrium Green's function (NEGF) formalism.[363–365]

It has been shown that the tunneling current is negligible in a device with 20 nm gate length, while direct source to drain tunneling is much more significant in a device with a gate length of 5 nm.[366] Hence, both the semi-classical and NEGF-based simulations have been applied to simulate 2D semiconductor devices. We focus on development and application of simulation approach and models to 2D devices. The studies on 2D semiconductor devices have been extensive and are beyond the scope of this review.

2.13.1.1 Semiclassical approach

Several semi-classical-based compact models of graphene, graphene nanoribbon and bilayer graphene devices have been presented for digital and radio frequency applications and circuit design purpose.[367–372] Meanwhile, models based on a semi-classical approach for monolayer TMDC material and black phosphorous (BP) MOSFET have been developed for computational efficiency. A top-of-barrier model was used to study the performance limit of monolayer TMDC and BP based MOSFET.[373,374] It showed that the device performance of monolayer TMDC and BP transistors outperform ultra-body-Si transistors with high-κ gate insulators, although the influence of scattering and contact resistance was not considered.

A drift-diffusion model was presented to study the I-V characteristics of a single TMDC long channel FET based on a lumped capacitance network.[375] An analytical model was used to study the subthreshold performance of a monolayer MoS_2 MOSFET.[376] The model consisted of three different subthreshold current sources, 1) subthreshold current, 2) band-to-band tunneling and 3) Shockley-Reed-Hall generation from the drain to body. A more rigorous model including all regions of MOSFET operation was derived for a 2D TMDC based MOSFET.[377] The model is also based on drift-diffusion theory but it also includes extrinsic effects such as interface traps, mobility degradation and inefficient source/drain doping. To facilitate circuit simulations, drift-diffusion-based compact models of lateral TMDC transistors have also been developed.[378–380]

2.13.1.2 Quantum transport approach

As the channel length scales down to sub-20 nm range, quantum tunneling and quasi-ballistic transport effects can play a more important role in carrier transport. The non-equilibrium Green's function (NEGF) formalism,[363–365] which describes quantum effects, can be used to simulate quantum transport in nanodevices. Device performance of graphene and graphene nanoribbon-based nanoscale MOSFET and tunneling FET has been thoroughly studied using the NEGF formalism.[381–389] In addition, ballistic NEGF transport simulations have been applied to study 2D TMDC and black phosphorous transistors with a channel length down to the sub-20 nm regime.[390–400] The effect of scattering can be treated in the NEGF formalism by using the self-consistent Born approximation.

Liu et al. have shown that considering phonon scattering is important to accurately predict the performance of MoS_2 FETs.[366] They predict that an 8.1 nm long monolayer MoS_2 MOSFET can fulfill the ITRS requirements for high performance logic devices in 2023. Phonon scattering effects on monolayer WSe_2 n-type MOSFET and BP FET have also been investigated.[401–403] By using a double gate structure, it has been predicted that a bilayer MoS_2 FET can fulfill the requirement of HP devices up to a 6.6 nm gate length.[403]

The effects of a doped contact and a metal contact on the performance of monolayer MoS_2 FET have been investigated by Han.[400] An Ohmic contact between semiconducting $2H$ MoS_2 and metallic $1T$' MoS_2 has been demonstrated in a MoS_2 FET with a gate length of 7.5 nm.[404] Quantum transport simulations have been carried out and shown good subthreshold swing. Recently, a MoS_2 transistor with 1 nm gate length has demonstrated with subthreshold swing near the thermionic limit.[405] The performance of a MoS_2 FET with sub-5nm gate length has also been studied.[406] The high frequency performance limit of a monolayer BP FET with a gate length of 10 nm has also been investigated.[407] In addition, the NEGF approach has been applied to study the performance of TMDC and BP tunneling FETs.[397, 408–415]

2.13.2 *In Silico* **Device Fabrication**

Simulation cells for vertical heterostructures can be formed automatically using the MPInterfaces software package.[42] Based on the work of Zur and McGill,[416] MPInterfaces will match two monolayers of arbitrary orientation in a single unit cell by minimizing both the cell size and the strain imposed on each layer. To the authors' knowledge, there are currently no open source tools available for the automatic construction of lateral heterostructures.

2.14 Outlook

Computational high-throughput methods have greatly accelerated the 2D materials discovery process as well as improved the in-depth understanding of their physical and chemical properties. Developing robust 2D databases will be crucial to expediting the spread of knowledge in the community. The application of advanced statistical analysis to these datasets remains an exciting and open frontier for discovering trends and physical rules for 2D materials.

Chemical substitutions are a simple way to expand the currently available 2D databases, and genetic algorithms can also be expected to contribute new stable 2D structures to these databases in the coming years. Developing machine learning models that interface to these methods would be one way to reduce the number of required objective function evaluations (typically DFT calculations) and decrease the amount of time required to perform a thorough search.

As a result of their exciting potential, graphene and TMDCs have received the majority of focus in the areas of gaseous interactions and defect properties. However, we have listed many other classes of 2D materials that possess great potential for devices as well. High throughput tools to investigate the behavior of these monolayers when interacting with gases and exhibiting defects will streamline and improve these fields of research. In addition, the edge shapes of hexagonal and $2H$ monolayers are well-documented. New 2D structures, however, often do not exhibit the established "zigzag" and "armchair" terminations. Future work is expected regarding the edge terminations of these more exotic monolayer structures.

With growing computing power and improved theoretical methods, first-principles cal-culations of larger systems are becoming possible. This opens possibilities for discovering, *e.g.*, new superconducting 2D materials and describing surfaces and interfaces more accu-rately. Modern experimental techniques, such as field effect doping, allow for modifying the electronic structure of covalently bonded thick layers, leading to rich prospects for new high T_c superconductors. Recent works show that first-principles electron-phonon calculations lead to meaningful results even in these often exotic electronic environments and can thus be an important tool to guide experimental understanding and fuel the discovery of novel superconductors.

2D materials hold promise for several applications. The recent the discovery of monolayer half-metals and magnetic insulators have expanded the potential of ultra-thin spintronic devices. There has also been significant growth in the field of 2D materials that respond to stimuli, which could be used in a variety of devices. For many of these monolayers, whether they maintain their properties when assembled in heterostructures remains an open question. Much recent effort has focused on investigating the suitability of 2D materials to act as photocatalysts for hydrogen evolution, and this remains a particularly promising proposed application. There has been some research on carbon evolution, but overcoming the difficulties associated with the process is ongoing. Other potential redox reactions have yet to be investigated in as much detail, but they may enable routes to convert harmful liquids or gases into benign or useful byproducts.

The next several years of 2D materials research, supported by the onset of accessible 2D material databases, will undoubtedly produce many exciting results, and may see the emergence of 2D materials in commercial technologies.

CHAPTER 3
STABILITY AND MAGNETIC BEHAVIOR OF EXFOLIABLE EXTREME NANOWIRE 1D MATERIALS

This chapter is an application of the topological scaling algorithm.[22] This algorithm determines the periodicity of a crystal by developing a network of bonded atoms, generating a supercell of the crystal, and rebuilding a network from the same starting point. Then, depending on the ratio of the initial and final network, the periodicity of the crystal is determined. This algorithm had previously been applied to the MaterialsProject database in search of graphite-like structures for exfoliable 2D materials. In this effort, I apply it again to the MaterialsProject database in search of van der Waals bonded nanowires. In doing so, I analyze the sensitivity of this algorithm to the criteria for network formation and discuss unique crystals found, such as dimensional heterostructures and bipartite crystals. I continue with a discussion of the thermodynamic stability of nanowires, using single chain Te as a metric. More specifically, 3H-Te, as this has been experimentally synthesized and can be exfoliated from a bulk precursor near the thermodynamic hull. Included is discussion of the difficulties of optimizing the structure of these nanowires using DFT and the potential impact of Peierls distortions on stability. Analysis of these electronic and magnetic properties of these nanowires follow, with an exploration of how magnetic ordering impacts stability of five magnetic nanowires.

3.1 Background

Nanomaterials are of great scientific interest due to their unique electronic, optical, magnetic, and quantum properties.[1–3, 10, 13, 48, 49, 417, 418] These properties enable a variety of potential applications, including optoelectronic,[49, 350] spintronic,[419, 420] and quantum devices.[421, 422] The emergence of these properties, when transitioning from bulk precursor to low-dimensional materials, stems from the enhancement of quantum mechanical effects, e.g., quantum confinement.

Nanomaterials range from zero-dimensional (0D) clusters and nanocrystals to one-dimensional (1D) nanotubes, wires, and ribbons to two-dimensional (2D) nanolayers. 0D
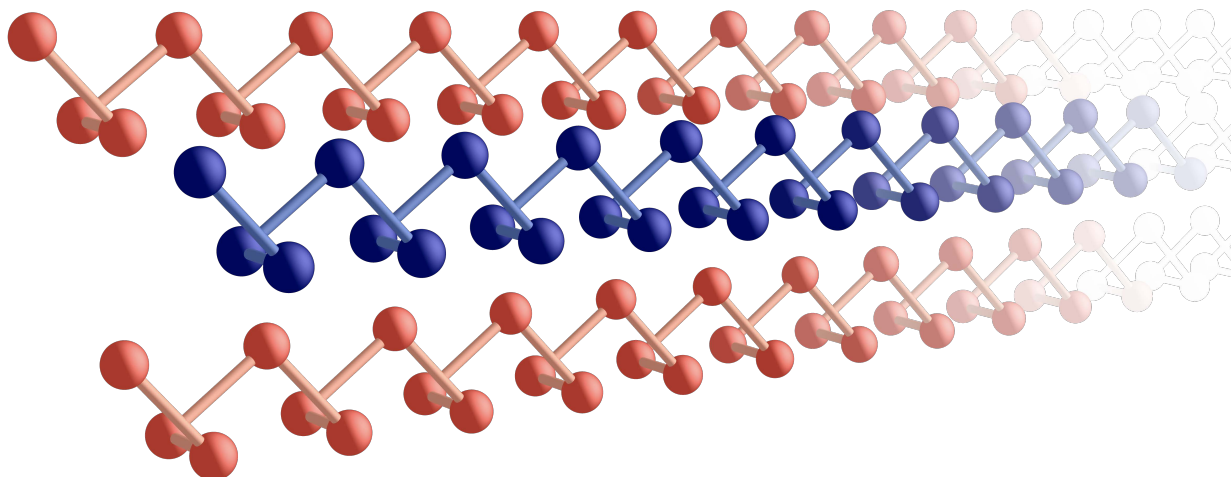
Figure 3-1. The structure of bulk tellurium with a 3-atom unit cell consists of 1D structural motifs, highlighted with the single chain of blue atoms. Exfoliation of such a material can lead to a 1D material, which corresponds to an inorganic polymer or nanowire. This Te nanowire forms a 3-fold-symmetric helical coil, denoted as 3H-Te.

materials have been a topic of research for several decades due to the tunability of their properties with system size.[417] Nanocrystals have numerous applications, such as semiconducting quantum dots for lighting, displays, and photovoltaics,[10–12] metal oxide and chalcogenide nanocrystals for catalysis,[423–425] fluorescent semiconductor nanocrystals for medical imaging,[426] and functionalized silica nanoparticles for disease treatment.[427] 1D materials have received less attention than other nanomaterials,[428] with the main focus for this class of materials on nanotubes[429] and nanoribbons,[430] both of which are synthesizable from 2D materials. However, several investigations have synthesized so-called extreme nanowires of a few Angstrom to nanometer radius by encapsulating them within carbon nanotubes.[13–17,431] 2D materials became of great interest with the discovery of graphene with its unique electronic and mechanical properties.[1] Since then, a large number of two-dimensional (2D) materials have been predicted and discovered, such as h-BN,[3,47] transition metal di-chalcogenides,[2,48,190,432] MXenes,[53,433] metal oxides,[84,434] and phosphorene,[85,435] with several reviews of the experimental[73,75,78] and computational efforts.[4,21,436]

Methods for the discovery of novel nanomaterials fall into two categories: approaches that rely on known crystal structures and approaches agnostic to prior crystal structure knowledge. Methods in the former category include datamining crystal structure databases[22, 28–30] and chemical substitutions in known prototype nanostructures.[33, 34, 190, 437] These methods have successfully predicted 2D materials that were subsequently synthesized experimentally.[418, 437–443] Techniques agnostic to known crystal structures include genetic algorithm and particle swarm structure searches,[23, 107, 184, 185] which use some objective function for evaluating the fitness of the generated crystals and the creation of new structures. Most of these discovery efforts for nanomaterials focus on 2D nanosheets, with only a few studies that identify 1D structural motifs in bulk materials.[30, 444]

In this paper, we identify exfoliable 1D materials that fall under the category of "extreme nanowires" and characterize their stability, electronic behavior, and magnetic properties. We use the topological scaling algorithm (TSA)[22, 42] to search the Materials Project database[37] and classify the dimensionality of the structural motifs comprising each bulk material. We identify 3,414 bulk materials composed of van der Waals bonded chains, i.e., pseudo-1D solids. Figure 3-1 illustrates, as an example, the 1D structural motif of tellurium (Te). We isolate these 1D materials and calculate their thermodynamic stability, using single chain Te as the reference due to its successful synthesis as a nanofilm[445] and inside carbon nanotubes.[13] We proceed to investigate the electronic and magnetic properties of the 295 nanowires that contain transition metals. We show that 1D materials exhibit a wide range of electronic and magnetic properties, revealing potential pathways to electronic applications and the value of investigating this relatively unexplored class of materials.

3.2   Methods

We apply the topological scaling algorithm (TSA) developed by Ashton *et al.*[22] and implemented in the MPInterfaces software package[42] to identify the dimensionality of the structural motifs comprising the materials in the Materials Project database as of the 15 of August, 2019.[37] We use the empirical atomic radii[446] specified in the pymatgen software

package[41] when using the TSA. To create the isolated 1D structures, perform the density functional theory (DFT) calculations, and analyze the results, we employ the MPInterfaces[42] and pymatgen[41] software packages. We identify and remove duplicate 1D materials by comparing the interatomic distances of systems with identical compositions.

The DFT calculations of the stability and properties of the 1D materials are performed with the plane-wave code VASP[447] using the projector-augmented wave (PAW) method.[448] To account for dispersion interactions between the 1D structural motifs in the bulk structure, we employ the vdw-DF-optB88 approximation[449] for the exchange-correlation functional. A plane-wave cutoff energy of 600 eV and a Γ-centered k-point mesh with a density of 60 k-points/Å^{-1} along the periodic directions ensures convergence of the energy of the relaxed structures to better than 1 meV/atom. All calculations are performed spin-polarized and initialized ferromagnetically unless otherwise stated. To improve the reliability of the structural optimization, we employ a damped molecular dynamic algorithm with a damping factor μ ranging between 0.2 and 0.4 and a small timestep of 0.05 to 0.3 fs. We place all 1D materials in an orthorhombic simulation cell such that their periodic direction is parallel to the a axis. To determine the vacuum spacing required to converge the nanowires' energy to 1 meV/atom, we calculate the change in energy when increasing the vacuum spacing from 10 to 26 Åfor 30 randomly selected 1D materials. The dispersion interaction between two parallel metallic wires scales with distance, d, as $1/\text{d}^2$.[450] Using this scaling relation, we find that the energy is converged to well below 1 meV/atom for a vacuum spacing of 20 Å, which we apply to the non-periodic directions of the nanowire cells.

3.3   Results

3.3.1   Identification of Structural Motifs

We apply the TSA to identify the structural motifs of all materials contained in the Materials Project database[37] as of August 23, 2019. The creation of the bonding network in the TSA requires a choice of bond lengths. Since there is no universal choice of bond length across all materials, we use the sum of the empirical atomic radii[446] of the species as specified
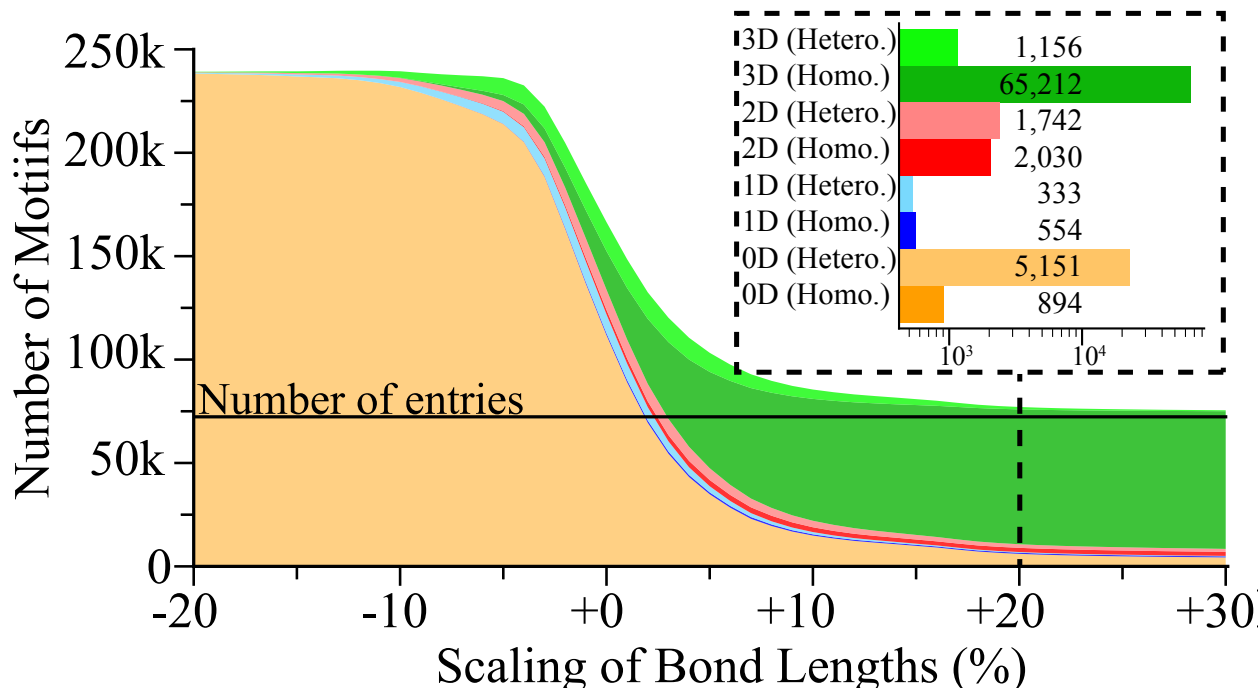
Figure 3-2. Distribution of structural motifs identified by the TSA as a function of scaling of the bond length criteria, i.e., the sum of empirical atomic radii. The figure is limited to materials which are reported as within 50 meV/atom of the thermodynamic hull. For materials where a heterostructure was identified (i.e., the composition of individual structural motifs does not match the materials composition), each atomic network with a unique composition is categorized separately. The number of conventionally networked materials increases rapidly up to a scaling of about +10%. We select a scaling of +20% to capture almost all covalent, ionic, and metallic bonds but not bridge the majority of van der Waals gaps.

in the pymatgen software package[41] and scale the values from -20% to $+30\%$ in steps of 1% to identify bonds.

Figure 3-2 illustrates the distribution of structural motifs for all materials within 50 meV/atom of the thermodynamic hull. Unsurprisingly, the unscaled atomic radii result in the classification of a large fraction of crystal structures into molecular heterostructures. To ensure accurate identification of the bonds and capture the structural motif of each crystal correctly, we increase the atomic radii by $+20\%$. This scaling ensures the correct identification of almost all covalent, ionic, and metallic bonds while not including second nearest neighbors and weak vdW bonds. We note that for any empirical bonding parameter, there is a small

fraction of incorrectly identified materials. An example of this is 2D PbS. The Pb and S species exhibit atomic radii of 1.8 and 1.0 Å respectively. In the PbS structure, the distance between nearest neighbor Pb and S atoms is 3.01 Å, which requires a minimum increase in atomic radii of 7.5% for the TSA to identify these species as bonded. However, at increased radii of 8.4%, the Pb atoms of neighboring vdW bonded layers are identified as a covalently bonded. Though the number of misidentified structural motifs is apriori unknown, visual inspection of a subset of materials and the apparent convergence of the structural motifs with further increase in the scaling of the bond length indicates that the number of misidentified cases is relatively small for a scaling of +20%.

Figure 3-2 shows that the number of identified structural motifs is larger than the number of considered crystal structures (72,316). The reason is that some crystal structures comprise multiple structural motifs. The structural motifs of these heterostructures can differ in both their chemical composition and their dimensionality, e.g., heterostructures of 0D and 2D motifs. Across the 3,632 chemical heterostructures, 1,850 have mixed dimensionality. We do not consider chains obtained from heterostructures, as they would not be easily exfoliable and may be charged and, thus, very unstable when isolated.

Though changing the supercell size should not change the structural motif of a crystal, we find several materials that display structural motifs whose dimensionalities depend on the supercell size chosen. For example, the monoclinic phosphorous crystal with Materials Project ID mp-568348 and Inorganic Crystal Structure Database (ICSD)[451] ID 29273 is identified as a 1D solid with a $2 \times 2 \times 2$ supercell and 2D solid with a $3 \times 3 \times 3$ supercell. Figure 3-3 displays the crystal structure and illustrates how periodic boundary conditions can result in incorrectly identified structural motifs. As shown in Figs. 3-3(c) and (d), building the network of bonded atoms results in different connectivity for the 2×2 and 3×3 supercells. When the periodic boundary condition is eliminated, the bonding network consists of two truly separate structural motifs exhibits, indicating that using periodic boundary conditions to characterize the network topology can be misleading. We identify 63 homogeneous crystals that display a change in the

dimensionality of their structural motifs with supercell size. We find that all these materials exhibit a similar bipartite bonding network topology as the phosphorus example.

3.3.2 Exfoliation and Structural Stability of 1D Nanowires

From our starting set of 120,612 crystals, 3,174 crystals comprise of 1D motifs, 554 of these crystals are within 50 meV/atom of the thermodynamic hull, indicating experimental accessibility. Of these, 404 crystal structures possess an entry in the ICSD[451] and thus are proven to be experimentally accessible. We further focus our search to materials that include at least one *d*-valence element, as such species in low-dimensional systems have the potential for strong correlations and magnetism. This results in 295 crystal structures with 1D structural motifs, which we characterize further using DFT.

We exfoliate the 1D nanowire structures from the parent crystal structures and evaluate their stability. We compare the energy of the isolated nanowire structure with that of the lowest energy bulk phase of the same chemical composition. We use two criteria to describe nanowire stability. The first is the exfoliation energy

$$\Delta E_{\mathrm{exf}} = \frac{E_{\mathrm{chain}}}{N_{\mathrm{chain}}} - \frac{E_{\mathrm{bulk}}}{N_{\mathrm{bulk}}}, \tag{3-1}$$

where E_{chain} and E_{bulk} denote the energy and N_{chain} and N_{bulk} the number of atoms in the unit cell of the isolated 1D chain and the bulk structure, respectively. The exfoliation energy measures the thermodynamic stability of the 1D material against formation of the ground state bulk phase. The second criterion is the line tension

$$\sigma = \frac{N_{\mathrm{chain}}}{a_{\mathrm{chain}}} \Delta E_{\mathrm{exf}}, \tag{3-2}$$

where a_{chain} is the unit cell length of the 1D chain structure. The line tension is the 1D analog to the surface energy of 2D materials and renormalizes the exfoliation energy by the linear atom density of the nanowire. Similar to the 2D case, the line tension stability criterion avoids the bias of the formation energy towards thicker nanomaterials.[23, 436]
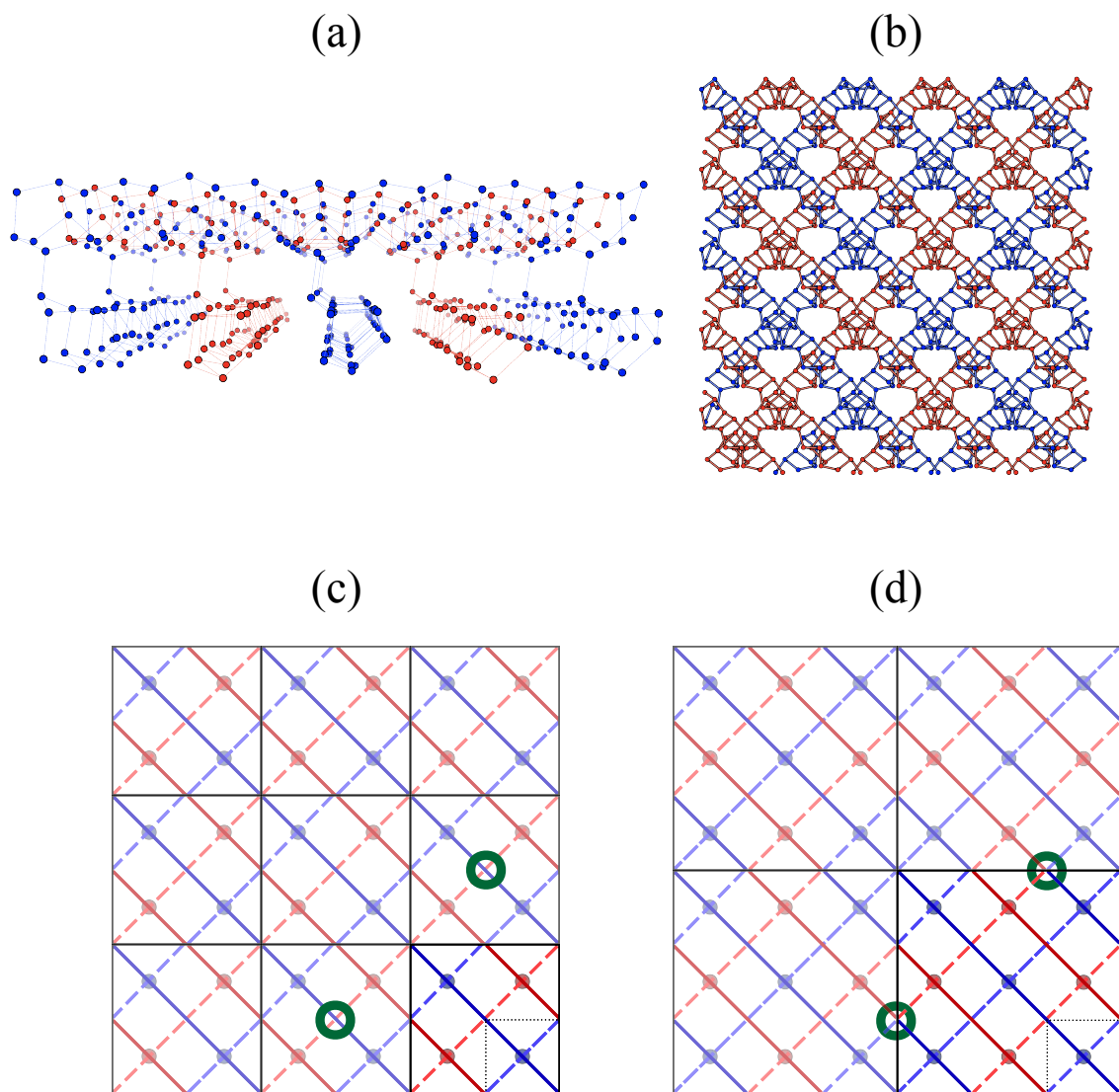
Figure 3-3. Effect of periodic boundary conditions on the dimensionality of structural motifs. The phosphorous bipartite structure comprises two separate bonding networks represented in red and blue. (a) The crystal structure consists of two networks of linked rod-like motifs. The top and bottom sets of atoms form equivalent structures that are related by a 90° rotation and connected through bridges. (b) The top-down view shows the bipartite network structure. (c) and (d) display 6×6 supercells of the unit cell, based on 2×2 and 3×3 supercells, respectively. The dashed lines represent the bottom rods, while solid lines represent the top rods. The green circles highlight the conflicting network connectivity for the 3×3 supercell (d), which shows the blue network incorrectly connected to the red one.

95

Figure 3-4 compares the line tensions and exfoliation energies for the nanowires with the values for a single chain of Te. We use the Te nanowire as a reference to classify the stability of the 1D materials. This nanowire forms a 3-fold-symmetric helical coil, abbreviated as 3H. Though a free-standing Te nanowire has not yet been synthesized, the thin film precursor[445] and a 3H-Te nanowire encapsulated in a carbon nanotube have been synthesized.[13] That linear Te nanowire was theorized to exhibit a Peierls distortion, which was, however, not seen in the experiments, possibly due to limitations in imaging technology.[13] In this work, we focus on the exfoliated helical coil 3H-Te nanowire. We test the exfoliated 3H-Te nanowire for Peierls distortions using supercells of doubled, tripled, and octupled unit cells with random perturbations of the atomic positions of 0.1 Å. We find that all supercells relax back to the undistorted structure, indicating the absence of Peierls distortions in the 3H-Te extended Te nanowire. Though other nanowires have also been synthesized within carbon nanotubes,[14–17,431] Te is the only known material identified with a thermodynamically stable bulk precursor composed of a nanowire structural motif. Sulfur exhibits a bulk phase with a 1D structural motifs, and a sulfur nanowire has been encapsulated in a carbon nanotube.[14] However, the sulfur nanowire structure differs from that of the 1D motif of the bulk precursor. Therefore, the 3H-Te nanowire presents the most relevant system for the stability standard of nanowire materials. We expect the criteria for thermodynamic stability to evolve as more exfoliable nanowires are synthesized and growth techniques develop over time.

After structural optimization, a total of 255 systems had both the exfoliated nanowire and bulk precursor successfully converge. Using the exfoliation energy of 3H-Te as the stability criterion, we observe that all considered nanowires are stable. However, using the line tension, which accounts for wire thickness, less than half of the exfoliated nanowires are sufficiently stable. Visual inspection reveals that the now unstable chains have a much larger radius than the other identified 1D materials, confirming that the line tension successfully acts as a 1D analogue to the 2D surface energy for measuring stability. We find that 78 nanowires

meet both the exfoliation energy and line tension stability criteria, and we consider them as sufficiently stable for synthesis.

Of the 255 nanowires, 232 unique chemical compositions are present. 21 chemical compositions appear more than once, an average of 2.1 times, with each nanowire being exfoliated from a unique precursor. Some of the precursors are very similar polymorphs, providing insight into the metastability of the phases. One example is niobium oxychloride ($NbOCl_3$), for which two unique bulk precursors exist. The exfoliated nanowires from each phase differ in their thermodynamic stability by 4 meV/atom and their line tension by 15 meV/Å. The lower energy exfoliated nanowire is also less symmetric, with the space group symbol of the low and high energy phase being C_{mm2} and C_{mmm}, respectively. The difference in symmetry is a result of the difference in the bond lengths of the O-Nb-O triplet. The bonds differ in length for the low energy phase, breaking the mirror plane and lowering the overall symmetry. This represents a Peierls distortion in the system, which was only identified in one of the optimized systems.

3.3.3 Magnetic Nanowires

The magnetic moment of all nanowires is shown in Fig. 3-4(b). We require a minimum magnetic moment per magnetic d species to be .1 Bohr magneton (μ_B) for a chain to be considered magnetic. We observe several integer magnetic moments, which indicates that these are magnetic semiconductors. We have found examples in which some of the d valence species do not contribute to magnetic behavior ($AgTa_2F_12$, 1 μ_B), though this is uncommon. For each integer magnetic moment, we identify the lowest energy nanowire (normalized by number of d species) and perform further calculations. First, we calculate the ferromagnetic (FM), non-magnetic (NM), and antiferromagnetic (AFM) energies for each chain, with AFM orderings of alternating moments ($+ - +-$), and paired moments ($+ + --$). Second, we test for Peierls distortions in the FM configuration by doubling and tripling the chain length, displacing the atomic positions by .1 Å, and reoptimizing the nanowires. We report this information in Table 3-1.
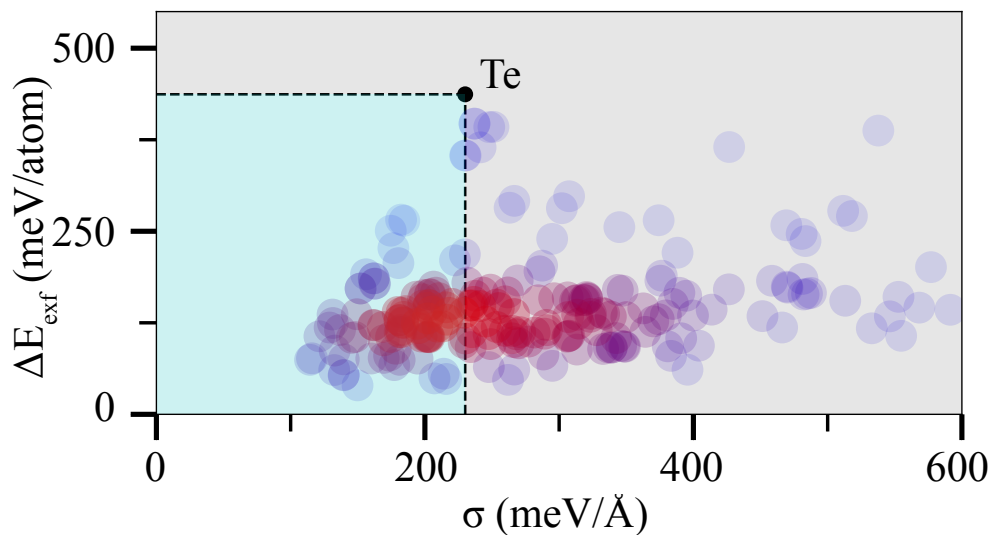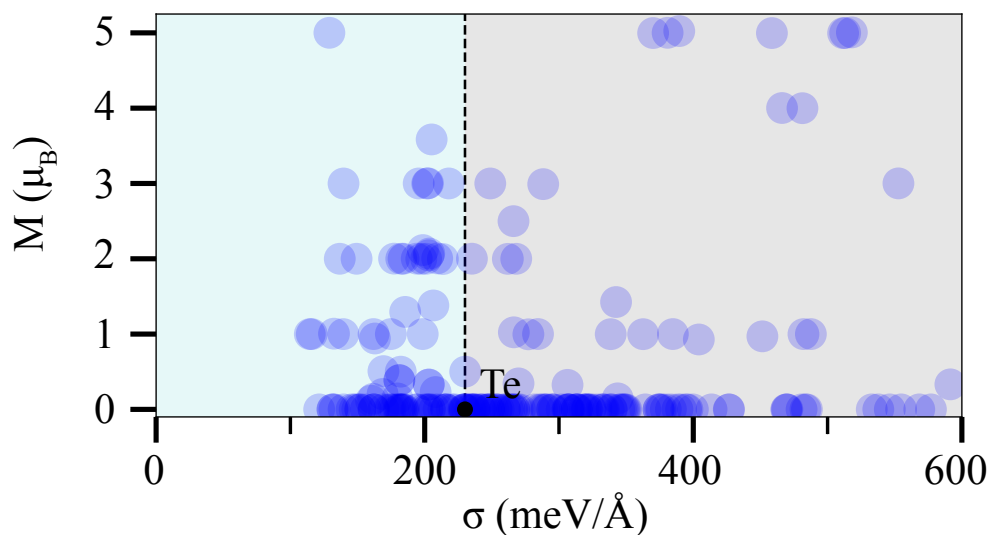
Figure 3-4. Density scatter plots for line tension, exfoliation energy, and magnetism. This is shown for (a) the line tension and exfoliation energy, and (b) the line tension and average magnetic moment, normalized by the number of *d* orbital elements. The black circle represents single-chain 3H-Te, which provides an empirical stability criterion indicated by the light blue region. A total of 78 nanowires meet both exfoliation energy and line tension forms of thermodynamic stability.

Table 3-1. Nanowire stability with various magnetic ordering

		Ferromagnetic			AFM		NM
	M	$1\times$	$2\times$	$3\times$	$+-+-$	$++--$	
MoF_5	1	114	116	116	114	118	144
$TiAl_2Cl_4$	2	198	198	197	218	198	332
$TcCl_4$	3	195	195	195	193	191	378
$FeH_4C_2O_6$	4	386	385	403	386	387	462
$FeCl_3$	5	126	126	128	98	110	454

We reach two conclusions from these results: all nanowires prefer any magnetic ordering over no ordering, and several wires have no strong preference for ordering. The energy barrier between these orderings is show to be small for all phases except $FeCl_3$, which shows a preference for $+-+-$ ordering. Only one system ($TcCl_4$) has the $++--$ as the ground state, though the energetic barriers to other orderings is low. The tripled FM cell of $FeH_4C_2O_6$ is notably higher energy than the other FM cells after full geometric optimization. Visual inspection reveals that the chain is somewhat compressed after relaxation (15.93 vs 16.20 Å) compared to the original supercell. When the a lattice was set to 16.2 Å, the cell contracts back to 15.93 Å. We attribute the differences in other FM supercells to the previously described metastability and complex energy landscape.

3.3.4 Electronic Structures

The PBE band gaps of the nanowires are shown in Fig. 3-5. We organize the materials in order of ascending smallest band gap. Several metals and insulators are shown, with many materials having a large difference in spin gap. This can be utilized for the development of a variety of nanoelectronic designs. In addition, we identify several half-metallic nanowires. It is known that higher-level calculations are needed to accurately determine half-metallicity,[452] and that there is the potential for Peierls distortions in these systems. Nonetheless, these materials are a potential avenue for developing nanoelectronics.

3.4 Summary

In summary, the Materials Project database was searched over for novel 1D materials using the Topological Scaling Algorithm. A cutoff of 120% of the covalent radius was considered
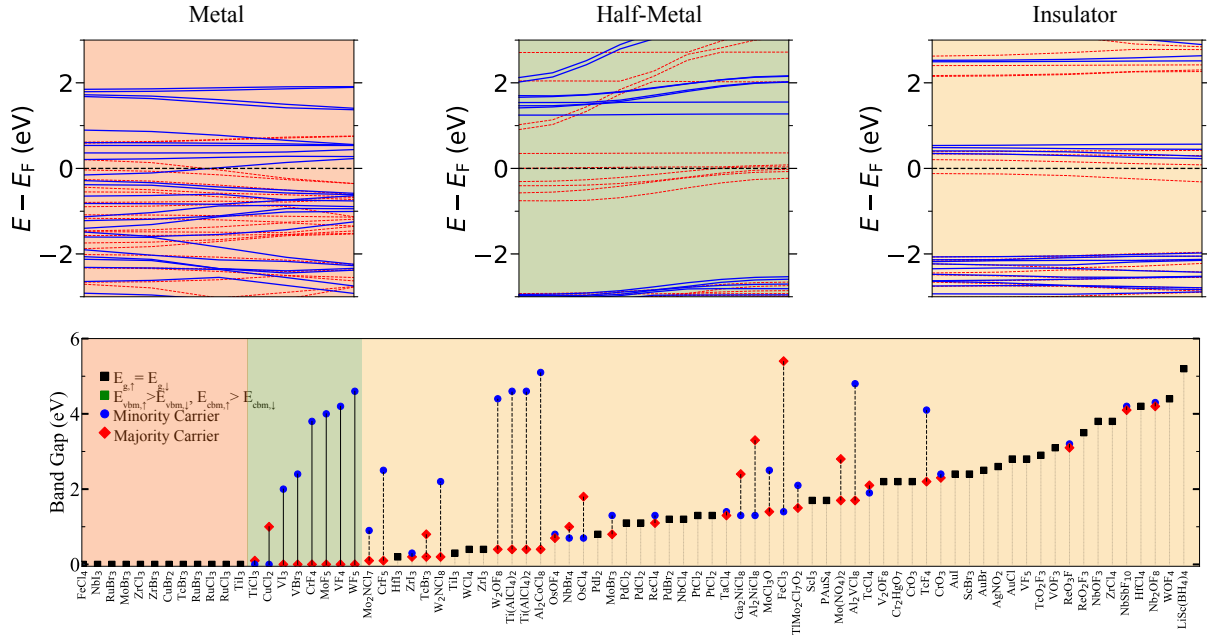
Figure 3-5. The band gaps of the 78 nanowires with thermodynamic stability comparable to 3H-Te. All band gaps are shown in the bottom plot with example band structures for each type (top). The bottom plot is ordered based on the magnitude of the smallest band gap, followed by the magnitude of the largest band gap. Red diamonds indicate that the given spin is the majority carrier, while blue dots indicate the spin is a minority carrier. Black squares indicate that the spins are equivalent, with respect to gap size and positions of the band edges. The dashed grey lines are used to guide the eye, while black lines are shown to connect the two dots. Red, green, and orange shading indicates the materials that are metallic, half-metallic, and semiconducting, with example band structures shown at the top of the figure. All semiconductors are staggered gap.

for building networks, resulting in 437 1D materials. 263 of these chains contain d electron elements, which contain the highest potential for correlation effects and were studied in this work. The stability of these chains were calculated in both energy per atom and energy per Angstrom. We used single chain Tellurium as the benchmark of stability, and found that nearly all the chains fall within the energy per atom, while 78 fell below the energy per Angstrom criteria which was used to screen for later calculations. A wide variety of electronic behavior was displayed by these chains, including half metals and magnetic insulators with significantly different band gaps. Future investigations into these materials can be determine how the

magnetic moments orient themselves within these chains, which will inform the potential applications of these chains in electronic devices. Further, testing these materials for Peierls distortions and identifying how said distortions will change their electronic structure will be critical to determining their potential applications in nanoelectronics.

CHAPTER 4
COMPUTATIONAL SYNTHESIS OF SUBSTRATES BY CRYSTAL CLEAVAGE

This chapter is an extension and further development of the topological scaling algorithm.[22] To begin, the TSA is used to identify fully periodic crystals. Following, bonds are broken in the atomic network in an attempt to generate a surface. If a surface is cleaved by breaking these bonds, it is recorded and the slab is stored. This search is performed on crystals with five or fewer atoms in the primitive cell, with a maximum of 3 bonds broken. This results in 4,708 surfaces cleaved across 2,136 crystals. I partially optimize the monolayer of each cleaved surface and identify 3,730 potential substrates with surface energies comparable to experimentally used substrate materials. I follow by analyzing how the energy-per-bond of a cleaved surface correlates with the electronic structure for the parent phase, identifying distinct trends we attribute to metallic and ionic/covalent bonds being the predominant bond broken. With a database of substrate materials, we test the usefulness of said database by epitaxially matching the precursors within to $BaSnO_3$, identifying potential substrates with an order of magnitude lower strain than currently used substrates.

4.1 Background

Single-crystal substrates facilitate the epitaxial growth of crystalline thin films based on their surface similarity, in terms of lattice parameters and symmetry. Many single-crystal substrate materials are commercially available with different facet orientations. However, while exfoliated 2D materials such as graphene are naturally smooth, cleaving a crystal does not guarantee an atomically smooth surface. Energetic instabilities of cleaved facets can result in the formation of various defects that limit the quality of a substrate for synthesis efforts. Identifying a wider range of substrates with low surface energies would enable the growth of high-quality materials by minimizing the presence of undesirable defects. For example, the cubic perovskite $BaSnO_3$ has diminished electronic properties due to the lattice mismatch of its (100) surface and the substrates suitable for its growth.[453–455]

The discovery of two-dimensional (2D) materials present similar challenges to substrates, most notably that both require materials with low surface energies. Computational efforts to identify novel 2D material have significantly expanded the list of potential monolayers and helped guide experimental synthesis.[22, 24, 28–31, 33, 34] One discovery technique is data mining, which searches bulk materials databases for yet unidentified monolayers.[22, 24, 28–31] A recent effort in this direction identified and characterized the bonding network of a crystal structure using the topological scaling algorithm (TSA).[22] This algorithm identifies bonding clusters within a finite number of unit cells, then uses the scaling of this network size as a function of supercell size to define dimensionality and was used to discover over 600 low-energy 2D materials.[22]

In this work, we present an approach to identify novel substrates, which utilizes the computational cleavage of bulk crystals. This effort is motivated by our recent 2D structure search using the genetic algorithm software GASP[60, 456] for the Ga_2O_3 system. In that search, we identified a monolayer structure that can be cleaved from the bulk crystal and was already experimentally synthesized.[457, 458] Thus, we use data mining techniques to discover planes of cleavage in fully periodic crystals. Rather than using the TSA to identify van der Waals gaps, we use it first to identify conventionally bonded solids; then, we systematically break bonds in the crystal to create a low-dimensional structure. When the breaking of bonds generates a surface (i.e., gives the material a 2D structural motif), we extract a single monolayer and calculate the work of adhesion (i.e., the energy cost required to cleave the crystal and form two surfaces), using density functional theory (DFT). This approach identifies nearly 4,000 potential substrates with surface energies comparable to experimentally used substrates and some with formation energies comparable to free-standing 2D materials.[436]

4.2   Methods

4.2.1   Characterization of Cleaved Materials

To calculate the stability of the cleaved surfaces, we perform density functional theory (DFT) calculations with the projector-augmented wave (PAW) method as implemented
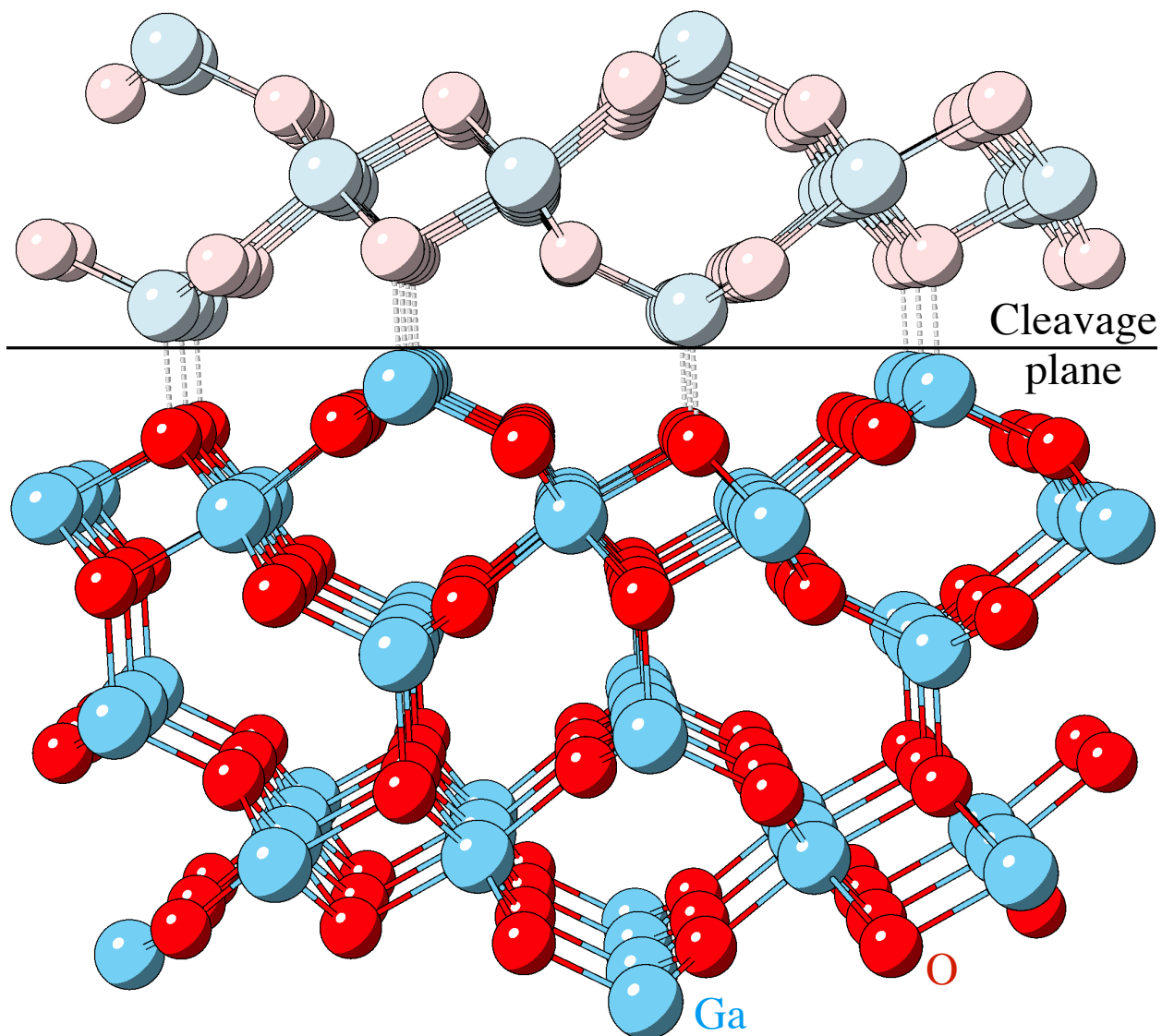
Figure 4-1. Example of a cleavable crystal, Ga_2O_3. The $(20\bar{1})$ plane exhibits a low density of bonds that, when cleaved, creates a low energy surface.

in the VASP package.[447,448] The choice of PAW potentials follows the recommendation of pymatgen.[37] We employ the Perdew-Burke-Ernzerhof (PBE)[459] approximation for the exchange-correlation functionals. To obtain convergence of the energy to 1 meV/atom, we use a Γ-centered k-point mesh with a density of 60 k-points per $Å^{-1}$ and a cutoff energy for the plane-wave basis set of 600 eV. For the 2D materials, we employ a vacuum spacing of 14 Å and reduce the number of k-points in the out-of-plane direction to 1. The DFT calculations are performed spin-polarized with an initial ferromagnetic configuration. Transition metal

atoms are initialized with a magnetic moment of 6 μ_{bohr} and all others with a moment of 0.5 μ_{Bohr}.

4.2.2 Workflow

We use the software packages pymatgen[41] and MPInterfaces[42] to prepare the input files, organize the results for the cleavage algorithm, and analyze the results of the DFT calculations. We use the pymatgen structure matching algorithm with an atomic position tolerance of 10^{-4} and not permitting any primitive cell reduction, lattice scaling, or supercell transformations.[37] Decreasing the tolerance to 10^{-5} only marginally increases the number of unique surfaces by 27, indicating that the choice of 10^{-4} provides high confidence in the uniqueness of the identified substrates. We fully relax all bulk precursor structures. To improve the efficiency of the materials screening for the large number of candidate cleaved materials, we relax each cleavage surface for a maximum of ten ionic steps, though not all extracted surfaces required that many steps for convergence. Any surfaces for which the bulk precursor did not converge are excluded from this study. Any surfaces which either diverged in energy or changed in surface area by more than 40% are excluded as well.

4.3   Results

4.3.1   Candidate Materials

For our study, we select all materials in the MaterialsProject database[37] with five or fewer atoms in the primitive unit cell and within 50 meV/atom of the convex hull, the latter to promote thermodynamic stability. Next, the topological scaling algorithm (TSA) identifies conventionally networked structures from this subset and creates a list of all bonds between neighboring atoms in these crystals. The bonding identification utilizes the empirical atomic radii of the elements, as provided in the pymatgen software package,[41] which we increase by 10%.

4.3.2   Bond Cleavage

We implement two approaches for cleaving bonds in a crystal structure that are illustrated in Fig. 4-2. The first approach breaks all periodic instances of a bond between two atoms in
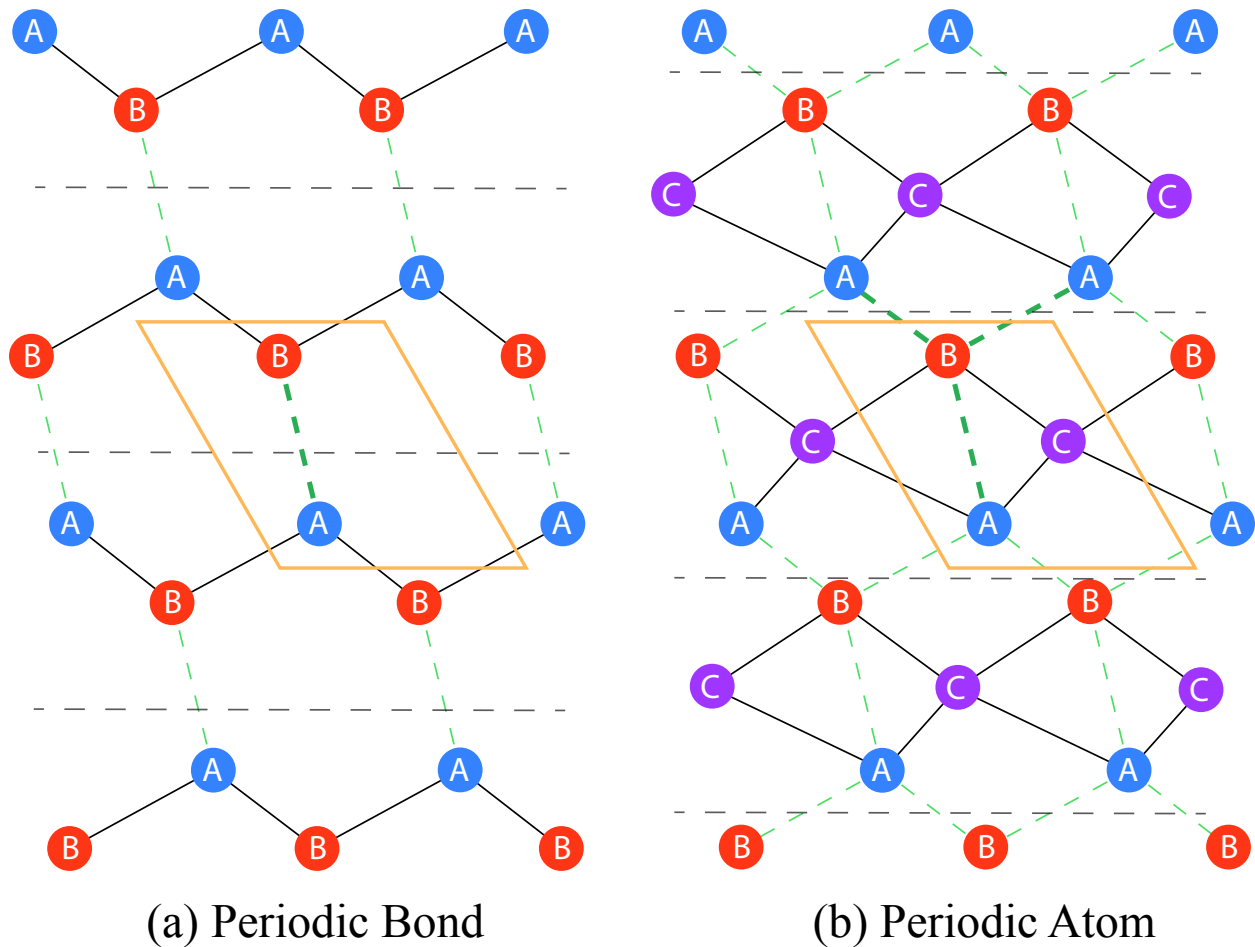
Figure 4-2. Bond cleaving algorithm. (a) The periodic bond approach cleaves all periodic images of a bond. (b) The periodic atom approach cleaves the bonds between all periodic images of the atoms. The periodic atom approach requires at least three atoms in the primitive cell to generate a cleaved facet.

the supercell and is denoted as the "periodic bonds" approach. In this case, the three A-B bonds shown in Fig. 4-2(a) are treated separately. The second approach breaks the bonds between all periodic instances of the atoms in the supercell and is referred to as the "periodic atom" approach, illustrated in Fig. 4-2(b).

We systematically break unique bonds in the primitive cell up to a maximum number of bonds given by

$$N_{\text{bonds}} = \text{round}\left(\alpha\, N_{\text{atoms}}^{2/3}\right), \tag{4-1}$$
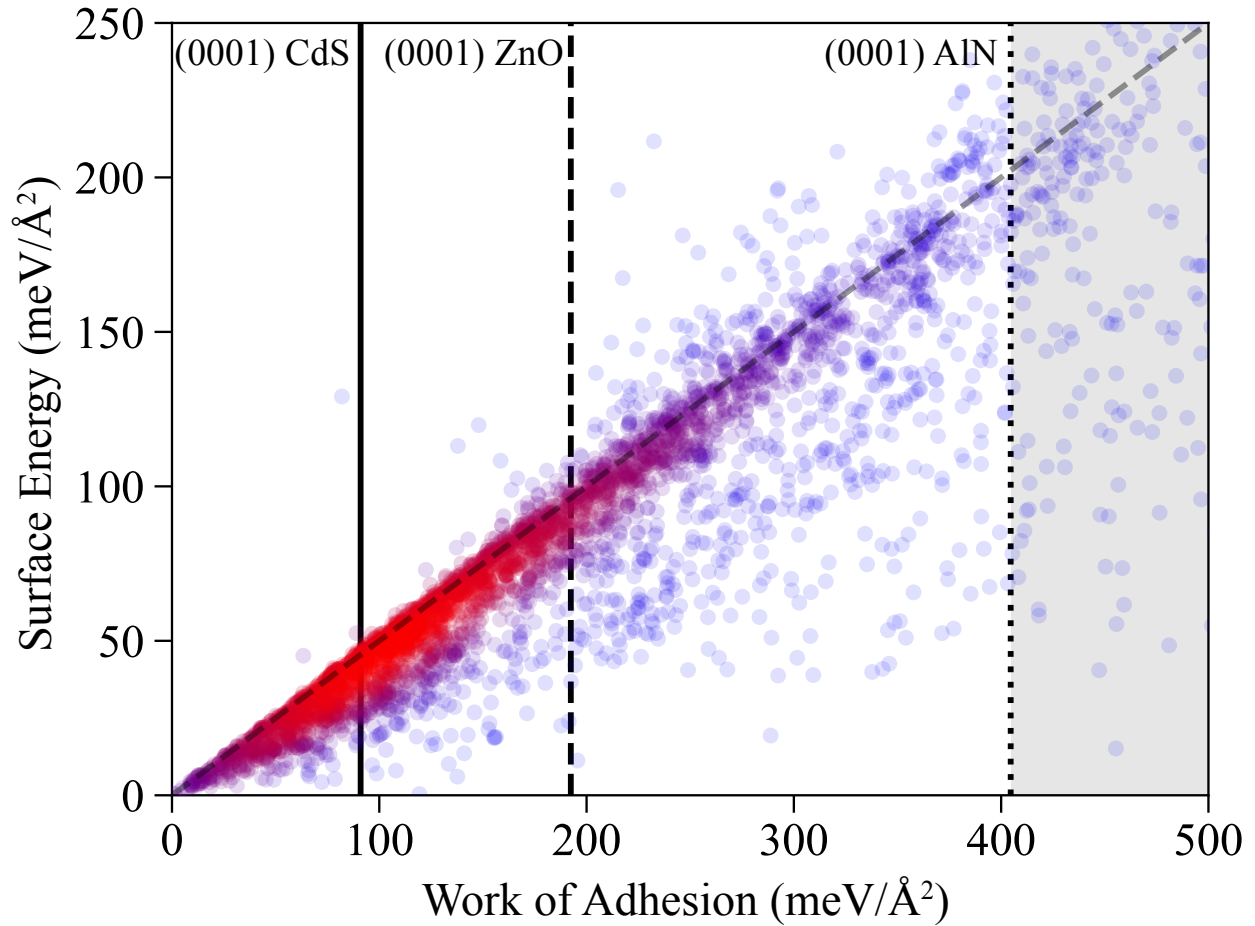
Figure 4-3. The work of adhesion and the surface energy after ten relaxation steps of the cleaved surfaces. Red indicates a higher density of points. The solid, dashed, and dotted black lines represent the work of adhesion of the (0001) CdS, ZnO, and AlN substrates, respectively. The grey region indicates materials have a work of adhesion greater than common substrates.

where N_{atoms} is the number of atoms in the primitive cell, and α is a scalable parameter based on the desired maximum number of bonds broken. The exponent of 2/3 appropriately scales the number of bonds per plane with increasing cell size. The choice of $\alpha = 1$ in this work results in one to three cleaved bonds in primitive cells of one to five atoms. For the periodic bond approach, N_{bonds} scales with the square of the supercell size. For the periodic atom approach, N_{bonds} scales at least with the square of the supercell size, with the potential to break a significantly larger number of bonds. The periodic atom approach fails for two-atom

| (a) Any precursor (4,325) | (b) Metallic precursor (2,591) 1.4 eV/bond | (c) Insulating precursor (1,734) 1.9 eV/bond |
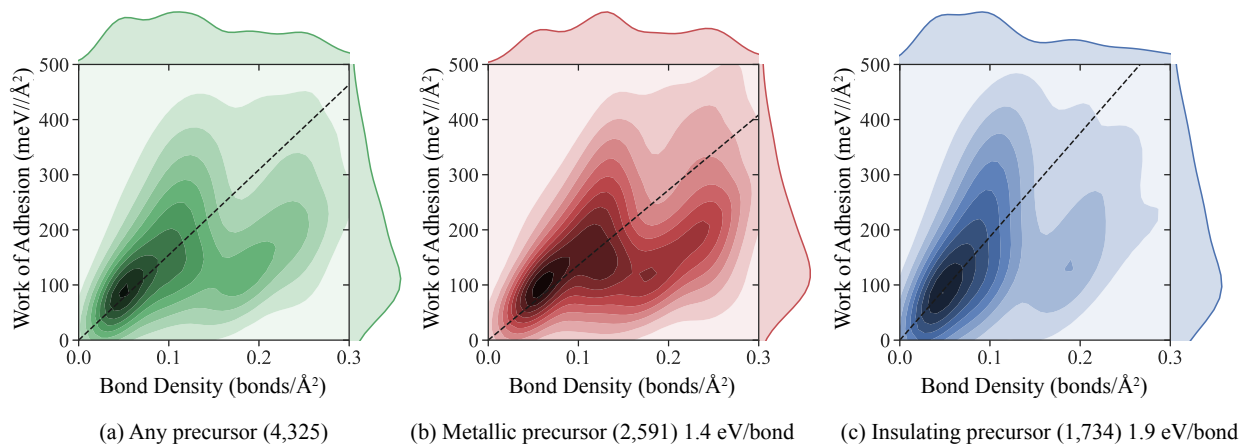
Figure 4-4. Distribution of the work of adhesion vs. bond density of cleaved surfaces, represented by kernel density estimation: (a) for 4,325 cleavage surfaces, (b) for surfaces with metallic precursors, and (c) for surfaces with precursors exhibiting an electronic bandgap. We use the bandgap reported by Materials Project for the bulk precursors of the surfaces. The dashed lines indicate the mean energy per bond. On average, the metallic precursors exhibit a higher coordination number, and hence bond density for the cleavage plane in conjunction with a lower energy per bond than the more covalent and ionically bonded precursors. This trend is reflected in the average energy of the cleaved bonds for metals being lower at 1.4 eV/bond compared to 1.9 eV/bond for the cleaved covalent and ionic precursors.

unit cells, and, with increasing unit cell size, converges to the results of the periodic bond approach.

4.3.3   Topology of Resulting Structure

To determine if a cleavage surface has been generated, the TSA is run on the primitive cell with N_{bonds} or fewer bonds broken (using either approach). If the TSA identifies a two-dimensional structural motif with the same stoichiometry as the overall cell, we have created a cleavable surface. This surface is isolated as a monolayer and oriented such that the $\vec{a}$ and $\vec{b}$ lattice vectors span the 2D lattice of the monolayer structure and the $\vec{c}$ lattice parameter is chosen perpendicular to the $(\vec{a}, \vec{b})$ plane. Due to the crystal symmetry, our algorithm can identify multiple instances of some surfaces. We remove these duplicates and identify the unique surfaces extracted from each crystal using the pymatgen structure matching algorithm.[37]

4.3.4 Predicted Substrates

From a starting set of 120,612 materials in the Materials Project database,[37] 9,309 crystals meet the criteria of exhibiting (i) an energy within 50 meV/atom of the thermodynamic hull (72,316), (ii) a primitive cell of 5 or fewer atoms (9,980), and (iii) a bonding network of three-dimensional topology. Applying the periodic bond and periodic atom cleavage approaches to the 9,309 materials generates 1,929 and 3,928 unique surfaces, respectively. Applying the structure matching to the combined list of 5,857 surfaces, we identify a total of 4,708 unique cleaved surfaces across 2,136 bulk crystals. It is worth noting here that Ga_2O_3 is not identified as cleavable by this search, as (i) the number of atoms in the primitive cell of the crystal is greater than five and (ii) the TSA identifies the crystal as layered when using our choice of 1.1 times the atomic radii of Ga and O, rather than as a fully networked structure.

To determine the stability of the surfaces, we perform DFT calculations with VASP.[447,448] We extract monolayers for each of the identified 4,708 unique cleavage surfaces and optimize the structure of the surfaces and their bulk precursors; 2,115 bulk precursors phases successfully underwent structural optimization, and 4,325 monolayers remained structurally intact and changed by less than 40% in surface area. A sizable number of 1,802 of these surfaces contain f-valence elements, for which semilocal exchange-correlation functionals exhibit larger formation energy errors.[38] Therefore, care should be taken when considering these materials in the MaterialsWeb.org substrate database.

We use the work of adhesion of a monolayer to describe the thermodynamic stability of a surface. The work of adhesion measures the energy required to cleave a material, and the surface energy of a material's facet measures the thermodynamics stability of said facet. To validate that a monolayer accurately approximates the work of adhesion for cleaving a crystal, we calculate the change in work of adhesion with slab thickness for a subset of 21 (001) surfaces, from one to four unit cells. We find changes in the work of adhesion of less than 3 meV/$Å^2$, confirming that monolayers accurately describe the work of adhesion for a cleaved surface. To verify that the work of adhesion indicates surface stability, we compare
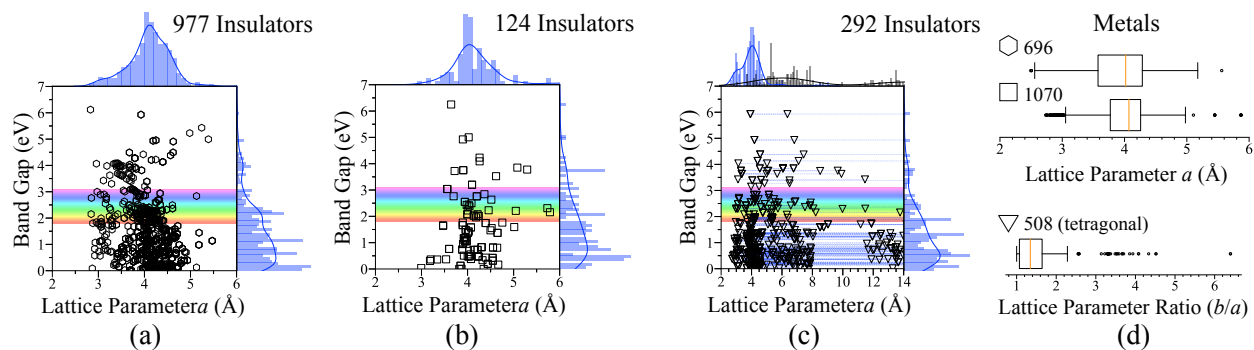
Figure 4-5. Lattice vectors, bandgaps, and their kernel density estimates for the electronic structure information of the substrates. (a) shows the distribution for hexagonal substrates, (b) square, and (c) tetragonal substrates with insulating precursors. For the tetragonal substrates in (c), the *a* and *b* lattice vectors are both plotted and connected with a dashed line, and the *b* kernel density is plotted in grey. For substrates with metallic precursors, (d) shows boxplots for the hexagonal and square substrates and the *b/a* ratio of the tetragonal ones. The 63 monoclinic surfaces are not represented here.

the calculated work of adhesion for 4,325 cleaved, free-standing monolayers to their partially-optimized surface energy in Fig. 4-3. We observe that 2,182 materials display surface energies within 10% of half their work of adhesion and 1,433 within 5%. Importantly, in most cases, the work of adhesion is larger than the surface energy, demonstrating that it is an effective metric for surface stability.

4.4   Discussion

Our search identifies several surfaces that are currently used as substrates, including (0001) CdS, ZnO, and AlN. Figure 4-3 highlights 3,730 surfaces (2,188 *f*-valence free) with a work of adhesion below that of (0001) AlN, and 846 surfaces below that of (0001) CdS. We also identify 249 materials that exhibit formation energies less than that of 2D-SnSe,[166, 460] indicating the possibility that these 249 materials could be synthesized as free-standing materials.[436]

Figure 4-4 analyzes the trend between the number of cleaved bonds and the work of adhesion across the 4,325 cleaved surfaces. The joint distribution in Fig. 4-4(a) indicates that our cleavage criterion of Eq. (4-1) results in both a low density of cleaved bonds and a moderate spread of work of adhesion. Furthermore, the distribution indicates two clustering

trends in the plot, which correspond to different average bond energies. We attribute these trends to different types of chemical bonds being broken. Metallic systems typically display high coordination numbers and somewhat lower bond energies. Covalent and ionic bonds share localized electrons, which results in lower coordination numbers and higher energies per bond. To test this hypothesis, Figures 4-4(b) and (c) show the work of adhesion and bond density distribution for monolayers derived from metallic and insulating precursors, respectively, based on the precursor bandgap reported in the MaterialsProject database.[37] We observe that the two clusters in the distribution indeed correspond predominantly to metallic and covalent/ionic bonding with average bond energies of 1.4 and 1.9 eV/bond, respectively.

To determine the potential of our data mining approach to expand the set of known substrates, we characterize the cleavage surfaces' symmetry and lattice parameters. Figure 4-5 illustrates the lattice parameter distribution of the hexagonal, square, and tetragonal substrates identified in this work, as well as the electronic properties of their bulk precursors. The broad range of electronic behavior and lattice parameters for each symmetry indicates that these cleaved crystals could provide suitable substrates for a variety of thin-film systems.

To demonstrate the impact of this substrate database, we epitaxially match cubic perovskite (100) $BaSnO_3$, using the crystal structure and stiffness tensor provided by MaterialsProject[37,461] to substrates with a work of adhesion below that of (0001) AlN. We use the pymatgen[41] lattice matching algorithm to epitaxially match the perovskite to the layers extracted in our search. We identify 34 cleavage surfaces when using the screening criteria of (i) a work of adhesion less than that of (0001) AlN, (ii) a strain energy below 1 meV/atom, (iii) no f-valence species, and (iv) epitaxial matches to a single unit cell of $BaSnO_3$.

We highlight here three potential substrates: (001) Rb_2NiO_2,[462] (001) NiO,[463] and (001) CaSe.[464] The work of adhesion for each substrate is small, being 23, 36, and 28 meV/$Å^2$, respectively. The resulting epitaxial strain of $BaSnO_3$ for Rb_2NiO_2 and NiO are also small, with only $+0.3\%$ and $+0.4\%$, which correspond to strain energies of 0.2 and 0.4 meV/atom, respectively. These are an order of magnitude smaller than currently used substrates such as

(001) $SrTiO_3$ (-5.4%) and (001) MgO ($+2.2\%$) indicating the opportunity for defect-free growth of $BaSnO_3$ on these new substrates. The strain energy when using CaSe is larger at 1.3 meV/atom, though still with a low lattice mismatch of $+0.7\%$. All three precursor materials – Rb_2NiO_2, NiO, and CaSe – have been experimentally synthesized,[462–464] providing new opportunities for the growth of $BaSnO_3$.

To facilitate the use of these substrates for further studies and future synthesis efforts of epitaxial single-crystal thin-films, we provide the substrate structures and the data on their stability under an open-source license at MaterialsWeb.org. Furthermore, we make the software for cleaving crystal structures available as part of the open-source MPInterfaces package.[42, 465]

4.5 Summary

In conclusion, we developed a data mining approach that systematically breaks bonds in three-dimensional crystals to identify cleavage planes for substrate synthesis. We identify 4,708 unique cleavage surfaces across 2,136 periodic crystals and determine their structure and stability. We show that 3,730 surfaces display a work of adhesion comparable to that of the known substrate material (0001) AlN. These cleavage surfaces show a broad distribution of electronic properties and lattice parameters. We illustrate their utility by identifying three substrates for $BaSnO_3$ with epitaxial matches that are an order of magnitude better than currently used substrates. Though we limited our search to small primitive cells, the low surface energy of Ga_2O_3 indicates that there are many more low-energy substrates which can be cleaved from periodic crystals.

CHAPTER 5
LAYER GROUP IDENTIFICATION TOOL FOR SYMMETRY OF 2D MATERIALS

This chapter is an exploration and development of software for specifically treating 2D materials, with regard to symmetry and structure. The majority of open-source tools used in computational materials science is designed for fully periodic crystals. This creates problems for 2D materials, which lack periodicity in one direction. This restriction is not properly treated by these software packages, leading to potential errors when calculating electronic structure and performing primitive/conventional cell generation on these crystals. To approach this problem, I begin by discussing how to standardize 2D unit cells to explicitly address the reduced periodicity. Following, I use the layer groups to describe the symmetry of these systems, which consider three dimensions of space, but only two dimensions of periodicity. The flow of the algorithm is outlined, which is then applied to 2D materials exfoliated using the same algorithm discussed in Ch. 3 and the surfaces cleaved in Ch. 4. I then the chapter by providing a complete list of high symmetry pathways in 2D materials, based on the five possible Bravais lattices which exist for 2D materials. I end the chapter by discussing extensions of this algorithm and potential applications beyond determining the layer group.

5.1   Background

Symmetry in periodic crystals is critical to properly understanding their properties and behavior. For example, the point group operations that describe the symmetry within a crystal can be used to reduce the form of tensors (such as elastic and piezoelectric). To describe two-dimensional (2D) material symmetry, both wallpaper groups and space groups have been used. The former describes symmetry for systems which exist in 2D and have two dimensions of periodicity. This has well established applications, being critical for analyzing and creating art used across world and time.[466] While the wallpaper groups clearly have their uses, they are not appropriate for characterizing 2D materials. While 2D materials have two dimensions of periodicity, they exist in a fully three-dimensional (3D) space. Space groups do take into

Table 5-1. Bravais lattices in two-dimensional space

Dimension \Periodicity	1D	2D	3D	Uses
1D	Line Groups	NULL	NULL	Intro to Symmetry
2D	Frieze Groups	Wallpaper Groups	NULL	Art
3D	Rod Groups	Layer Groups	Space Groups	Crystallography

account 3D space, the assumption of periodicity in three dimensions results in potentially misidentifying the primitive and Wigner-Seitz cell of a 2D crystal.

As monolayers exists in a 3D space, wallpaper groups fail to take into account the thickness of the monolayer, as they have periodicity in two dimensions yet exist in three dimensions. The reduction of space required to use wallpaper groups to classify symmetry has several problematic consequences. The first consequence is that mirror planes in the non-periodic direction aren't recognized. The importance of this distinction cannot be understated, given how critical it can be to reducing the form of property tensors. The second consequence is a simple inability to resolve atoms. By reducing the system to two dimensions, atoms can overlapping each other, either fully or partially eclipsing atoms. For $2H$ monolayers, which have formula units of AB_2, the B atoms have the same x and y coordinates, but distinct z coordinates. The reduction of space required by wallpaper groups makes it impossible to resolve the difference between these two atoms. The third consequence is the incorrect identification of symmetry operations. While the lack of mirror planes needs to be explicitly stated, other operations are also incorrectly identified. For example, using $2H$ monolayers again as an example, wallpaper groups identify a center of inversion in the material. This indicates that no piezoelectric tensor can exist in the monolayer. However, it has been seen to display such a response both computationally[467] and experimentally,[468] and can be clearly seen to lack such a center when viewed from the side.

Space groups being used to describe 2D materials initially seems sufficient. When considering higher symmetry monolayers, this can often hold true. However, for lower symmetry structures, there can be problems. Inherent to 2D material unit cells is an axis perpendicular to the in-plane lattice vectors. Lower symmetry space groups do not have this restriction, and as
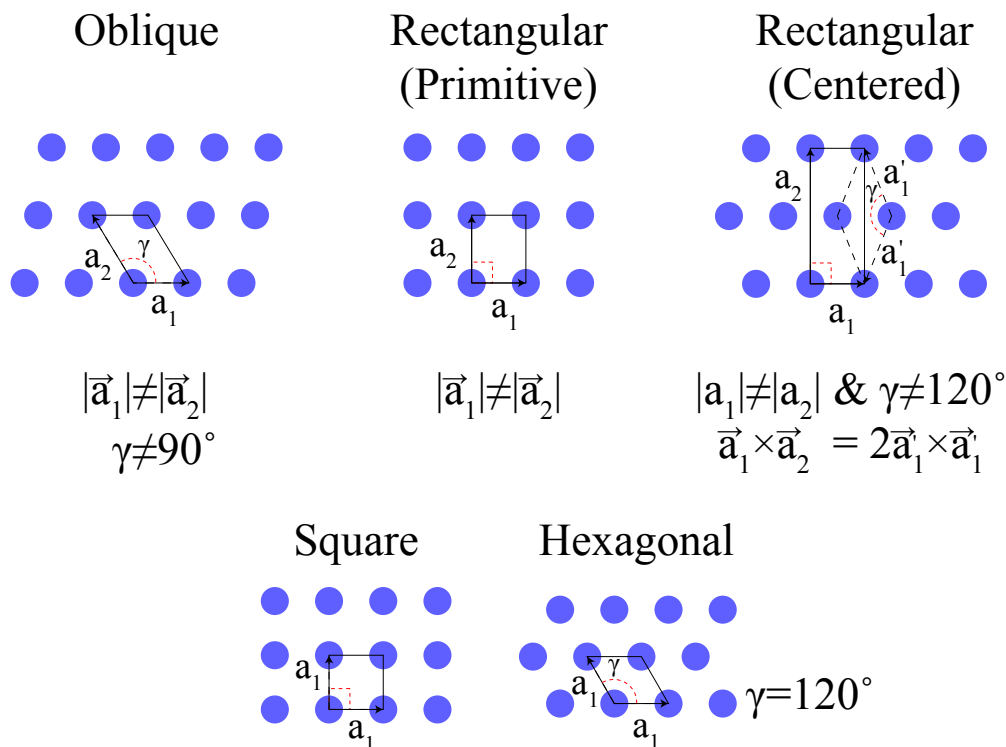
Figure 5-1. The 2D Bravais lattices, in order of increasing symmetry. When a third axis, perpendicular to the shown lattice vectors, is included the cells become monoclinic, orthorhombic, tetragonal, and hexagonal respectively.

a result using tools which assume 3D periodicity to treat 2D materials with low symmetry can result in drastically incorrect primitive cells. For example, tools for standardizing 3D crystals can result in monolayers with multi-atom thickness being collapsed such that all atoms lie in a single plane.

As neither wallpaper groups nor space groups can be used to properly describe and treat 2D material unit cells, there is a clear need to find an alternative approach. The solution is layer groups, which consider symmetry for systems which exist in three dimensions but are periodic in only two dimensions.[469,470] Though they have been known for decades, no tools currently exist for classifying monolayers using these groups.

In this work, we develop such a tool. This software properly treats and reduces 2D material unit cells and identifies their layer group symmetry as well as space group symmetry using the appropriate constraints. We begin by discussing the process of standardizing a 2D

material unit cell and the conventions we use. We follow by discussing the literature describing layer groups and how layer groups relate to space groups. From this we investigate the potential pitfalls of using fully periodic unit cells to identify layer groups to ensure the proper treatment. We then discuss how the layer group identification algorithm works and the results of applying it to 2D materials exfoliated from graphite-like crystals and cleaved from fully periodic crystals. Finally, we provide a convention for the high-symmetry electronic pathways for 2D materials.

5.2   Unit Cell Standardization

Before discussing how layer groups are determined, we will address the conventions we use to standardize 2D material unit cells. There exist five Bravais lattices for 2D systems, shown in Fig. 5-1.[471] These are strictly 2D space, whereas unit cells must be represented with three axiis. This makes the naming convention of the 2D material unit cells to, in order of symmetry: monoclinic, orthorhombic (primitive and centered), tetragonal, and hexagonal. The convention we use for representing 2D crystals depends on which of these five the 2D material falls into. $\overrightarrow{a_1}$ and $\overrightarrow{a_2}$ represent the in-plane vectors of the monolayer, with a_3 being perpendicular to it. For a given 2D material, the monolayer may not be parallel to a face of the unit cell. Thus, $\overrightarrow{a_1}$ and $\overrightarrow{a_2}$ must be identified as part of the preprocessing. We use the topological scaling algorithm (TSA)[22] to identify these vectors. This algorithm generates a supercell of the original crystal, then identifies the atomic network of the monolayer. This is done by starting at an atom in the unit cell, identifying nearby atoms with overlapping atomic radii, and adding these atoms to a list. When no new atoms can be added to the list, the list of all atoms in the monolayer has been created. Since this is a supercell of the original material, each site is seen four times in the network. By drawing vectors between identical sites, one can identify the in-plane vectors $\overrightarrow{a_1}$ and $\overrightarrow{a_2}$ needed to describe the 2D material. Though $\overrightarrow{a_3}$ is not a periodic dimension, it must be defined so that the heights of the atoms in the layers can be represented with fractional coordinates. All (primitive) orthorhombic and tetragonal cells are represented as

$$\begin{bmatrix} a_1 & 0 & 0 \\ 0 & a_2 & 0 \\ 0 & 0 & a_3 \end{bmatrix}$$

and all monoclinic and hexagonal systems are represented with

$$\begin{bmatrix} a_1 \times \cos(\theta/2) & a_1 \times \sin(\theta/2) & 0 \\ a_2 \times \cos(\theta/2) & -a_2 \times \sin(\theta/2) & 0 \\ 0 & 0 & a_3 \end{bmatrix}$$

where a_1, a_2, and a_3 are the magnitudes of the lattice vectors $\vec{a_1}$, $\vec{a_2}$, and $\vec{a_3}$ and θ is the in-plane angle between $\vec{a_1}$ and $\vec{a_2}$, chosen such that $\theta > \pi/2$. For these four Bravais lattices, the primitive and conventional cells are identical. For the centered orthorhombic, the former standard is used to represent the conventional cell and the latter is chosen to represent the primitive cell.

5.3   Mathematical Relation Between Layer Groups and Space Groups

With the unit cells standardized, layer group operations can be applied to identify symmetry. Layer groups can be derived from the reducible 3D space groups (1 to 194) for a total of 80 unique layer groups. However, the space and layer groups do not have a one-to-one relationship. For a given reducible space group, up to three layer groups can be derived. The following will be a summary of the work performed by Litvin and Kopský in 2000.[472] For a given reducible space group G, the translational operations associated with the group can be broken into two subgroups, written as

$$\mathrm{T} = \mathrm{T}_{G1} \oplus \mathrm{T}_{G2}, \tag{5-1}$$

where T is a translation subgroup of the reducible space group. T_{G1} and T_{G2} represent the set of all translations along one vector and within a plane perpendicular to said vector,

respectively. G can then be separated into factor groups based on the translational subgroups, such that G/T_{G1} is isomorphic to the symmetry operations of a single layer group. By choosing the translation vector in T_{G1} to be parallel to $\vec{a_1}$, $\vec{a_2}$, or $\vec{a_3}$ vector, a single space group can be used to derive more than one layer group. Thus, there is not a one-to-one relationship between layer groups and space groups. The highest layer group that can derived from monoclinic, orthorhombic, and tetragonal lattice systems is 18, 48, and 64 respectively.

The convention in the Bilbao Crystallographic Server defines the lattice vector perpendicular to the planes to be the $\vec{a_3}$ vector, which we follow in the previously discussed conventions for representing of the 2D crystals. A notable feature of layer groups is that no layer group operations has a translational component perpendicular to the layer.[472] This is sensible, as translational symmetry cannot exist along a dimension with no periodicity. This gives rise to the question of whether mirror planes perpendicular to the $\vec{a_3}$ axis can be misidentified. More specifically, whether the convention for defining the center of symmetry for a mirror plane need be layer-centered in middle the monolayer, or vacuum-centered in the middle of the vacuum of the non-periodic direction. Fig. 5-2 shows that either convention is appropriate, with all positions described using fractional coordinates. The distance d_{layer} represents the distance of an atom and it's image from a layer-centered mirror plane, with d_{vac} representing the same for the distance from a vacuum-centered mirror plane. If a mirror plane were to exist in the vacuum, it would be a distance of 0.5 from the center of the monolayer (Eq. 3). With this being the case, one can subtract Eq. 2 from Eq. 6 and identify that either the a layer-centered or vacuum-centered mirror plane can be used, as the resulting atoms are 1 lattice vector distance from each other. Since no glide operations can exist in the non-periodic direction due to the lack of translations, we have identified the potential pitfalls of using a periodic boundary to describe a non-periodic direction in these systems.

5.4 Layer Group Identification Tool

The flow of the algorithm is shown in Fig. 5-3. To begin, the structure of the monolayer is standardized as discussed previously. Next, each unique layer group operation is applied to

$$(1) \quad d_{layer} = z' - O_{I,layer}$$
$$= O_{I,layer} - z$$

$$(2) \quad z + z' = 2O_{I,layer}$$

$$(3) \quad O_{I,vac} = O_{I,layer} + .5$$
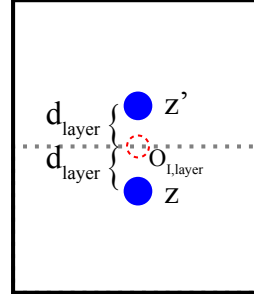
$$(4) \quad d_{vac} = z'' - O_{I,vac}$$
$$= O_{I,vac} - z$$

$$(5) \quad z + z'' = 2O_{I,vac}$$

$$(6) \quad z + z'' = 2O_{I,layer} + 1$$

$$(7) \quad (6) - (2) = z'' - z' = 1$$

$$(8) \quad z'' = z' + 1$$
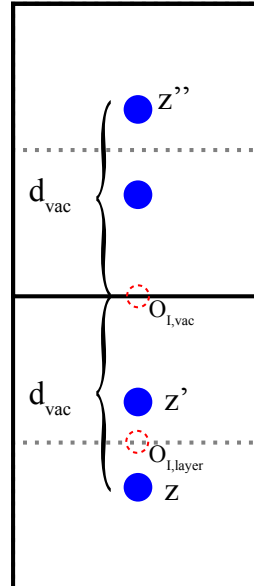
Figure 5-2. A demonstration of mirror planes existing in both the center of a monolayer and the center of the vacuum. If a mirror plane exists in the center of a monolayer, and exists in the center of the vacuum region, then they must be a fractional distance of 0.5 from each other. Using this, we can identify that the mirror image when using either a layer-centered mirror plane or a vacuum-centered mirror plane are 1 lattice vector apart, i.e. equivalent atoms. Thus, if a mirror plane exists in either the center of the vacuum or the center of the monolayer, then it must exist in both.
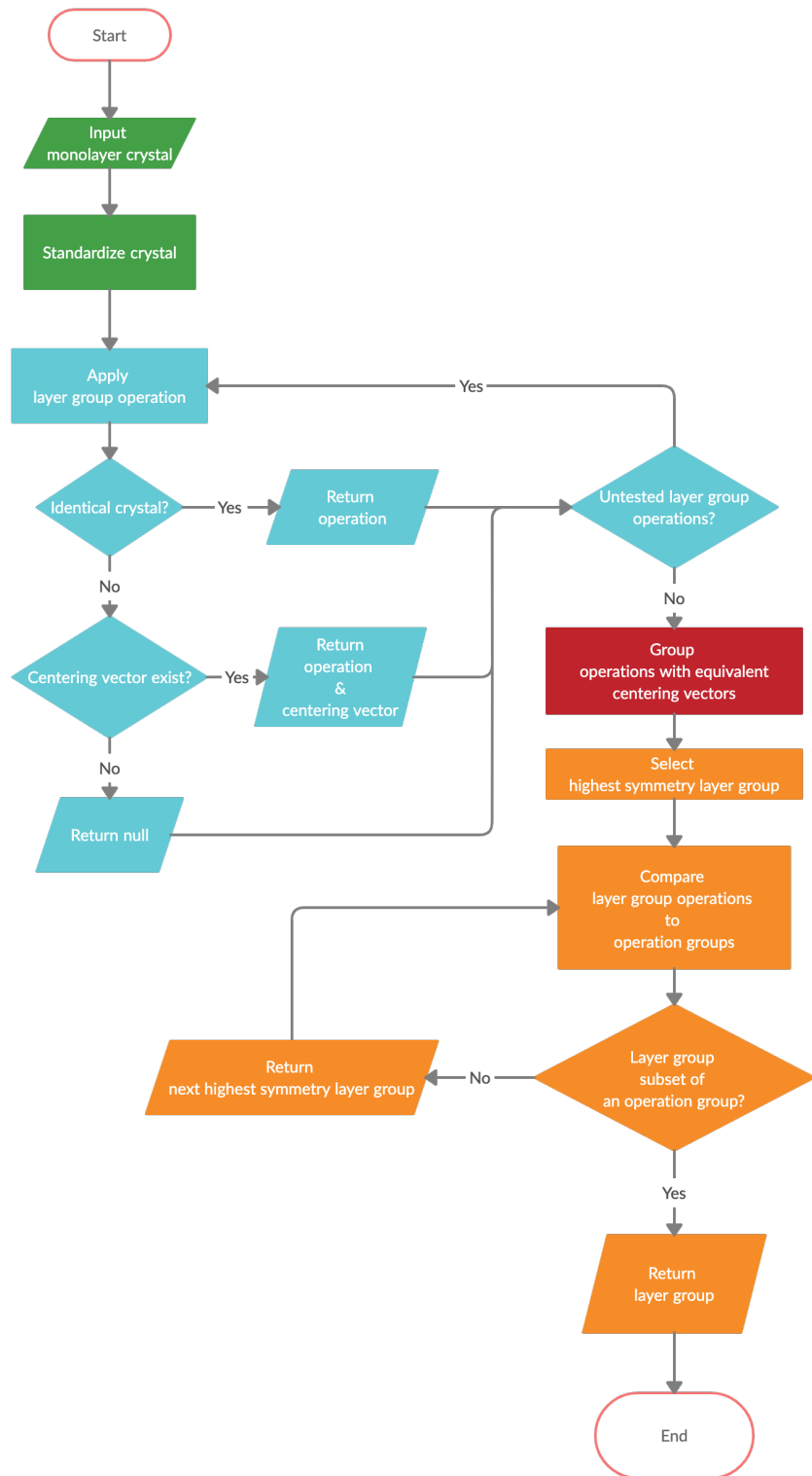
Figure 5-3. The flow of the algorithm to identify the layer group of a monolayer. The process can be broken into 4 components: preprocessing (green), layer group operation testing (blue), standardizing data (red), and identification of the layer group (orange).
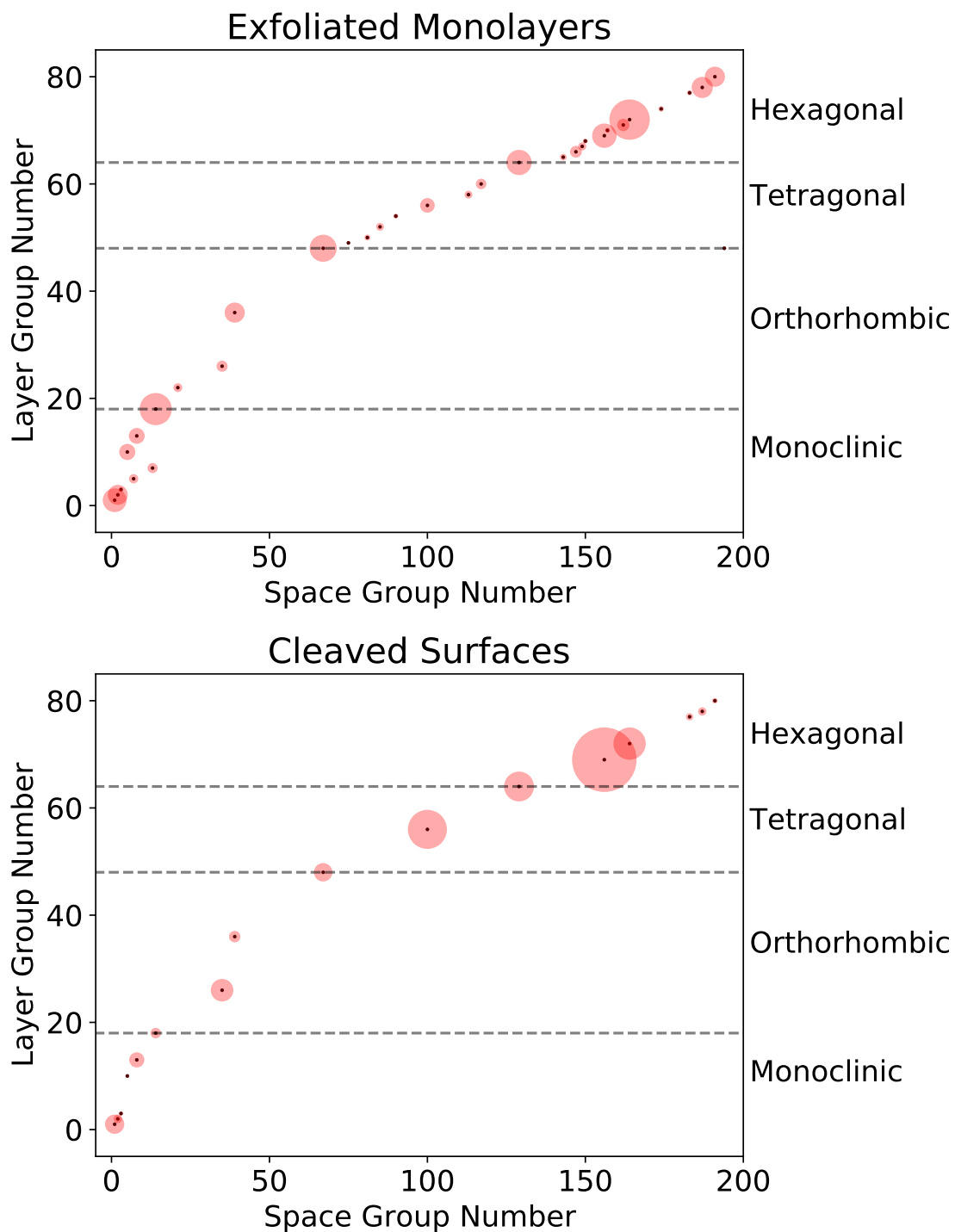
Figure 5-4. The relationship between space group and layer group for exfoliated monolayers and cleaved surfaces when accounting for reduced periodicity. This is shown in the top and bottom plots, respectively. Larger red circles represent the higher concentration of 2D materials with that space group-layer group relationship. The reducible space groups ends at space group 194, which is the maximum space group a 2D material can be.

the crystal. In order for a material to possess a specific symmetry operation, the coordinates of the material must be identical before and after the symmetry operation is applied to it. For each layer group operation, we apply the operation to the fractional coordinates of a material. Afterwards, we compare the positions of the atoms to each other in Cartesian space. This is done so that, if one generates a supercell of a crystal, the precision does not change due to the lattice vectors increasing in size.

If the atomic positions before and after the operation are indistinguishable, the operation is stored. If not, but a translation vector exists which can make the crystal identical to before the operation, the operation and the vector required to properly center the monolayer is stored. Once all operations are tested, the layer group operations are grouped based on which share equivalent centering vectors, where each operation can be in more than one group (e.g., the identity operation is present in all groups of operations, as any centering vector results in an identical match). Once these groups are defined, they are compared to the highest symmetry layer group. If the layer group is found to be a subset of one of the collected groups of operations, then the layer group is reported as the symmetry of the monolayer. If not, the process is repeated for the next highest symmetry layer group. A layer group will inevitably be identified, as layer group 1 consists of just the identity operation, and all groups of operations contain the identity operation.

The relationship between space groups and layer groups of various 2D materials are shown in Fig. 5-4. The left plot shows the relationship for 2,229 2D materials which are exfoliated from graphite-like crystals while the right plot is for 2,597 of the surfaces cleaved from bulk crystals in Chapter 4. The space group is identified using the same algorithm as for layer group, but comparing space group operations with at least one zero in the translational vector component of the operation. The same general trend between space group and layer group can be seen in both plots. In the case of cleaved surfaces, there is far less diversity in the number of layer groups. This is likely a consequence of the restrictions imposed on the cleaving algorithm. This indicates that certain layer groups are associated with low-energy

Table 5-2. High symmetry pathways for 2D Bravais lattices

Monoclinic			Orthorhombic (P)			Orthorhombic (C)			Tetragonal			Hexagonal		
$\times b_1$	$\times b_2$		$\times b_1$	$\times b_2$		$\times b_1$	$\times b_2$		$\times b_1$	$\times b_2$		$\times b_1$	$\times b_2$	
0	0	Γ	0	0	Γ	0	0	Γ	0	0	Γ	0	0	Γ
1/2	1/2	C	1/2	1/2	S	0	1/2	S	1/2	1/2	M	1/2	0	M
1/2	0	X	1/2	0	X	ζ	ζ	X	0	1/2	X	1/2	1/2	K
0	1/2	Y	0	1/2	Y	$-1/2$	1/2	Y						
η	$1-\nu$	H				$-\zeta$	$1-\zeta$	X_1						
$1-\eta$	ν	H_1												

$\eta = (1 - a\cos\alpha/b)/2\sin^2\alpha$ $\qquad\zeta = (1 + a^2/b^2)/4$
$\nu = 1/2 - \eta b\cos\alpha/a$

surfaces, with the most common being Layer Group 69 and 72. For the cleaved surfaces, a higher symmetry layer group always relates to a higher symmetry space group. While this holds generally true for exfoliated surfaces, outliers can be seen where a higher space group monolayer has a lower layer group. When using conventional space group analysis tools on 2D materials, we find near universal underestimation in the symmetry.

5.5 Electronic Structure

Setyawan and Curtarolo detailed a standardized approach to electronic band structure calculations of bulk materials in 2010.[473] 2D materials, due to their reduced periodicity, have Fermi surfaces which exist only in two dimensions. Thus, the electronic structure of 2D materials are described by a fully planar high symmetry pathway. For the five possible
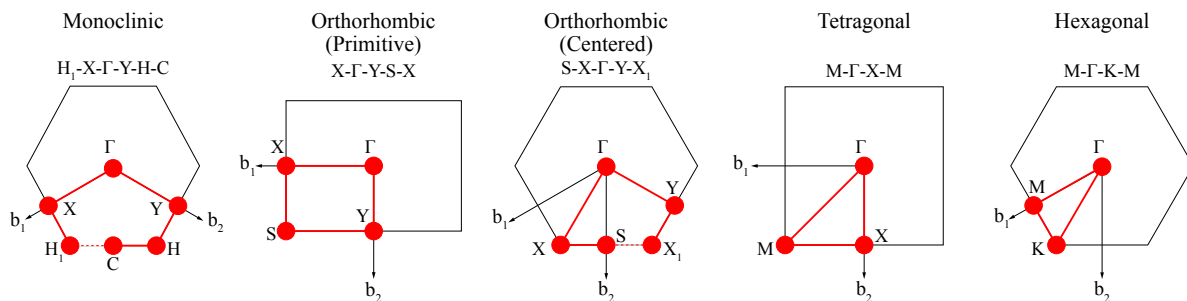
Figure 5-5. The high-symmetry pathways for electronic structure calculations of 2D material Bravais lattices. Since 2D materials are only periodic in two dimensions, 2D Bravais lattices can be used to determine the high-symmetry pathways for band structure identification.

Bravais lattices (monoclinic, primitive orthorhombic, centered orthorhombic, tetragonal, and hexagonal), a 2D material adopts one of five high-symmetry pathways, which are shown in Fig. 5-5. We select labels for the high-symmetry points to match the conventions set by Setyawan and Curtarolo.[473]

5.6   Summary

In summary, we developed a software tool to identify the layer group of 2D materials, as well the space group when the presence of a non-periodic boundary is enforced. We outline the known literature on how layer groups relate to space groups and consider the potential pitfalls associated with using a periodic boundary to describe a non-periodic dimension in a unit cell. We follow by discussing how the algorithm functions and apply it to 2D materials which are exfoliated form and cleaved from bulk crystals, identifying a difference in diversity of layer groups. We attribute this to the restrictions imposed by searching for planes of cleavage with low bond density. In future, expanding this software to classify 1D nanowires using rod groups is a clear path to building on this work, as well as returning reduced property tensors upon request based on the symmetry of the nanomaterial. There may be ways to use the layer groups of a thin film and a substrate to improve the best guess of how the interface will form, prior to performing any form of energy calculation.

CHAPTER 6
CONCLUSIONS

6.1   Summary

In this work, I investigated low-dimensional systems with datamining techniques as well as how to properly represent the symmetry of these systems. This dissertation begins with Ch. 2 providing a thorough review article authored in 2017, discussing the advancements in computational materials science research focused on 2D materials. I follow with Ch. 3, an application of the topological scaling algorithm (TSA) to search for van der Waals bonded nanowires in the MaterialsProject database. This chapter discusses the algorithm's sensitivity to bonding criteria and discusses unique crystals found, such as dimensional heterostructures and bipartite crystals. It then determines thermodynamic stability in exfoliated nanowires identified in the search and their diverse set of magnetic and electronic properties. Ch. 4 is an extended development of the TSA to cleave crystals and generate low-energy surfaces. This work has created a database of theoretical substrates with a wide range of lattice vectors, with demonstrated effectiveness on $BaSnO_3$. Ch. 5 investigates the failings associated with using fully periodic boundaries to treat symmetry in 2D materials. The software I developed for the work can properly treat the creation of primitive cells and conventional cells for 2D materials. It also uses layer groups to define the symmetry in 2D materials rather than space groups, as the former adequately addresses the reduced periodicity of monolayers. The chapter ends with applying the algorithm to two sets of 2D materials and defining conventions for the high-symmetry pathways used in electronic structure calculations of 2D materials.

6.2   Outlook

While Ch. 3 represents a significant step forward in understanding extereme nanowires, there are still several features that can be better understood. First, the magnetic ordering in these nanowires is of significant importance. A subset of nanowires were investigated for their magnetic behavior, but a broad study across many nanowires will be an important avenue of research. Further, identifying how these moments orient themselves, in the same

way, 2D materials are investigated and discussed in Ch. 2.8.3, will be relevant to any form of application of these materials in nanoelectronics. Along this same vein, how these properties change when transitioning from a single nanowire to a sheet of nanowires can significantly reduce the barrier to utilizing these materials in technological applications. How common and the impact of Peierls distortions is also relevant, as these periodic distortions may change the nanowire's properties.

Ch. 4 detailed an algorithm for cleaving periodic crystals to identify substrates. However, there are further applications of this algorithm. When growing a thin film, there can be competing facet orientations that the crystal can grow. Using the bond cleaving algorithm, one can search for low energy surfaces of the material of interest. The surface energy of these facets can then be calculated to identify how close in energy the desired orientation is to other facets of the crystal. Using this information, substrates can be explicitly chosen to promote the growth of the desired orientation based on the lattice strain imposed on the thin film. Further, the distribution of layer groups identified for low-energy facets in Ch. 5 can be used to inform the identification of future substrates without the need for explicitly cleaving bonds. With regard to datamining efforts, such approaches are inherently limited. An algorithm cannot be run again on the same dataset and obtain different results. Even in the case of the bond cleaving algorithm, although one could increase the scope of materials considered, there is still an inherent limit on its data mining potential. Future efforts to identify low-dimensional systems will require novel approaches which can be applied to the same datasets.

The importance of using layer groups to describe 2D materials is discussed in depth in Ch. 5, detailing the failings of wallpaper and space groups to describe 2D materials fully. This contribution will be significant in future discussions of 2D materials, with several impacts. First, using the symmetry operations identified by the algorithm to reduce the form of piezoelectric and elastic tensors will be able to guide the prediction of useful 2D materials. Second, the tool developed in this work will lower the barriers associated with 2D materials research through a uniform standard for unit cells and electronic structure. In addition, having tools to

properly handle 2D material unit cells can accelerate the research into these materials. Next steps in developing this software include expanding it to identify rod groups of 1D materials and applying it to the nanowires detailed in Ch. 3. Refining the crystal structure of 1D and 2D materials based on the applicable symmetry operations is an additional extension. This can accelerate the structural optimization of these systems by placing the atoms exactly at their high-symmetry positions, rather than performing a structural optimization calculation to reach those positions.

The impact of this research will be an important component of the foundation of future research into low-dimensional materials. As such, it is valuable to lower the barrier to access the tools and information of this work. The nanowires and substrates found in this work are being incorporated into the MaterialsWeb.org database to allow easy access to the crystal structures. The software developed is available or being integrated into the open-source software package MPInterfaces (https://github.com/henniggroup/MPInterfaces) so that other researchers can access, use, and develop the software themselves. Including interactive tools online at MaterialsWeb.org will lower the barrier to using and understanding the results discussed in this dissertation.

Low-dimensional materials have the potential to improve the performance of nanoelectronic devices significantly. However, they must be understood thoroughly to provide this improved performance. Thanks to the reduced cost of computational investigations, such efforts can accelerate the understanding of these systems. In this work, Ch. 3 provides a foundation to explore the applications of 1D materials further. Ch. 4 provides a novel way of searching for low-dimensional materials and substrates to grow them on. Ch. 5 provides a more accurate description of 2D material symmetry and presents conventions for describing 2D material unit cells and band structure diagrams. The results presented are progressions of work in the field thus far, and will be a valuable component of future research into low-dimensional materials.

REFERENCES

[1] Novoselov K S, Geim A K, Morozov S V, Jiang D, Zhang Y, Dubonos S V, Grigorieva I V and Firsov A A 2004 *Science* **306** 666–669

[2] Mak K F, Lee C, Hone J, Shan J and Heinz T F 2010 *Phys. Rev. Lett.* **105**(13) 136805 URL http://link.aps.org/doi/10.1103/PhysRevLett.105.136805

[3] Cassabois G, Valvin P and Gil B 2016 *Nat Photon* **10** 262–266 ISSN 1749-4885 URL http://dx.doi.org/10.1038/nphoton.2015.277http://10.0.4.14/nphoton.2015.277http://www.nature.com/nphoton/journal/v10/n4/abs/nphoton.2015.277.html{#}supplementary-information

[4] Singh A K, Mathew K, Zhuang H L and Hennig R G 2015 *The Journal of Physical Chemistry Letters* **6** 1087–1098 pMID: 26262874

[5] Liu H, Neal A T and Ye P D 2012 *ACS Nano* **6** 8563–8569 pMID: 22957650

[6] Roy T, Tosun M, Kang J S, Sachid A B, Desai S B, Hettick M, Hu C C and Javey A 2014 *ACS Nano* **8** 6259–6264 pMID: 24779528

[7] Mele E J and Král P 2002 *Phys. Rev. Lett.* **88**(5) 056803

[8] Blonsky M N, Zhuang H L, Singh A K and Hennig R G 2015 *ACS Nano* **9** 9885–9891

[9] Fei R, Faghaninia A, Soklaski R, Yan J A, Lo C and Yang L 2014 *Nano Letters* **14** 6393–6399

[10] Bourzac K 2013 *Nature* **493** 283

[11] Lan X, Voznyy O, García de Arquer F P, Liu M, Xu J, Proppe A H, Walters G, Fan F, Tan H, Liu M, Yang Z, Hoogland S and Sargent E H 2016 *Nano letters* **16** 4630–4634

[12] Bealing C R, Baumgardner W J, Choi J J, Hanrath T and Hennig R G 2012 *ACS Nano* **6** 2118–2127

[13] Medeiros P V C, Marks S, Wynn J M, Vasylenko A, Ramasse Q M, Quigley D, Sloan J and Morris A J 2017 *ACS Nano* **11** 6178–6185 pMID: 28467832

[14] Fujimori T, Morelos-Gómez A, Zhu Z, Muramatsu H, Futamura R, Urita K, Terrones M, Hayashi T, Endo M, Young Hong S, Chul Choi Y, Tománek D and Kaneko K 2013 *Nature Communications* **4** 2162 ISSN 2041-1723 URL https://doi.org/10.1038/ncomms3162

[15] Giusca C E, Stolojan V, Sloan J, Börrnert F, Shiozawa H, Sader K, Rümmeli M H, Büchner B and Silva S R P 2013 *Nano letters* **13** 4020—4027 ISSN 1530-6984

[16] Slade C A, Sanchez A M and Sloan J 2019 *Nano Letters* **19** 2979–2984 pMID: 30973739

[17] Vasylenko A, Marks S, Wynn J M, Medeiros P V C, Ramasse Q M, Morris A J, Sloan J and Quigley D 2018 *ACS Nano* **12** 6023–6031 pMID: 29782147

[18] The nobel prize in chemistry 1998 URL https://www.nobelprize.org/prizes/chemistry/1998/summary/

[19] The nobel prize in chemistry 1998 URL https://www.nobelprize.org/prizes/chemistry/1998/summary/

[20] Pollack L and Perdew J P 2000 *Journal of Physics: Condensed Matter* **12** 1239

[21] Zhuang H L and Hennig R G 2014 *JOM* **66** 366–374 ISSN 1543-1851

[22] Ashton M, Paul J, Sinnott S B and Hennig R G 2017 *Phys. Rev. Lett.* **118**(10) 106101 URL https://link.aps.org/doi/10.1103/PhysRevLett.118.106101

[23] Revard B C, Tipton W W, Yesypenko A and Hennig R G 2016 *Phys. Rev. B* **93**(5) 054117 URL http://link.aps.org/doi/10.1103/PhysRevB.93.054117

[24] Choudhary K, Kalish I, Beams R and Tavazza F 2017 *Sci. Rep.* **7** 5179 ISSN 2045-2322 URL https://doi.org/10.1038/s41598-017-05402-0

[25] Pouget J P 2016 *Comptes Rendus Physique* **17** 332 – 356 ISSN 1631-0705 physique de la matière condensée au XXIe siècle: l'héritage de Jacques Friedel URL http://www.sciencedirect.com/science/article/pii/S163107051500225X

[26] Toriyama T, Nakao A, Yamaki Y, Nakao H, Murakami Y, Hasegawa K, Isobe M, Ueda Y, Ushakov A V, Khomskii D I, Streltsov S V, Konishi T and Ohta Y 2011 *Phys. Rev. Lett.* **107**(26) 266402 URL https://link.aps.org/doi/10.1103/PhysRevLett.107.266402

[27] Eyert V 2002 *Europhysics Letters (EPL)* **58** 851–856 URL https://doi.org/10.1209%2Fepl%2Fi2002-00452-6

[28] Lebègue S, Björkman T, Klintenberg M, Nieminen R M and Eriksson O 2013 *Phys. Rev. X* **3**(3) 031002

[29] Cheon G, Duerloo K A N, Sendek A D, Porter C, Chen Y and Reed E J 2017 *Nano Lett.* **17** 1915–1923

[30] Mounet N, Gibertini M, Schwaller P, Campi D, Merkys A, Marrazzo A, Sohier T, Castelli I E, Cepellotti A, Pizzi G and Marzari N 2018 *Nature Nanotechnology* **13** 246–252 ISSN 1748-3395 URL https://doi.org/10.1038/s41565-017-0035-5

[31] Haastrup S, Strange M, Pandey M, Deilmann T, Schmidt P S, Hinsche N F, Gjerding M N, Torelli D, Larsen P M, Riis-Jensen A C, Gath J, Jacobsen K W, Mortensen J J, Olsen T and Thygesen K S 2018 *2D Materials* **5** 042002

[32] Şahin H, Cahangirov S, Topsakal M, Bekaroglu E, Akturk E, Senger R T and Ciraci S 2009 *Phys. Rev. B* **80**(15) 155453

[33] Şahin H, Cahangirov S, Topsakal M, Bekaroglu E, Akturk E, Senger R T and Ciraci S 2009 *Physical Review B* **80** 155453

[34] Zhuang H L, Singh A K and Hennig R G 2013 *Physical Review B* **87** 165415

[35] 2011 Materials genome initiative for global competitiveness Tech. rep. National Science and Technology Council

[36] Hellenbrandt M 2004 *Crystallography Reviews* **10** 17–22 URL http://dx.doi.org/10.1080/08893110410001664882

[37] Jain A, Ong S P, Hautier G, Chen W, Richards W D, Dacek S, Cholia S, Gunter D, Skinner D, Ceder G and Persson K a 2013 *APL Materials* **1** 011002 ISSN 2166532X URL http://link.aip.org/link/AMPADS/v1/i1/p011002/s1&Agg=doi

[38] Kirklin S, Saal J E, Meredig B, Thompson A, Doak J W, Aykol M, Rühl S and Wolverton C 2015 *NPJ Comput. Mater.* **1** 1–15

[39] Curtarolo S, Setyawan W, Wang S, Xue J, Yang K, Taylor R H, Nelson L J, Hart G L, Sanvito S, Buongiorno-Nardelli M, Mingo N and Levy O 2012 *Computational Materials Science* **58** 227 – 235 ISSN 0927-0256 URL http://www.sciencedirect.com/science/article/pii/S0927025612000687

[40] Bahn S R and Jacobsen K W 2002 *Computing in Science Engineering* **4** 56–66 ISSN 1521-9615

[41] Ong S P, Richards W D, Jain A, Hautier G, Kocher M, Cholia S, Gunter D, Chevrier V L, Persson K A and Ceder G 2013 *Computational Materials Science* **68** 314 – 319 ISSN 0927-0256

[42] Mathew K, Singh A K, Gabriel J J, Choudhary K, Sinnott S B, Davydov A V, Tavazza F and Hennig R G 2016 *Computational Materials Science* **122** 183 – 190 ISSN 0927-0256

[43] Novoselov K S, Geim A K, Morozov S V, Jiang D, Zhang Y, Dubonos S V, Grigorieva I V and Firsov A A 2004 *Science* **306** 666–669 ISSN 0036-8075

[44] Mermin N D and Wagner H 1966 *Phys. Rev. Lett.* **17**(22) 1133–1136

[45] Le Doussal P and Radzihovsky L 1992 *Phys. Rev. Lett.* **69**(8) 1209–1212

[46] Nelson D, Piran T and Weinberg S 2004 *Statistical mechanics of membranes and surfaces* (World Scientific)

[47] Pacilé D, Meyer J C, Ç Ö Girit and Zettl A 2008 *Applied Physics Letters* **92** 133107

[48] Splendiani A, Sun L, Zhang Y, Li T, Kim J, Chim C Y, Galli G and Wang F 2010 *Nano Letters* **10** 1271–1275 pMID: 20229981

[49] Wang Q H, Kalantar-Zadeh K, Kis A, Coleman J N and Strano M S 2012 *Nat Nano* **7** 699–712 ISSN 1748-3387

[50] Ma R and Sasaki T 2010 *Advanced Materials* **22** 5082–5104 ISSN 1521-4095

[51] Yin K, Zhang Y Y, Zhou Y, Sun L, Chisholm M F, Pantelides S T and Zhou W 2017 *2D Materials* **4** 011001

[52] Naguib M, Mashtalir O, Carle J, Presser V, Lu J, Hultman L, Gogotsi Y and Barsoum M W 2012 *ACS Nano* **6** 1322–1331 pMID: 22279971

[53] Ashton M, Mathew K, Hennig R G and Sinnott S B 2016 *The Journal of Physical Chemistry C* **120** 3550–3556

[54] Zhuang H L and Hennig R G 2013 *Applied Physics Letters* **103** 212102

[55] Zheng H, Li X B, Chen N K, Xie S Y, Tian W Q, Chen Y, Xia H, Zhang S B and Sun H B 2015 *Phys. Rev. B* **92**(11) 115307

[56] Lebègue S and Eriksson O 2009 *Phys. Rev. B* **79**(11) 115409

[57] Zhou L, Kou L, Sun Y, Felser C, Hu F, Shan G, Smith S C, Yan B and Frauenheim T 2015 *Nano Letters* **15** 7867–7872 pMID: 26524118

[58] Debbichi L, Kim H, Björkman T, Eriksson O and Lebègue S 2016 *Physical Review B* **93** 245307

[59] Liu H, Neal A T, Zhu Z, Luo Z, Xu X, Tománek D and Ye P D 2014 *ACS Nano* **8** 4033–4041 pMID: 24655084

[60] Revard B C, Tipton W W, Yesypenko A and Hennig R G 2016 *Physical Review B* **93** 054117

[61] Joensen P, Frindt R and Morrison S R 1986 *Mater. Res. Bull.* **21** 457–461

[62] Lin Y, Williams T V and Connell J W 2009 *J. Phys. Chem. Lett.* **1** 277–283

[63] Altuntasoglu O, Matsuda Y, Ida S and Matsumoto Y 2010 *Chem. Mater.* **22** 3158–3164

[64] Coleman J N, Lotya M, O'Neill A, Bergin S D, King P J, Khan U, Young K, Gaucher A, De S, Smith R J *et al.* 2011 *Science* **331** 568–571

[65] Naguib M, Kurtoglu M, Presser V, Lu J, Niu J, Heon M, Hultman L, Gogotsi Y and Barsoum M W 2011 *Advanced Materials* **23** 4248–4253 ISSN 1521-4095

[66] Lee Y H, Zhang X Q, Zhang W, Chang M T, Lin C T, Chang K D, Yu Y C, Wang J T W, Chang C S, Li L J *et al.* 2012 *Adv. Mater.* **24** 2320–2325

[67] Cong C, Shang J, Wu X, Cao B, Peimyoo N, Qiu C, Sun L and Yu T 2014 *Adv. Opt. Mater.* **2** 131–136

[68] Li X, Magnuson C W, Venugopal A, Tromp R M, Hannon J B, Vogel E M, Colombo L and Ruoff R S 2011 *J. Am. Chem. Soc.* **133** 2816–2819

[69] Hwang J, Kim M, Campbell D, Alsalman H A, Kwak J Y, Shivaraman S, Woll A R, Singh A K, Hennig R G, Gorantla S *et al.* 2012 *Acs Nano* **7** 385–395

[70] Singh A K, Zhuang H L and Hennig R G 2014 *Physical Review B* **89** 245431

[71] Al Balushi Z Y, Wang K, Ghosh R K, Vilá R A, Eichfeld S M, Caldwell J D, Qin X, Lin Y C, DeSario P A, Stone G *et al.* 2016 *Nature materials* **15** 1166–1171

[72] Zhuang H L, Johannes M D, Blonsky M N and Hennig R G 2014 *Appl. Phys. Lett.* **104** 022116

[73] Miro P, Audiffred M and Heine T 2014 *Chem. Soc. Rev.* **43**(18) 6537–6554

[74] Tang Q and Zhou Z 2013 *Progress in Materials Science* **58** 1244 – 1315 ISSN 0079-6425

[75] Gupta A, Sakthivel T and Seal S 2015 *Progress in Materials Science* **73** 44 – 126 ISSN 0079-6425

[76] Castro Neto A H, Guinea F, Peres N M R, Novoselov K S and Geim A K 2009 *Rev. Mod. Phys.* **81**(1) 109–162

[77] Shao Y, Wang J, Wu H, Liu J, Aksay I and Lin Y 2010 *Electroanalysis* **22** 1027–1036 ISSN 1521-4109

[78] Singh V, Joung D, Zhai L, Das S, Khondaker S I and Seal S 2011 *Progress in Materials Science* **56** 1178 – 1271 ISSN 0079-6425

[79] Abergel D, Apalkov V, Berashevich J, Ziegler K and Chakraborty T 2010 *Advances in Physics* **59** 261–482

[80] Lin Y and Connell J W 2012 *Nanoscale* **4**(22) 6908–6939

[81] Wang Q H, Kalantar-zadeh K, Kis A, Coleman J N and Strano M S 2012 *Nature Nanotechnology* **7** 699–712 copyright - Copyright Nature Publishing Group Nov 2012; Last updated - 2014-03-08

[82] Chhowalla M, Shin H S, Eda G, Li L J, Loh K P and Zhang H 2013 *Nat Chem* **5** 263–275 ISSN 1755-4330

[83] Naguib M, Mochalin V N, Barsoum M W and Gogotsi Y 2014 *Advanced Materials* **26** 992–1005 ISSN 1521-4095

[84] Osada M and Sasaki T 2009 *J. Mater. Chem.* **19**(17) 2503–2511

[85] Khandelwal A, Mani K, Karigerasi M H and Lahiri I 2017 *Materials Science and Engineering: B* **221** 17 – 34 ISSN 0921-5107

[86] Geim A K and Grigorieva I V 2013 *Nature* **499** 419–425 ISSN 0028-0836

[87] Niu T and Li A 2015 *Progress in Surface Science* **90** 21 – 45 ISSN 0079-6816 special Issue on Silicene

[88] Zhang T, Xue Q, Zhang S and Dong M 2012 *Nano Today* **7** 180 – 200 ISSN 1748-0132

[89] Cockayne E, Mihalkovič M and Henley C L 2016 *Phys. Rev. B* **93**(2) 020101

[90] Büchner C, Wang Z J, Burson K M, Willinger M G, Heyde M, Schlögl R and Freund H J 2016 *ACS Nano* **10** 7982–7989

[91] IUCr Commission 1992 *Acta Crystallographica Section A* **48** 922–946

[92] Mackay A L 1982 *Physica A: Statistical Mechanics and its Applications* **114** 609–613

[93] Förster S, Meinel K, Hammer R, Trautmann M and Widdra W 2013 *Nature* **502** 215

[94] Huang P Y, Kurasch S, Srivastava A, Skakalova V, Kotakoski J, Krasheninnikov A V, Hovden R, Mao Q, Meyer J C, Smet J, Muller D A and Kaiser U 2012 *Nano Letters* **12** 1081–1086

[95] Benedict L X, Chopra N G, Cohen M L, Zettl A, Louie S G and Crespi V H 1998 *Chemical Physics Letters* **286** 490–496

[96] Liu Z, Liu J Z, Cheng Y, Li Z, Wang L and Zheng Q 2012 *Physical Review B* **85** 205418

[97] Qian X, Liu J, Fu L and Li J 2014 *Science* **346** 1344–1347

[98] Zhuang H L, Johannes M D, Singh A K and Hennig R G 2017 *Phys. Rev. B* **96**(16) 165305 URL https://link.aps.org/doi/10.1103/PhysRevB.96.165305

[99] Liu H, Neal A T, Zhu Z, Luo Z, Xu X, Tománek D and Ye P D 2014 *ACS Nano* **8** 4033–4041

[100] Zhu Z and Tománek D 2014 *Phys. Rev. Lett.* **112**(17) 176802 URL https://link.aps.org/doi/10.1103/PhysRevLett.112.176802

[101] Guan J, Zhu Z and Tománek D 2014 *ACS Nano* **8** 12763–12768

[102] Wang G, Pandey R and Karna S P 2015 *ACS Applied Materials & Interfaces* **7** 11490–11496

[103] Sandoval E D, Hajinazar S and Kolmogorov A N 2016 *Phys. Rev. B* **94**(9) 094105

[104] Zhao Y, Zeng S and Ni J 2016 *Phys. Rev. B* **93**(1) 014502

[105] Li P and Luo W 2016 *Scientific Reports* **6** 25423

[106] Matusalem F, Marques M, Teles L K and Bechstedt F 2015 *Phys. Rev. B* **92**(4) 045436

[107] Singh A K, Revard B C, Ramanathan R, Ashton M, Tavazza F and Hennig R G 2017 *Phys. Rev. B* **95**(15) 155426

[108] Ding Y, Wang Y, Ni J, Shi L, Shi S and Tang W 2011 *Physica B: Condensed Matter* **406** 2254–2260

[109] Thomas L H 1927 *Mathematical Proceedings of the Cambridge Philosophical Society* **23** 542–548

[110] Fermi E 1927 *Rendiconti dell'Accademia dei Lincei*

[111] Weizsäcker C F v 1935 *Zeitschrift für Physik* **96** 431–458 ISSN 0044-3328

[112] Hohenberg P and Kohn W 1964 *Phys. Rev.* **136**(3B) B864–B871

[113] Kohn W and Sham L J 1965 *Phys. Rev.* **140**(4A) A1133–A1138

[114] Vosko S H, Wilk L and Nusair M 1980 *Canadian Journal of Physics* **58** 1200–1211

[115] Perdew J P and Zunger A 1981 *Phys. Rev. B* **23**(10) 5048–5079

[116] Perdew J P and Wang Y 1992 *Physical Review B* **45** 13244–13249 ISSN 0163-1829

[117] Ceperley D M and Alder B J 1980 *Phys. Rev. Lett.* **45**(7) 566–569

[118] Becke A D 2014 *The Journal of Chemical Physics* **140** 18A301 ISSN 0021-9606

[119] Perdew J P, Burke K and Ernzerhof M 1996 *Phys. Rev. Lett.* **77**(18) 3865–3868

[120] Becke A D 1988 *Physical Review A* **38** 3098–3100 ISSN 0556-2791

[121] Perdew J P, Yang W, Burke K, Yang Z, Gross E K U, Scheffler M, Scuseria G E, Henderson T M, Zhang I Y, Ruzsinszky A, Peng H, Sun J, Trushin E and Görling A 2017 *Proceedings of the National Academy of Sciences* **114** 2801–2806 ISSN 0027-8424

[122] Perdew J P, Ernzerhof M and Burke K 1996 *The Journal of Chemical Physics* **105** 9982–9985 ISSN 0021-9606

[123] Heyd J, Scuseria G E and Ernzerhof M 2003 *The Journal of Chemical Physics* **118** 8207–8215

[124] Batista E R, Heyd J, Hennig R G, Uberuaga B P, Martin R L, Scuseria G E, Umrigar C J and Wilkins J W 2006 *Phys. Rev. B* **74**(12) 121102

[125] Parker W D, Wilkins J W and Hennig R G 2011 *physica status solidi (b)* **248** 267–274

[126] Hennig R G, Wadehra A, Driver K P, Parker W D, Umrigar C J and Wilkins J W 2010 *Phys. Rev. B* **82**(1) 014101

[127] Anisimov V I, Zaanen J and Andersen O K 1991 *Physical Review B* **44** 943–954 ISSN 0163-1829

[128] Liechtenstein A I, Anisimov V I and Zaanen J 1995 *Phys. Rev. B* **52**(8) R5467–R5470

[129] Dudarev S L, Botton G A, Savrasov S Y, Humphreys C J and Sutton A P 1998 *Phys. Rev. B* **57**(3) 1505–1509

[130] Hedin L 1965 *Phys. Rev.* **139** A796—-A823

[131] Aryasetiawan F and Gunnarsson O 1998 *Reports on Progress in Physics* **61** 237

[132] Salpeter E E and Bethe H A 1951 *Phys. Rev.* **84**(6) 1232–1242

[133] Runge E and Gross E K U 1984 *Phys. Rev. Lett.* **52**(12) 997–1000

[134] Yang Z h and Ullrich C A 2013 *Phys. Rev. B* **87**(19) 195204

[135] Sharma S, Dewhurst J K, Sanna A and Gross E K U 2011 *Phys. Rev. Lett.* **107**(18) 186401

[136] Grimme S 2006 *Journal of Computational Chemistry* **27** 1787–1799 ISSN 0192-8651

[137] Grimme S, Ehrlich S and Goerigk L 2011 *Journal of Computational Chemistry* **32** 1456–1465 ISSN 01928651

[138] Dion M, Rydberg H, Schröder E, Langreth D C and Lundqvist B I 2004 *Phys. Rev. Lett.* **92**(24) 246401

[139] Klimeš J, Bowler D R and Michaelides A 2010 *Journal of Physics: Condensed Matter* **22** 022201

[140] Tkatchenko A and Scheffler M 2009 *Physical Review Letters* **102** 073005 ISSN 0031-9007

[141] Tkatchenko A, DiStasio R A, Car R and Scheffler M 2012 *Physical Review Letters* **108** 236402 ISSN 0031-9007

[142] Björkman T, Gulans A, Krasheninnikov A V and Nieminen R M 2012 *Phys. Rev. Lett.* **108**(23) 235502

[143] Zhou Y, Pellouchoud L A and Reed E J 2017 *2D Materials* **4** 025005

[144] Kresse G and Hafner J 1993 *Phys. Rev. B* **47**(1) 558–561

[145] Kresse G and Furthm uller J 1996 *Computational Materials Science* **6** 15 − 50 ISSN 0927-0256

[146] Kresse G and Furthmüller J 1996 *Phys. Rev. B* **54**(16) 11169–11186

[147] Giannozzi P, Baroni S, Bonini N, Calandra M, Car R, Cavazzoni C, Ceresoli D, Chiarotti G L, Cococcioni M, Dabo I, Dal Corso A, de Gironcoli S, Fabris S, Fratesi G, Gebauer R, Gerstmann U, Gougoussis C, Kokalj A, Lazzeri M, Martin-Samos L, Marzari N, Mauri F, Mazzarello R, Paolini S, Pasquarello A, Paulatto L, Sbraccia C, Scandolo S, Sclauzero G, Seitsonen A P, Smogunov A, Umari P and Wentzcovitch R M 2009 *Journal of Physics: Condensed Matter* **21** 395502 (19pp)

[148] Gonze X, Amadon B, Anglade P M, Beuken J M, Bottin F, Boulanger P, Bruneval F, Caliste D, Caracas R, Côté M, Deutsch T, Genovese L, Ghosez P, Giantomassi M, Goedecker S, Hamann D, Hermet P, Jollet F, Jomard G, Leroux S, Mancini M, Mazevet S, Oliveira M, Onida G, Pouillon Y, Rangel T, Rignanese G M, Sangalli D, Shaltaf R, Torrent M, Verstraete M, Zerah G and Zwanziger J 2009 *Computer Physics Communications* **180** 2582

– 2615 ISSN 0010-4655 40 {YEARS} {OF} CPC: A celebratory issue focused on quality software for high performance, grid and novel computing architectures

[149] Milman V, Winkler B, White J A, Pickard C J, Payne M C, Akhmatskaya E V and Nobes R H 2000 *International Journal of Quantum Chemistry* **77** 895–910 ISSN 1097-461X

[150] Rasmussen F A and Thygesen K S 2015 *J. Phys. Chem.* **119** 13169–13183

[151] Midwest nano infrastructure corridor 2d database http://apps.minic.umn.edu/2D/result.php accessed: 2017-05-24

[152] Parlinski K, Li Z Q and Kawazoe Y 1997 *Phys. Rev. Lett.* **78**(21) 4063–4066

[153] Baroni S, de Gironcoli S, Dal Corso A and Giannozzi P 2001 *Rev. Mod. Phys.* **73**(2) 515–562

[154] Togo A and Tanaka I 2015 *Scr. Mater.* **108** 1–5

[155] van de Walle A, Asta M D and Ceder G 2002 *Calphad* **26** 539–553

[156] van de Walle A 2009 *Calphad* **33** 266–278

[157] Lerch D, Wieckhorst O, Hart G L W, Forcade R W and Müller S 2009 *Modelling and Simulation in Materials Science and Engineering* **17** 055003

[158] Feng J, Hennig R G, Ashcroft N W and Hoffmann R 2008 *Nature* **451** 445–448 ISSN 0028-0836

[159] Rudin S P, Jones M D and Albers R C 2004 *Phys. Rev. B* **69**(9) 094117

[160] Ong S P, Wang L, Kang B and Ceder G 2008 *Chemistry of Materials* **20** 1798–1807 ISSN 0021-9606

[161] Jain A, Hautier G, Ong S, Moore C, Fischer C, Persson K and Ceder G 2011 *Physical Review B* **84** 045115 ISSN 1098-0121

[162] Shulenburger L, Baczewski A, Zhu Z, Guan J and Tománek D 2015 *Nano Letters* **15** 8170–8175

[163] Singh A K and Hennig R G 2014 *Applied Physics Letters* **105** 042103

[164] Ashton M, Gabriel J, Matthew K, Sinnott S B and Hennig R G 2017 Materialsweb https://materialsweb.org

[165] Zhang C, Yin H, Han M, Dai Z, Pang H, Zheng Y, Lan Y Q, Bao J and Zhu J 2014 *ACS Nano* **8** 3761–3770

[166] Singh A K and Hennig R G 2014 *Appl. Phys. Lett.* **105** 042103

[167] Persson K, Ekman M and Ozoliņš V 2000 *Phys. Rev. B* **61**(17) 11221–11224

[168] Hennig R G, Lenosky T J, Trinkle D R, Rudin S P and Wilkins J W 2008 *Phys. Rev. B* **78**(5) 054121

[169] Souvatzis P, Eriksson O, Katsnelson M I and Rudin S P 2008 *Phys. Rev. Lett.* **100**(9) 095901

[170] Kirkwood J G 1935 *The Journal of Chemical Physics* **3** 300–313

[171] Souvatzis P, Eriksson O, Katsnelson M and Rudin S 2009 *Computational Materials Science* **44** 888 – 894 ISSN 0927-0256

[172] Belsky A, Hellenbrandt M, Karen V L and Luksch P 2002 *Acta Crystallographica Section B: Structural Science* **58** 364–369

[173] Bahmann S and Kortus J 2013 *Computer Physics Communications* **184** 1618–1625

[174] Zhou X F, Dong X, Oganov A R, Zhu Q, Tian Y and Wang H T 2014 *Phys. Rev. Lett.* **112** 085502

[175] Zhou X F, Oganov A R, Wang Z, Popov I A, Boldyrev A I and Wang H T 2016 *Physical Review B* **93** 085406

[176] Zhao Y, Zeng S and Ni J 2016 *Physical Review B* **93** 014502

[177] Wang Z, Zhou X F, Zhang X, Zhu Q, Dong H, Zhao M and Oganov A R 2015 *Nano letters* **15** 6182–6186

[178] Xiang H, Huang B, Li Z, Wei S H, Yang J and Gong X 2012 *Physical Review X* **2** 011003

[179] Oganov A R and Glass C W 2006 *The Journal of chemical physics* **124** 244704

[180] Tipton W W and Hennig R G 2013 *Journal of Physics: Condensed Matter* **25** 495401

[181] Revard B C, Tipton W W and Hennig R G 2014 *Structure and Stability Prediction of Compounds with Evolutionary Algorithms* (Cham: Springer International Publishing) ISBN 978-3-319-05774-3

[182] Wang Y, Lv J, Zhu L and Ma Y 2010 *Phys. Rev. B* **82** 094116

[183] Luo X, Yang J, Liu H, Wu X, Wang Y, Ma Y, Wei S H, Gong X and Xiang H 2011 *Journal of the American Chemical Society* **133** 16285–16290

[184] Wang Y, Miao M, Lv J, Zhu L, Yin K, Liu H and Ma Y 2012 *The Journal of chemical physics* **137** 224108

[185] Luo W, Ma Y, Gong X and Xiang H 2014 *Journal of the American Chemical Society* **136** 15992–15997

[186] Wu X, Dai J, Zhao Y, Zhuo Z, Yang J and Zeng X C 2012 *ACS nano* **6** 7443–7453

[187] Lu H, Mu Y, Bai H, Chen Q and Li S D 2013 *The Journal of chemical physics* **138** 024701

[188] Dai J, Zhao Y, Wu X, Yang J and Zeng X C 2013 *The journal of physical chemistry letters* **4** 561–567

[189] Zhang M, Gao G, Kutana A, Wang Y, Zou X, John S T, Yakobson B I, Li H, Liu H and Ma Y 2015 *Nanoscale* **7** 12023–12029

[190] Ataca C, Sahin H and Ciraci S 2012 *The Journal of Physical Chemistry C* **116** 8983–8999

[191] Ashton M, Hennig R G, Broderick S R, Rajan K and Sinnott S B 2016 *Phys. Rev. B* **94**(5) 054116

[192] Naguib M, Kurtoglu M, Presser V, Lu J, Niu J, Heon M, Hultman L, Gogotsi Y and Barsoum M W 2011 *Advanced Materials* **23** 4248–4253

[193] Naguib M, Halim J, Lu J, Cook K M, Hultman L, Gogotsi Y and Barsoum M W 2013 *Journal of the American Chemical Society* **135** 15966–15969

[194] Mashtalir O, Naguib M, Mochalin V N, Dall'Agnese Y, Heon M, Barsoum M W and Gogotsi Y 2013 *Nature communications* **4** 1716

[195] Ghidiu M, Naguib M, Shi C, Mashtalir O, Pan L, Zhang B, Yang J, Gogotsi Y, Billinge S and Barsoum M 2014 *Chemical Communications* **50** 9517–9520

[196] Khazaei M, Arai M, Sasaki T, Chung C Y, Venkataramanan N S, Estili M, Sakka Y and Kawazoe Y 2013 *Advanced Functional Materials* **23** 2185–2192

[197] Urbankowski P, Anasori B, Makaryan T, Er D, Kota S, Walsh P L, Zhao M, Shenoy V B, Barsoum M W and Gogotsi Y 2016 *Nanoscale* **8** 11385–11391

[198] Persson K A, Waldwick B, Lazic P and Ceder G 2012 *Physical Review B* **85** 235438

[199] Mathew K, Sundararaman R, Letchworth-Weaver K, Arias T A and Hennig R G 2014 *The Journal of Chemical Physics* **140** 084106

[200] Leenaerts O, Partoens B and Peeters F M 2008 *Phys. Rev. B* **77**(12) 125416

[201] Schedin F, Geim A K, Morozov S V, Hill E W, Blake P, Katsnelson M I and Novoselov K S 2007 *Nature Materials* **6** 652–5

[202] Fowler J D, Allen M J, Tung V C, Yang Y, Kaner R B and Weiller B H 2009 *ACS Nano* **3** 301–306

[203] Dan Y, Lu Y, Kybert N J, Luo Z and Johnson A T C 2009 *Nano Letters* **9** 1472–1475

[204] González B S, Hernández-Rojas J, Bretón J and Gomez Llorente J M 2007 *The Journal of Physical Chemistry C* **111** 14862–14869

[205] Zhang Y H, Chen Y B, Zhou K G, Liu C H, Zeng J, Zhang H L and Peng Y 2009 *Nanotechnology* **20** 185504

[206] Liu H, Han N and Zhao J 2015 *RSC Adv.* **5**(23) 17572–17581

[207] Qiu H, Xu T, Wang Z, Ren W, Nan H, Ni Z, Chen Q, Yuan S, Miao F, Song F, Long G, Shi Y, Sun L, Wang J and Wang X 2013 *Nature Communications* **4** 2642

[208] Zhou W, Zou X, Najmaei S, Liu Z, Shi Y, Kong J, Lou J, Ajayan P M, Yakobson B I and Idrobo J C 2013 *Nano Letters* **13** 2615–2622

[209] Tongay S, Zhou J, Ataca C, Liu J, Kang J S, Matthews T S, You L, Li J, Grossman J C and Wu J 2013 *Nano Letters* **13** 2831–2836 pMID: 23627637

[210] Tongay S, Suh J, Ataca C, Fan W, Luce A, Kang J S, Liu J, Ko C, Raghunathanan R, Zhou J, Ogletree F, Li J, Grossman J C and Wu J 2013 *Scientific Reports* **3** 2657

[211] Perdew J P and Levy M 1983 *Phys. Rev. Lett.* **51**(20) 1884–1887

[212] Perdew J P 1985 *International Journal of Quantum Chemistry* **28** 497–523 ISSN 1097-461X

[213] Zhuang H L and Hennig R G 2013 *Phys. Rev. B* **88**(11) 115314

[214] Onida G, Reining L and Rubio A 2002 *Rev. Mod. Phys.* **74**(2) 601–659

[215] Frenkel J 1931 *Phys. Rev.* **37**(1) 17–44

[216] Wannier G H 1937 *Phys. Rev.* **52**(3) 191–197

[217] Ross J S, Wu S, Yu H, Ghimire N J, Jones A M, Aivazian G, Yan J, Mandrus D G, Xiao D, Yao W *et al.* 2013 *Nature Communications* **4** 1474

[218] Mak K F, He K, Lee C, Lee G H, Hone J, Heinz T F and Shan J 2013 *Nature materials* **12** 207–211

[219] Ziman J M 1979 *Principles of the Theory of Solids* (Cambridge University Press,Cambridge)

[220] Cheiwchanchamnangij T and Lambrecht W R L 2012 *Phys. Rev. B* **85**(20) 205302

[221] Chow P K, Jacobs-Gedrim R B, Gao J, Lu T M, Yu B, Terrones H and Koratkar N 2015 *ACS Nano* **9** 1520–1527 pMID: 25603228

[222] Nair R R, Blake P, Grigorenko A N, Novoselov K S, Booth T J, Stauber T, Peres N M R and Geim A K 2008 *Science* **320** 1308–1308 ISSN 0036-8075

[223] Bernardi M, Palummo M and Grossman J C 2013 *Nano Letters* **13** 3664–3670 pMID: 23750910

[224] Dumcenco D, Ovchinnikov D, Marinov K, Lazi? P, Gibertini M, Marzari N, Sanchez O L, Kung Y C, Krasnozhon D, Chen M W, Bertolazzi S, Gillet P, Fontcuberta i Morral A, Radenovic A and Kis A 2015 *ACS Nano* **9** 4611–4620 pMID: 25843548

[225] Tsai M L, Su S H, Chang J K, Tsai D S, Chen C H, Wu C I, Li L J, Chen L J and He J H 2014 *ACS Nano* **8** 8317–8322

226 Withers F, Del Pozo-Zamudio O, Mishchenko A, Rooney A P, Gholinia A, Watanabe K, Taniguchi T, Haigh S J, Geim A K, Tartakovskii A I and Novoselov K S 2015 *Nat Mater* **14** 301–306

227 Kittel C 2005 *Introduction to Solid State Physics* 8th ed (New York: John Wiley & Sons, Inc.)

228 Bak T, Nowotny J, Rekas M and Sorrell C 2002 *International journal of hydrogen energy* **27** 991–1022

229 Ni M, Leung M K, Leung D Y and Sumathy K 2007 *Renewable and Sustainable Energy Reviews* **11** 401–425

230 Sun Y, Cheng H, Gao S, Sun Z, Liu Q, Liu Q, Lei F, Yao T, He J, Wei S *et al.* 2012 *Angewandte Chemie International Edition* **51** 8727–8731

231 Sun Y, Sun Z, Gao S, Cheng H, Liu Q, Piao J, Yao T, Wu C, Hu S, Wei S *et al.* 2012 *Nature communications* **3** 1057

232 Voiry D, Yamaguchi H, Li J, Silva R, Alves D C, Fujita T, Chen M, Asefa T, Shenoy V B, Eda G *et al.* 2013 *Nature materials* **12** 850–855

233 Sun Y, Sun Z, Gao S, Cheng H, Liu Q, Lei F, Wei S and Xie Y 2014 *Advanced Energy Materials* **4**

234 Xu Y, Zhao W, Xu R, Shi Y and Zhang B 2013 *Chemical Communications* **49** 9803–9805

235 Liang L, Sun Y, Lei F, Gao S and Xie Y 2014 *Journal of Materials Chemistry A* **2** 10647–10653

236 Singh D, Gupta S K, Sonvane Y, Kumar A and Ahuja R 2016 *Catalysis Science & Technology* **6** 6605–6614

237 Gao J, Tay Q, Li P Z, Xiong W W, Zhao Y, Chen Z and Zhang Q 2014 *Chem.-Asian J.* **9** 131–134

238 Zhuang H L and Hennig R G 2013 *J. Phys. Chem. C* **117** 20440–20445

239 Zhuang H L and Hennig R G 2013 *Chem. Mater.* **25** 3232–3238

240 Chowdhury C, Karmakar S and Datta A 2017 *The Journal of Physical Chemistry C* **121** 7615–7624

241 Wang J, Meng J, Li Q and Yang J 2016 *Physical Chemistry Chemical Physics* **18** 17029–17036

242 Jiao Y, Zhou L, Ma F, Gao G, Kou L, Bell J, Sanvito S and Du A 2016 *ACS applied materials & interfaces* **8** 5385–5392

243 Liu J, Li X B, Wang D, Lau W M, Peng P and Liu L M 2014 *J. Chem. Phys.* **140** 054707

[244] Zhang X, Zhao X, Wu D, Jing Y and Zhou Z 2016 *Advanced Science* **3**

[245] Liu J, Li X B, Wang D, Liu H, Peng P and Liu L M 2014 *J. Mater. Chem. A* **2** 6755–6761

[246] Zhou L, Zhuo Z, Kou L, Du A and Tretiak S 2017 *Nano Letters*

[247] Zhang X, Li B, Wang J, Yuan Y, Zhang Q, Gao Z, Liu L M and Chen L 2014 *Phys. Chem. Chem. Phys.* **16**(47) 25854–25861

[248] Wang J, Zhang M, Meng J, Li Q and Yang J 2017 *RSC Advances* **7** 24446–24452

[249] Guo Z, Zhou J, Zhu L and Sun Z 2016 *Journal of Materials Chemistry A* **4** 11446–11452

[250] Ashton M, Sinnott S B and Hennig R G 2016 *Applied Physics Letters* **109** 192103

[251] Ashton M, Gluhovic D, Sinnott S B, Guo J, Stewart D A and Hennig R G 2017 *Nano Letters*

[252] Torun E, Sahin H, Singh S and Peeters F 2015 *Applied Physics Letters* **106** 192404

[253] Wilkinson M, Cable J, Wollan E and Koehler W 1959 *Phys. Rev.* **113** 497

[254] Sivadas N, Daniels M W, Swendsen R H, Okamoto S and Xiao D 2015 *Phys. Rev. B* **91**(23) 235425

[255] Kosterlitz J M and Thouless D J 1973 *Journal of Physics C: Solid State Physics* **6** 1181

[256] Šipr O, Bornemann S, Minár J, Polesya S, Popescu V, Šimnek A and Ebert H 2007 *Journal of Physics: Condensed Matter* **19** 096203 ISSN 0953-8984

[257] Kan M, Adhikari S and Sun Q 2014 *Phys. Chem. Chem. Phys.* **16**(10) 4990–4994

[258] Zhang H, Dai Y M and Liu L M 2015 *Computational Materials Science* **101** 255 – 259 ISSN 0927-0256

[259] Zhuang H L and Hennig R G 2016 *Phys. Rev. B* **93**(5) 054429

[260] Chittari B L, Park Y, Lee D, Han M, MacDonald A H, Hwang E and Jung J 2016 *Phys. Rev. B* **94**(18) 184428

[261] Sivadas N, Daniels M W, Swendsen R H, Okamoto S and Xiao D 2015 *Phys. Rev. B* **91**(23) 235425

[262] Zhuang H L, Xie Y, Kent P R C and Ganesh P 2015 *Phys. Rev. B* **92**(3) 035407

[263] Li X and Yang J 2014 *J. Mater. Chem. C* **2**(34) 7071–7076

[264] Zhang S, Li Y, Zhao T and Wang Q 2014 *Scientific Reports* **4** 5241

[265] Gong C, Li L, Li Z, Ji H, Stern A, Xia Y, Cao T, Bao W, Wang C, Wang Y, Qiu Z Q, Cava R J, Louie S G, Xia J and Zhang X 2017 *Nature* **advance online publication** –

[266] Huang B, Clark G, Navarro-Moratalla E, Klein D R, Cheng R, Seyler K L, Zhong D, Schmidgall E, McGuire M A, Cobden D H, Yao W, Xiao D, Jarillo-Herrero P and Xu X 2017 *Nature* **546** 270–273

[267] Zhuang H L, Kent P R C and Hennig R G 2016 *Phys. Rev. B* **93**(13) 134407

[268] Guo Y 2004 *Science* **306** 1915–1917 ISSN 0036-8075

[269] Sklyadneva I Y, Heid R, Bohnen K P, Echenique P M and Chulkov E V 2013 *Physical Review B* **87** 085440 ISSN 1098-0121

[270] Özer M M, Thompson J R and Weitering H H 2006 *Nature Physics* **2** 173–176 ISSN 1745-2473

[271] Noffsinger J and Cohen M L 2010 *Physical Review B* **81** 214519 ISSN 1098-0121

[272] Zhang T, Cheng P, Li W J, Sun Y J, Wang G, Zhu X G, He K, Wang L, Ma X, Chen X, Wang Y, Liu Y, Lin H Q, Jia J F and Xue Q K 2010 *Nat. Phys.* **6** 104–108 ISSN 1745-2473

[273] Noffsinger J and Cohen M L 2011 *Solid State Communications* **151** 421–424 ISSN 0038-1098

[274] Margine E R and Giustino F 2014 *Physical Review B* **90** 014518 ISSN 1098-0121

[275] Profeta G, Calandra M and Mauri F 2012 *Nature Physics* **8** 131–134 ISSN 1745-2473

[276] Zheng J J and Margine E R 2016 *Physical Review B* **94** 064509 ISSN 2469-9950

[277] Einenkel M and Efetov K B 2011 *Physical Review B* **84** 214508 ISSN 1098-0121

[278] Ludbrook B M, Levy G, Nigge P, Zonno M, Schneider M, Dvorak D J, Veenstra C N, Zhdanovich S, Wong D, Dosanjh P, Straßer C, Stöhr A, Forti S, Ast C R, Starke U and Damascelli A 2015 *Proceedings of the National Academy of Sciences* **112** 11795–11799 ISSN 0027-8424

[279] Hsu F C, Luo J Y, Yeh K W, Chen T K, Huang T W, Wu P M, Lee Y C, Huang Y L, Chu Y Y, Yan D C and Wu M K 2008 *Proceedings of the National Academy of Sciences* **105** 14262–14264 ISSN 0027-8424

[280] Wang Q Y, Li Z, Zhang W H, Zhang Z C, Zhang J S, Li W, Ding H, Ou Y B, Deng P, Chang K, Wen J, Song C L, He K, Jia J F, Ji S H, Wang Y Y, Wang L L, Chen X, Ma X C and Xue Q K 2012 *Chinese Physics Letters* **29** 037402 ISSN 0256-307X

[281] Lee J J, Schmitt F T, Moore R G, Johnston S, Cui Y T, Li W, Yi M, Liu Z K, Hashimoto M, Zhang Y, Lu D H, Devereaux T P, Lee D H and Shen Z X 2014 *Nature* **515** 245–248 ISSN 0028-0836

[282] Hirschfeld P J 2016 *Comptes Rendus Physique* **17** 197–231 ISSN 16310705

[283] Li B, Xing Z W, Huang G Q and Xing D Y 2014 *Journal of Applied Physics* **115** 193907 ISSN 0021-8979

[284] Wang Y, Linscheid A, Berlijn T and Johnston S 2016 *Physical Review B* **93** 134513 ISSN 2469-9950 (*Preprint* 1602.03288)

[285] Singh D J and Du M H 2008 *Physical Review Letters* **100** 237003 ISSN 0031-9007

[286] Zhou Y and Millis A J 2016 *Phys. Rev. B* **93**(22) 224506

[287] Linscheid A 2016 *Superconductor Science and Technology* **29** 104005 ISSN 0953-2048

[288] Maniadaki A E, Kopidakis G and Remediakis I N 2016 *Solid State Communications* **227** 33 − 39 ISSN 0038-1098

[289] Ni Z H, Yu T, Lu Y H, Wang Y Y, Feng Y P and Shen Z X 2008 *ACS Nano* **2** 2301–2305 pMID: 19206396

[290] Choi S M, Jhi S H and Son Y W 2010 *Phys. Rev. B* **81**(8) 081407

[291] Mohr M, Papagelis K, Maultzsch J and Thomsen C 2009 *Phys. Rev. B* **80**(20) 205410

[292] Wang J, Zhao R, Yang M, Liu Z and Liu Z 2013 *The Journal of Chemical Physics* **138** 084701

[293] Guzman D M and Strachan A 2014 *Journal of Applied Physics* **115** 243701

[294] Kou L, Frauenheim T and Chen C 2013 *The Journal of Physical Chemistry Letters* **4** 1730–1736 pMID: 26282986

[295] Guo H, Lu N, Wang L, Wu X and Zeng X C 2014 *The Journal of Physical Chemistry C* **118** 7242–7249

[296] Wang G, Pandey R and Karna S P 2015 *ACS Applied Materials & Interfaces* **7** 11490–11496

[297] Zhang J and Meguid S A 2017 *Semiconductor Science and Technology* **32** 043006

[298] Fei R, Li W, Li J and Yang L 2015 *Applied Physics Letters* **107** 173104

[299] Li W and Li J 2015 *Nano Research* **8** 3796–3802

[300] Zeng Z, Tan C, Huang X, Bao S and Zhang H 2014 *Energy Environ. Sci.* **7**(2) 797–803

[301] Lee C, Wei X, Kysar J W and Hone J 2008 *Science* **321** 385–388 ISSN 0036-8075

[302] Li W and Li J 2015 *Nano Research* **8** 3796–3802 ISSN 1998-0000

[303] Wang H and Qian X 2017 *2D Materials* **4** 015042

[304] Baroni S, Giannozzi P and Testa A 1987 *Phys. Rev. Lett.* **58**(18) 1861–1864

[305] Gonze X 1995 *Phys. Rev. A* **52**(2) 1086–1095

[306] Gonze X 1995 *Phys. Rev. A* **52**(2) 1096–1114

[307] Wu X, Vanderbilt D and Hamann D R 2005 *Phys. Rev. B* **72**(3) 035105

[308] Wang H, Zhang Y N, Wu R Q, Sun L Z, Xu D S and Zhang Z D 2013 *Scientific Reports* **3** 3521 EP –

[309] Cullen J R 1995 *Phys. Rev. B* **52**(1) 57–60

[310] Zhang G and Zhang Y W 2015 *Mechanics of Materials* **91** 382 – 398 ISSN 0167-6636 mechanics of energy conversion and storage

[311] Liu F, You L, Seyler K L, Li X, Yu P, Lin J, Wang X, Zhou J, Wang H, He H, Pantelides S T, Zhou W, Sharma P, Xu X, Ajayan P M, Wang J and Liu Z 2016 *Nature Communications* **7** 12357

[312] Wang H and Qian X 2017 *2D Materials* **4** 015042

[313] Lin Z, Carvalho B R, Kahn E, Lv R, Rao R, Terrones H, Pimenta M A and Terrones M 2016 *2D Materials* **3** 022002

[314] Terrones H, Lv R, Terrones M and Dresselhaus M S 2012 *Reports on Progress in Physics* **75** 062501

[315] Yazyev O V and Chen Y P 2014 *Nat. Nano.* **9** 755–767

[316] Liu L, Qing M, Wang Y and Chen S 2015 *Journal of Materials Science & Technology* **31** 599 – 606 ISSN 1005-0302 a Special Issue on 1D Nanomaterials

[317] Peng Q, Crean J, Dearden A K, Huang C, Wen X, Bordas S P and De S 2013 *Modern Physics Letters B* **27** 1330017

[318] Van de Walle C G and Neugebauer J 2004 *Journal of applied physics* **95** 3851–3879

[319] Zhang S and Northrup J E 1991 *Physical review letters* **67** 2339

[320] Cohen M L, Schlüter M, Chelikowsky J R and Louie S G 1975 *Physical Review B* **12** 5575

[321] Rurali R, Palummo M and Cartoixà X 2010 *Phys. Rev. B* **81**(23) 235304

[322] Komsa H P, Berseneva N, Krasheninnikov A V and Nieminen R M 2014 *Phys. Rev. X* **4**(3) 031044

[323] Dabo I, Kozinsky B, Singh-Miller N E and Marzari N 2008 *Phys. Rev. B* **77**(11) 115139

[324] Richter N A, Sicolo S, Levchenko S V, Sauer J and Scheffler M 2013 *Phys. Rev. Lett.* **111**(4) 045502

[325] Hockney R W 1970 Potential calculation and some applications. Tech. rep. Langley Research Center, Hampton, Va.

[326] Martyna G J and Tuckerman M E 1999 *The Journal of Chemical Physics* **110** 2810–2821

[327] Genovese L, Deutsch T, Neelov A, Goedecker S and Beylkin G 2006 *The Journal of Chemical Physics* **125** 074105

[328] Zou X, Liu Y and Yakobson B I 2013 *Nano Letters* **13** 253–258 pMID: 23227928

[329] Berger D and Ratsch C 2016 *Phys. Rev. B* **93**(23) 235441

[330] Banhart F, Kotakoski J and Krasheninnikov A V 2011 *ACS Nano* **5** 26–41 pMID: 21090760

[331] Camacho-Mojica D C and López-Urías F 2016 *Chemical Physics Letters* **652** 73 – 78 ISSN 0009-2614

[332] Huang P Y, Ruiz-Vargas C S, van der Zande A M, Whitney W S, Levendorf M P, Kevek J W, Garg S, Alden J S, Hustedt C J, Zhu Y, Park J, McEuen P L and Muller D A 2011 *Nature* **469** 389–392

[333] Enyashin A N, Bar-Sadan M, Houben L and Seifert G 2013 *The Journal of Physical Chemistry C* **117** 10842–10848

[334] van der Zande A M, Huang P Y, Chenet D A, Berkelbach T C, You Y, Lee G H, Heinz T F, Reichman D R, Muller D A and Hone J C 2013 *Nat. Mater.* **12** 554–561

[335] Zhang Z, Zou X, Crespi V H and Yakobson B I 2013 *ACS Nano* **7** 10475–10481

[336] Ren J C, Ding Z, Zhang R Q and Van Hove M A 2015 *Phys. Rev. B* **91**(4) 045425

[337] Kou L, Tang C, Guo W and Chen C 2011 *ACS Nano* **5** 1012–1017 pMID: 21229964

[338] Dutta S and Wakabayashi K 2015 *Scientific Reports* **5** 11744 EP –

[339] Son Y W, Cohen M L and Louie S G 2006 *Nature* **444** 347–349

[340] Okada S and Oshiyama A 2001 *Phys. Rev. Lett.* **87**(14) 146803

[341] Enoki T and Kobayashi Y 2005 *J. Mater. Chem.* **15**(37) 3999–4002

[342] Fujita M, Wakabayashi K, Nakada K and Kusakabe K 1996 *Journal of the Physical Society of Japan* **65** 1920–1923

[343] Nakada K, Fujita M, Dresselhaus G and Dresselhaus M S 1996 *Phys. Rev. B* **54**(24) 17954–17961

[344] Kobayashi Y, Fukui K i, Enoki T, Kusakabe K and Kaburagi Y 2005 *Phys. Rev. B* **71**(19) 193406

[345] Miyamoto Y, Nakada K and Fujita M 1999 *Phys. Rev. B* **59**(15) 9858–9861

[346] Cao D, Shen T, Liang P, Chen X and Shu H 2015 *The Journal of Physical Chemistry C* **119** 4294–4301

[347] Crespi V H, Benedict L X, Cohen M L and Louie S G 1996 *Phys. Rev. B* **53**(20) R13303–R13305

[348] Terrones H, Terrones M, Hernández E, Grobert N, Charlier J C and Ajayan P M 2000 *Phys. Rev. Lett.* **84**(8) 1716–1719

[349] Terrones H and Terrones M 2014 *2D Materials* **1** 011003

[350] Lee J, Huang J, Sumpter B G and Yoon M 2017 *2D Materials* **4** 021016

[351] Zhang X Q, Lin C H, Tseng Y W, Huang K H and Lee Y H 2015 *Nano Letters* **15** 410–415

[352] Son Y, Li M Y, Cheng C C, Wei K H, Liu P, Wang Q H, Li L J and Strano M S 2016 *Nano Letters* **16** 3571–3577 pMID: 27120519

[353] Wang H, Liu F, Fu W, Fang Z, Zhou W and Liu Z 2014 *Nanoscale* **6**(21) 12250–12272

[354] Fang H, Battaglia C, Carraro C, Nemsak S, Ozdol B, Kang J S, Bechtel H A, Desai S B, Kronast F, Unal A A, Conti G, Conlon C, Palsson G K, Martin M C, Minor A M, Fadley C S, Yablonovitch E, Maboudian R and Javey A 2014 *Proceedings of the National Academy of Sciences* **111** 6198–6202

[355] Novoselov K S, Mishchenko A, Carvalho A and Castro Neto A H 2016 *Science* **353** ISSN 0036-8075

[356] Fiori G, Bonaccorso F, Iannaccone G, Palacios T, Neumaier D, Seabaugh A, Banerjee S K and Colombo L 2014 *Nat Nano* **9** 768–779

[357] Akinwande D, Petrone N and Hone J 2014 *Nature Communications* **5** 5678 EP –

[358] Xia F, Wang H, Xiao D, Dubey M and Ramasubramaniam A 2014 *Nat Photon* **8** 899–907

[359] Yu W J, Li Z, Zhou H, Chen Y, Wang Y, Huang Y and Duan X 2013 *Nat Mater* **12** 246–252

[360] Lee C H, Lee G H, van der Zande A M, Chen W, Li Y, Han M, Cui X, Arefe G, Nuckolls C, Heinz T F, Guo J, Hone J and Kim P 2014 *Nat Nano* **9** 676–681

[361] Wang H, Yu L, Lee Y H, Fang W, Hsu A, Herring P, Chin M, Dubey M, Li L J, Kong J and Palacios T 2012 Large-scale 2d electronics based on single-layer mos2 grown by chemical vapor deposition *2012 International Electron Devices Meeting* pp 4.6.1–4.6.4 ISSN 0163-1918

[362] Wang H, Yu L, Lee Y H, Shi Y, Hsu A, Chin M L, Li L J, Dubey M, Kong J and Palacios T 2012 *Nano Letters* **12** 4674–4680 pMID: 22862813

[363] Keldysh L V 1965 *Sov. Phys. JETP* **20** 1018

[364] Datta S 1997 *Quantum Transport* (Cambridge University Press)

[365] Ferry D K; Goodnick S M 1997 *Transport in Nanostructures* (Cambridge University Press)

[366] Liu L, Lu Y and Guo J 2013 *IEEE Transactions on Electron Devices* **60** 4133–4139 ISSN 0018-9383

[367] Wang H, Hsu A, Kong J, Antoniadis D A and Palacios T 2011 *IEEE Transactions on Electron Devices* **58** 1523–1533 ISSN 0018-9383

[368] Jimenez D 2011 *IEEE Transactions on Electron Devices* **58** 4377–4383 ISSN 0018-9383

[369] Thiele S and Schwierz F 2011 *Journal of Applied Physics* **110** 034506

[370] Frégonése S, Magallo M, Maneux C, Happy H and Zimmer T 2013 *IEEE Transactions on Nanotechnology* **12** 539–546 ISSN 1536-125X

[371] Cheli M, Fiori G and Iannaccone G 2009 *IEEE Transactions on Electron Devices* **56** 2979–2986 ISSN 0018-9383

[372] Fahad M S, Srivastava A, Sharma A K and Mayberry C 2016 *IEEE Transactions on Nanotechnology* **15** 39–50 ISSN 1536-125X

[373] Liu L, Kumar S B, Ouyang Y and Guo J 2011 *IEEE Transactions on Electron Devices* **58** 3042–3047 ISSN 0018-9383

[374] Lam K T, Dong Z and Guo J 2014 *IEEE Electron Device Letters* **35** 963–965 ISSN 0741-3106

[375] Jiménez D 2012 *Applied Physics Letters* **101** 243501

[376] Kshirsagar C, Xu W, Kim C H and Koester S J 2014 Design and analysis of mos2-based mosfets for ultra-low-leakage dynamic memory applications *72nd Device Research Conference* pp 187–188 ISSN 1548-3770

[377] Cao W, Kang J, Liu W and Banerjee K 2014 *IEEE Transactions on Electron Devices* **61** 4282–4290 ISSN 0018-9383

[378] Suryavanshi S V and Pop E 2015 Physics-based compact model for circuit simulations of 2-dimensional semiconductor devices *2015 73rd Annual Device Research Conference (DRC)* pp 235–236 ISSN 1548-3770

[379] Yadav C, Agarwal A and Chauhan Y S 2017 *IEEE Transactions on Electron Devices* **64** 1261–1268 ISSN 0018-9383

[380] Jiang C, Liang R, Wang J and Xu J 2015 *AIP Advances* **5** 057122

[381] Chauhan J, Liu L, Lu Y and Guo J 2012 *Journal of Applied Physics* **111** 094313

[382] Ouyang Y, Campbell P and Guo J 2008 *Applied Physics Letters* **92** 063120

[383] Chauhan J and Guo J 2011 *Nano Research* **4** 571–579 ISSN 1998-0000

[384] Yoon Y and Guo J 2007 *Applied Physics Letters* **91** 073103

[385] Ouyang Y, Yoon Y and Guo J 2007 *IEEE Transactions on Electron Devices* **54** 2223–2231 ISSN 0018-9383

[386] Ouyang Y, Wang X, Dai H and Guo J 2008 *Applied Physics Letters* **92** 243124

[387] Yoon Y, Fiori G, Hong S, Iannaccone G and Guo J 2008 *IEEE Transactions on Electron Devices* **55** 2314–2323 ISSN 0018-9383

[388] Zhao P, Chauhan J and Guo J 2009 *Nano Letters* **9** 684–688 pMID: 19199761

[389] Ouyang Y, Dai H and Guo J 2010 *Nano Research* **3** 8–15 ISSN 1998-0000

[390] Yoon Y, Ganapathi K and Salahuddin S 2011 *Nano Letters* **11** 3768–3773 pMID: 21790188

[391] Alam K and Lake R K 2012 *IEEE Transactions on Electron Devices* **59** 3250–3254 ISSN 0018-9383

[392] Mishra V, Smith S, Ganapathi K and Salahuddin S 2013 Dependence of intrinsic performance of transition metal dichalcogenide transistors on materials and number of layers at the 5 nm channel-length limit *2013 IEEE International Electron Devices Meeting* pp 5.6.1–5.6.4 ISSN 0163-1918

[393] Liu F, Wang Y, Liu X, Wang J and Guo H 2014 *IEEE Transactions on Electron Devices* **61** 3871–3876 ISSN 0018-9383

[394] Wan R, Cao X and Guo J 2014 *Applied Physics Letters* **105** 163511

[395] Cao X and Guo J 2015 *IEEE Transactions on Electron Devices* **62** 659–665 ISSN 0018-9383

[396] Yin D, Han G and Yoon Y 2015 *IEEE Electron Device Letters* **36** 978–980 ISSN 0741-3106

[397] Yin D and Yoon Y 2016 *Journal of Applied Physics* **119** 214312

[398] Banerjee L, Mukhopadhyay A, Sengupta A and Rahaman H 2016 *Journal of Computational Electronics* **15** 919–930 ISSN 1572-8137

[399] Luo S, Lam K T, Wang B, Hsu C H, Huang W, Yao L Z, Bansil A, Lin H and Liang G 2017 *IEEE Transactions on Electron Devices* **64** 579–586 ISSN 0018-9383

[400] Han G and Yoon Y 2014 *Applied Physics Letters* **105** 213508

[401] Sengupta A, Chanana A and Mahapatra S 2015 *AIP Advances* **5** 027101

[402] Lam K T, Luo S, Wang B, Hsu C H, Bansil A, Lin H and Liang G 2015 Effects of interlayer interaction in van der waals layered black phosphorus for sub-10 nm fet *2015 IEEE International Electron Devices Meeting (IEDM)* pp 12.2.1–12.2.4

[403] Cao W, Kang J, Sarkar D, Liu W and Banerjee K 2015 *IEEE Transactions on Electron Devices* **62** 3459–3469 ISSN 0018-9383

[404] Nourbakhsh A, Zubair A, Sajjad R N, Tavakkoli K G A, Chen W, Fang S, Ling X, Kong J, Dresselhaus M S, Kaxiras E, Berggren K K, Antoniadis D and Palacios T 2016 *Nano Letters* **16** 7798–7806 pMID: 27960446

[405] Desai S B, Madhvapathy S R, Sachid A B, Llinas J P, Wang Q, Ahn G H, Pitner G, Kim M J, Bokor J, Hu C, Wong H S P and Javey A 2016 *Science* **354** 99–102 ISSN 0036-8075

[406] Dong Z and Guo J 2017 *IEEE Transactions on Electron Devices* **64** 622–628 ISSN 0018-9383

[407] Yin D, AlMutairi A and Yoon Y 2017 *IEEE Transactions on Electron Devices* **PP** 1–8 ISSN 0018-9383

[408] Lam K T, Cao X and Guo J 2013 *IEEE Electron Device Letters* **34** 1331–1333 ISSN 0741-3106

[409] Ghosh R K and Mahapatra S 2013 *IEEE Journal of the Electron Devices Society* **1** 175–180 ISSN 2168-6734

[410] Lam K T, Seol G and Guo J 2014 Performance evaluation of mos2-wte2 vertical tunneling transistor using real-space quantum simulator *2014 IEEE International Electron Devices Meeting* pp 30.3.1–30.3.4 ISSN 0163-1918

[411] Chang J and Hobbs C 2015 *Applied Physics Letters* **106** 083509

[412] Liu F, Shi Q, Wang J and Guo H 2015 *Applied Physics Letters* **107** 203501

[413] Agarwal T, Radu I, Raghavan P, Fiori G, Thean A, Heyns M and Dehaene W 2016 Effect of material parameters on two-dimensional materials based tfets: An energy-delay perspective *2016 46th European Solid-State Device Research Conference (ESSDERC)* pp 47–50

[414] Ilatikhameneh H, Tan Y, Novakovic B, Klimeck G, Rahman R and Appenzeller J 2015 *IEEE Journal on Exploratory Solid-State Computational Devices and Circuits* **1** 12–18 ISSN 2329-9231

[415] Chen F, Ilatikhameneh H, Tan Y, Valencia D, Klimeck G and Rahman R 2016 *arXiv preprint arXiv:1608.05057*

[416] Zur A and McGill T C 1984 *Journal of Applied Physics* **55** 378–386

[417] Alivisatos A P 1996 *Science* **271** 933–937 ISSN 0036-8075 (*Preprint* http://science.sciencemag.org/content/271/5251/933.full.pdf) URL http://science.sciencemag.org/content/271/5251/933

[418] Deng Y, Yu Y, Song Y, Zhang J, Wang N Z, Sun Z, Yi Y, Wu Y Z, Wu S, Zhu J and Wang J 2018 *Nature* **563** 94–99

[419] Han W 2016 *APL Materials* **4** 032401

[420] Pesin D and MacDonald A H 2012 *Nature Materials* **11** 409 URL https://doi.org/10.1038/nmat3305http://10.0.4.14/nmat3305

[421] Qian X, Liu J, Fu L and Li J 2014 *Science* **346** 1344–1347 ISSN 0036-8075 URL https://science.sciencemag.org/content/346/6215/1344

[422] Schaibley J R, Yu H, Clark G, Rivera P, Ross J S, Seyler K L, Yao W and Xu X 2016 *Nature Reviews Materials* **1** 16055 URL https://doi.org/10.1038/natrevmats.2016.55http://10.0.4.14/natrevmats.2016.55

[423] Hong W T, Risch M, Stoerzinger K A, Grimaud A, Suntivich J and Shao-Horn Y 2015 *Energy Environ. Sci.* **8**(5) 1404–1427

[424] Kodaimati M S, Lian S, Schatz G C and Weiss E A 2018 *Proc. Natl. Acad. Sci. U.S.A.* **115** 8290–8295

[425] Nelson A, Fritz K E, Honrao S, Hennig R G, Robinson R D and Suntivich J 2016 *J. Mater. Chem. A* **4**(8) 2842–2848

[426] Michalet X, Pinaud F F, Bentolila L A, Tsay J M, Doose S, Li J J, Sundaresan G, Wu A M, Gambhir S S and Weiss S 2005 *Science* **307** 538–544 ISSN 0036-8075 (*Preprint* http://science.sciencemag.org/content/307/5709/538.full.pdf) URL http://science.sciencemag.org/content/307/5709/538

[427] Chen F, Ma K, Benezra M, Zhang L, Cheal S M, Phillips E, Yoo B, Pauliah M, Overholtzer M, Zanzonico P, Sequeira S, Gonen M, Quinn T, Wiesner U and Bradbury M S 2017 *Chemistry of Materials* **29** 8766–8779

[428] Xia Y, Yang P, Sun Y, Wu Y, Mayers B, Gates B, Yin Y, Kim F and H H Y 2003 *Advanced Materials* **15** 353–389

[429] Thostenson E T, Ren Z and Chou T W 2001 *Composites Science and Technology* **61** 1899 – 1912 ISSN 0266-3538 URL http://www.sciencedirect.com/science/article/pii/S026635380100094X

[430] Dutta S and Pati S K 2010 *J. Mater. Chem.* **20**(38) 8207–8223

[431] Carter R, Sloan J, Kirkland A I, Meyer R R, Lindan P J D, Lin G, Green M L H, Vlandas A, Hutchison J L and Harding J 2006 *Phys. Rev. Lett.* **96**(21) 215501 URL https://link.aps.org/doi/10.1103/PhysRevLett.96.215501

[432] Mak K F, Lee C, Hone J, Shan J and Heinz T F 2010 *Phys. Rev. Lett.* **105**(13) 136805 URL https://link.aps.org/doi/10.1103/PhysRevLett.105.136805

[433] Halim J, Kota S, Lukatskaya M R, Naguib M, Zhao M Q, Moon E J, Pitock J, Nanda J, May S J, Gogotsi Y and Barsoum M W 2016 *Advanced Functional Materials* **26** 3118–3127 URL https://onlinelibrary.wiley.com/doi/abs/10.1002/adfm.201505328

[434] Yang X, Makita Y, Liu Z h, Sakane K and Ooi K 2004 *Chemistry of Materials* **16** 5581–5588

[435] Woomer A H, Farnsworth T W, Hu J, Wells R A, Donley C L and Warren S C 2015 *ACS Nano* **9** 8869–8884 pMID: 26256770

[436] Paul J T, Singh A K, Dong Z, Zhuang H, Revard B C, Rijal B, Ashton M, Linscheid A, Blonsky M, Gluhovic D, Guo J and Hennig R G 2017 *Journal of Physics: Condensed Matter* **29** 473001 URL http://stacks.iop.org/0953-8984/29/i=47/a=473001

[437] Zhuang H L and Hennig R G 2012 *Appl. Phys. Lett.* **101** 153109

[438] Singh A K and Hennig R G 2014 *Applied Physics Letters* **105** 051604 (*Preprint* http://dx.doi.org/10.1063/1.4892351) URL http://dx.doi.org/10.1063/1.4892351

[439] Balushi Z Y A, Wang K, Ghosh R K, Vilá R A, Eichfeld S M, Caldwell J D, Qin X, Lin Y C, DeSario P A, Stone G, Subramanian S, Paul D F, Wallace R M, Datta S, Redwing J M and Robinson J A 2016 *Nature Mater.* **15** 1166–1171

[440] Zhuang H L, Kent P R C and Hennig R G 2016 *Phys. Rev. B* **93**(13) 134407

[441] Fei Z, Huang B, Malinowski P, Wang W, Song T, Sanchez J, Yao W, Xiao D, Zhu X, May A F and Wu W 2018 *Nature Mater.* **17** 778–782

[442] Liu S, Yuan X, Zou Y, Sheng Y, Huang C, Zhang E, Ling J, Liu Y, Wang W, Zhang C and Zou J 2017 *NPJ 2D Mater. Appl.* **1** 1–7

[443] Zhou X, Brzostowski B, Durajski A, Liu M, Xiang J, Jiang T, Wang Z, Chen S, Li P, Zhong Z, Drzewiński A, Jarosik M, Szczesniak R, Lai T, Guo D and Zhong D 2020 *The Journal of Physical Chemistry C* **124** 9416–9423

[444] Larsen P M, Pandey M, Strange M and Jacobsen K W 2019 *Phys. Rev. Materials* **3**(3) 034003 URL https://link.aps.org/doi/10.1103/PhysRevMaterials.3.034003

[445] Du Y, Qiu G, Wang Y, Si M, Xu X, Wu W and Ye P D 2017 *Nano Letters* **17** 3965–3973 pMID: 28562056 (*Preprint* https://doi.org/10.1021/acs.nanolett.7b01717) URL https://doi.org/10.1021/acs.nanolett.7b01717

[446] Slater J C 1964 *J. Chem. Phys.* **41** 3199–3204

[447] Kresse G and Furthmüller J 1996 *Phys. Rev. B* **54**(16) 11169–11186 URL http://link.aps.org/doi/10.1103/PhysRevB.54.11169

[448] Blöchl P E 1994 *Phys. Rev. B* **50**(24) 17953–17979 URL http://link.aps.org/doi/10.1103/PhysRevB.50.17953

[449] Klimeš J, Bowler D and Michaelides A 2010 *J. Phys. Condens. Matter* **22** 022201 ISSN 1361-648X

[450] Misquitta A J, Spencer J, Stone A J and Alavi A 2010 *Phys. Rev. B* **82**(7) 075312 URL https://link.aps.org/doi/10.1103/PhysRevB.82.075312

[451] Bergerhoff G, Brown I, Allen F *et al.* 1987 *International Union of Crystallography, Chester* **360** 77–95

[452] Ashton M, Gluhovic D, Sinnott S B, Guo J, Stewart D A and Hennig R G 0 *Nano Letters* **0** null pMID: 28745061 URL http://dx.doi.org/10.1021/acs.nanolett.7b01367

[453] Paik H, Chen Z, Lochocki E, Seidner H A, Verma A, Tanen N, Park J, Uchida M, Shang S, Zhou B C, Brützam M, Uecker R, Liu Z K, Jena D, Shen K M, Muller D A and Schlom D G 2017 *APL Materials* **5** 116107

[454] Lee W J, Kim H J, Kang J, Jang D H, Kim T H, Lee J H and Kim K H 2017 *Annu. Rev. Mater. Res.* **47** 391–423

[455] Yoon D, Yu S and Son J 2018 *NPG Asia Materials* **10** 363–371 ISSN 1884-4057 URL https://doi.org/10.1038/s41427-018-0038-1

[456] Tipton W W and Hennig R G 2013 *J. Phys. Condens. Matter* **25** 495401 URL https://doi.org/10.1088%2F0953-8984%2F25%2F49%2F495401

[457] Hwang W S, Verma A, Peelaers H, Protasenko V, Rouvimov S, (Grace) Xing H, Seabaugh A, Haensch W, de Walle C V, Galazka Z, Albrecht M, Fornari R and Jena D 2014 *Appl. Phys. Lett.* **104** 203111

[458] Peelaers H and Van de Walle C G 2017 *Phys. Rev. B* **96**(8) 081409 URL https://link.aps.org/doi/10.1103/PhysRevB.96.081409

[459] Perdew J P, Burke K and Ernzerhof M 1996 *Phys. Rev. Lett.* **77**(18) 3865–3868 URL http://link.aps.org/doi/10.1103/PhysRevLett.77.3865

[460] Zhang C, Yin H, Han M, Dai Z, Pang H, Zheng Y, Lan Y Q, Bao J and Zhu J 2014 *ACS Nano* **8** 3761–3770

[461] de Jong M, Chen W, Angsten T, Jain A, Notestine R, Gamst A, Sluiter M, Krishna Ande C, van der Zwaag S, Plata J J, Toher C, Curtarolo S, Ceder G, Persson K A and Asta M 2015 *Scientific Data* **2** 150009 ISSN 2052-4463 URL https://doi.org/10.1038/sdata.2015.9

[462] Rieck H and Hoppe R 1973 *Z. Anorg. Allg. Chem.* **400** 311–320

[463] Rezende S M, Lucena M A, Azevedo A, Oliveira A B, de Aguiar F M and Egelhoff W F 2001 *J. Magn. Magn. Mater.* **226-230** 1683 – 1685 ISSN 0304-8853 URL http://www.sciencedirect.com/science/article/pii/S0304885300012002

[464] Kohle J and Petzel T 1977 *Zeitschrift fuer Anorganische und Allgemeine Chemie (1950) (DE)* **437** 193–196

[465] Mathew K, Gabriel J J, Ashton M, Singh A K, Paul J T, Monahan S G and Hennig R G 2018 MPInterfaces - Python package for high throughput analysis of materials interfaces

https://github.com/henniggroup/MPInterfaces URL https://github.com/henniggroup/MPInterfaces

[466] Clarke A D F, Green P R, Halley F and Chantler M J 2011 *Symmetry* **3**(2) 246–264

[467] Duerloo K A N, Ong M T and Reed E J 2012 *The Journal of Physical Chemistry Letters* **3** 2871–2876

[468] Wu W, Wang L, Li Y, Zhang F, Lin L, Niu S, Chenet D, Zhang X, Hao Y, Heinz T F, Hone J and Wang Z L 2014 *Nature* **514** 470–474

[469] Kopský V 1989 *Acta Crystallographica Section A* **45** 815–823

[470] Kopský V 1989 *Acta Crystallographica Section A* **45** 805–815

[471] Kittel C 2005 *Introduction to Solid State Physics* (John Wiley and Sons, Inc.)

[472] Litvin D and Kopsky V 2000 *Acta crystallographica. Section A, Foundations of crystallography* **56 (Pt 4)** 370–4

[473] Setyawan W and Curtarolo S 2010 *Comput. Mater. Sci.* **49** 299 – 312 ISSN 0927-0256 URL http://www.sciencedirect.com/science/article/pii/S0927025610002697

BIOGRAPHICAL SKETCH

Joshua Paul was born and raised in Glendale, Arizona, receiving a B.S. Materials science and engineering at the University of Arizona in 2015. After graduating, he was accepted into the Hennig Research Group at the University of Florida. During his tenure he performed an internship at the Army Research Lab in the summer of 2017 and was a participant of the Complex High-Dimensional Energy Landscape program in fall of 2017 at University of California Los Angeles. In his spare time, he enjoys playing Dungeons and Dragons and hiking.